DI Gernot Voitic, BSc

Pure compressed hydrogen production by chemical looping technology

DOCTORAL THESIS

to achieve the university degree of

Doktor der technischen Wissenschaften

submitted to

Graz University of Technology

Supervisor

Assoc.Prof. Dipl.-Ing. Dr.techn. Viktor Hacker

Institute of Chemical Engineering and Environmental Technology

Graz, October 2016

AFFIDAVIT

I declare that I have authored this thesis independently, that I have not used other than the declared sources/resources, and that I have explicitly indicated all material which has been quoted either literally or by content from the sources used. The text document uploaded to TUGRAZonline is identical to the present doctoral thesis.

Date

Signature

Preface

The work described in this thesis was commenced at the end of 2012 and was finished in December 2016. Most of the experimental investigations were executed as part of a small team of two or three researchers, which were embedded in the fuel cell work group at the Institute of Chemical Engineering and Environmental Technology at Graz University of Technology. The gross of the research was conducted within the project *Flex Fuel Reformer for Fuel-Cell Systems*, as part of the Research Studios Austria. Different research projects of the FFG (Austrian research promotion agency) and the NAWI Graz provided additional financial support.

I would like to thank Univ.-Prof Matthäus Siebenhofer and Assoc.Prof Viktor Hacker for the opportunity to conduct research in the scientific field of hydrogen generation and for the prospect to obtain the doctor of philosophy in chemical engineering. A special acknowledgment of my gratitude goes to Viktor Hacker for his support and counseling, which helped me to contribute to this scientific field and to finish this thesis. The sincere and amicable working environment that Viktor has created allowed for a fruitful and relaxing but nevertheless stimulating atmosphere.

I would also like to thank all my colleagues of the fuel cell group and of the Institute of Chemical Engineering for the cooperation.

Special thanks go to Stephan Nestl who worked very tightly with me on the field of hydrogen generation and on other projects. His ideas, opinions, suggestions and the intense discussions on controversial subjects were a huge contribution to my work.

“Thank you”, to the people who supported the completion of the thesis with their critical reviews: Eva, Karin, Stephan and Günther.

Finally, a big “Hvala!” to my family, parents, brother and sister, grandmother (and her card) and my wife Eva for their unconditional support to pursue my goals. Their encouraging words helped during harder times. To my son Aaron: “Thank you for your inspiration, may I be an inspiration to your future scientific achievements as well”.

Abstract

Hydrogen production by chemical looping is a promising technology to reduce harmful greenhouse gas emissions. Chemical Looping utilizes a solid oxygen carrier to transfer oxygen between a reducing and an oxidizing feed, which enables the separation of the carbon based feed stream from the product. The systems can be efficiently applied for decentralized small-scale hydrogen production. This enables the utilization of locally available renewable resources and produces hydrogen in the vicinity of the consumers to reduce transportation and storage demand.

A preparation method based on dry mixing of powder precursor was investigated for the manufacturing of iron based oxygen carriers with different additives for the chemical looping hydrogen process. Substantial stability improvements compared to untreated iron oxide were obtained by the addition of 10 – 15 wt% Al_2O_3 and CuO respectively. In addition the possibility of directly compressed hydrogen production was analyzed in a fixed bed reactor. An iron based oxygen carrier with 10 wt% Al_2O_3 was reduced at atmospheric pressure with pure hydrogen at 750 °C. In the subsequent oxidation liquid water was pumped into the reactor. The pressure build-up was realized by the water evaporation in the closed system. Steam reacted to hydrogen by oxidizing the reduced oxygen carrier to magnetite. The unreacted steam was condensed at the outlet, while compressed hydrogen remained in the system. A sequence of oxidations at different pressure levels was conducted. The experiments revealed no signs of repercussion on the hydrogen conversion efficiency and the oxygen carrier stability by the varying system pressure. The oxygen carrier maintained its porosity and structural integrity. A second set of pressure experiments was performed with an iron based oxygen carrier supported with 5 wt% Al_2O_3 and 5 wt% CeO_2. Reductions were executed with a synthesis gas mixture of H_2 54.5 vol%, CO 34.0 vol% and CO_2 11.5 vol% at 750 °C. Very pure hydrogen of 99.958% to 99.999% at a maximum pressure of 50 bar was obtained. Carbon monoxide and carbon dioxide were identified as the contaminations, which were formed by re-oxidizing of coke with steam. The coke formation occurred during the reduction and took place at the reactor inlet and outlet. On the oxygen carrier itself, no signs of solid carbon were found. The steam oxidations removed only small parts of the deposited carbon, which led to carbon-agglomeration and a steady decline of the hydrogen purity. Air oxidations were integrated in the cycle sequence to completely remove carbon residues and reverse the agglomeration effects. The experiments revealed that the hydrogen purity was not affected by the different pressure levels. The obtained results proved that the chemical looping process in a fixed bed reactor is suitable for the direct production of pure compressed hydrogen from carbon-based feedstocks.

Kurzfassung

Das Chemical Looping Verfahren zur Herstellung von Wasserstoff ist eine vielversprechende Technologie, um die Emissionen von schädlichen Treibhausgasen zu reduzieren. Beim Chemical Looping wird eine feste Kontaktmasse genutzt, um Sauerstoff zwischen einem oxidierenden und einem reduzierenden Gasstrom zu transferieren. Dies ermöglicht die effiziente Trennung des kohlenstoffhaltigen Rohstoffstroms vom Produktgas im kleinen Leistungsbereich und den Einsatz von lokal verfügbaren erneuerbaren Ressourcen. Hierbei wird der Wasserstoff in direkter Nähe am Verbraucher erzeugt, wodurch sich der Transport und Speicherbedarf reduziert.

Die Methode der Trockenmischung von pulverförmigen Ausgangsstoffen zur Herstellung von Eisenkontaktmassen mit unterschiedlichen Zusatzstoffen wurde erarbeitet. Dabei wurde eine deutliche Verbesserung der Zyklenstabilität durch den Zusatz von 10 – 15 Gew% Al_2O_3 oder CuO erzielt. Die Möglichkeit der direkten Erzeugung von komprimiertem Wasserstoff wurde im Festbettreaktor analysiert. Als Sauerstoffträger wurde Eisenoxid mit 10 Gew% Al_2O_3 eingesetzt. Dieser wurde unter atmosphärischen Bedingungen mit Wasserstoff bei 750 °C reduziert. In der darauffolgenden Oxidation wurde flüssiges Wasser in den Reaktor gepumpt. Durch die Verdampfung wurde ein Druckaufbau im geschlossenen System erzielt. Der Dampf oxidierte die reduzierte Reaktorfüllung zu Magnetit unter der Freisetzung von Wasserstoff. Der überschüssige Dampf wurde im Ausgangsbereich des Reaktors kondensiert und der komprimierte Wasserstoff verblieb im System. In dieser Serie von Oxidationen bei unterschiedlichem Systemdruck wurden keine Auswirkungen auf den Wasserstoffumsatz und die Kontaktmassenstabilität festgestellt, wobei die Porosität und Struktur des Sauerstoffträgers erhalten blieb. In einer zweiten Serie von Druckversuchen wurde die Reduktion mit einer Synthesegasmischung bestehend aus H_2 54.5 vol%, CO 34.0 vol% und CO_2 11.5 vol% bei 750 °C und einer Kontaktmasse aus Eisenoxid mit 5 Gew% Al_2O_3 und 5 Gew% CeO_2 durchgeführt. Hierbei wurde Wasserstoff mit einer Reinheit zwischen 99.958% – 99.999% und einem Maximaldruck von 50 bar erzeugt. Kohlenstoffmonoxid und Kohlenstoffdioxid wurden als Verunreinigungen identifiziert, die durch die Oxidation von abgeschiedenem Kohlenstoff gebildet wurden. Diese Verkokung wurde am Eingang und am Ausgang des Reaktors nachgewiesen. Auf der Kontaktmasse selbst wurde kein fester Kohlenstoff gefunden. Da durch die Dampfoxidation nur ein Bruchteil des Kohlenstoffs entfernt wurde, kam es zu einer fortschreitenden Verkokung und einer stetigen Verschlechterung der Wasserstoffreinheit. Zur vollständigen Entfernung des Kohlenstoffs wurden Luftoxidationen in die Zyklen integriert. Der erhöhte Systemdruck zeigte keinen Einfluss auf die Reinheit des erzeugten Wasserstoffs. Die Versuchsresultate belegten, dass das Chemical Looping Verfahren im Festbettreaktor zur Herstellung von reinem, komprimiertem Wasserstoff aus kohlenstoffhaltigen Rohstoffen geeignet ist.

Content

1 Introduction

In the following chapter, issues caused by anthropogenic CO_2 emissions and the correlation to climate change are discussed. Chemical looping hydrogen production is presented as a sustainable solution to reduce harmful carbon dioxide emissions.

Scientific and technological advancements are key components in the formation of the healthy and rich society we live in today. Since the industrial age, these technological expansions were paved with the increasing exploitation and consumption of newly discovered energy sources. Wood, the main energy carrier for centuries, was replaced by coal, oil and natural gas. Eventually, the enormous worldwide energy demand, displayed in figure 1, was satisfied by the utilization of a diversity of fossil fuels.

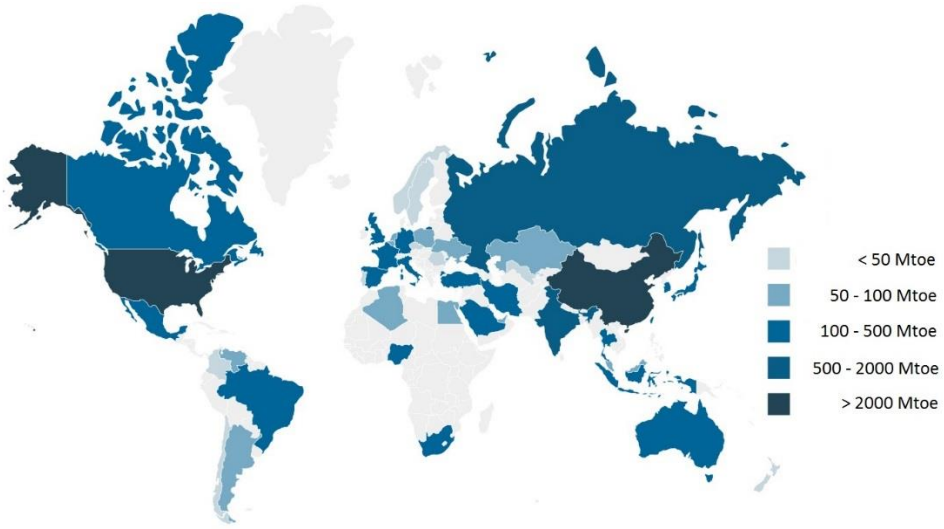

Figure 1: The main protagonists in the world's total energy consumption in 2015 (1 Mtoe = $41.868 \cdot 10^6$ GJ).[1] ¥

Since the 1950s a steep increase in energy and material consumption per capita occurred (figure 2). Until today this trend has continued. In combination with the development of non-OECD countries and the continuously growing world population, recent studies expect the growth in total energy and material demand to prolong for the next decades.[2]

Eventually two critical issues appeared and became urgent to a point where they can no longer be ignored or misinterpreted. Firstly, our exploitation rate of fossil energy carrier will lead to a scarcity of those resources. The retrograding yields of production from easily accessible and well-established deposits are currently compensated by tapping into new reserves. For instance in case of crude oil, deep-sea or arctic locations are made accessible by new drilling technology and unconventional precursor are exploited e.g. oil shale.[3–7] Both pathways have been successfully established, however at high risks of critical ecological impact and

significantly increased production costs.[6–8] An increase in the share of energy production from these sources may thrust the costs for energy to a point were repercussions on our global economic development lead to recession and poverty. Moreover, the scarceness of critical resources will provoke violent conflicts as it had already happened in the past. Hence, a transition to a society based on renewable energy and regenerative resources is crucial.[9,10]

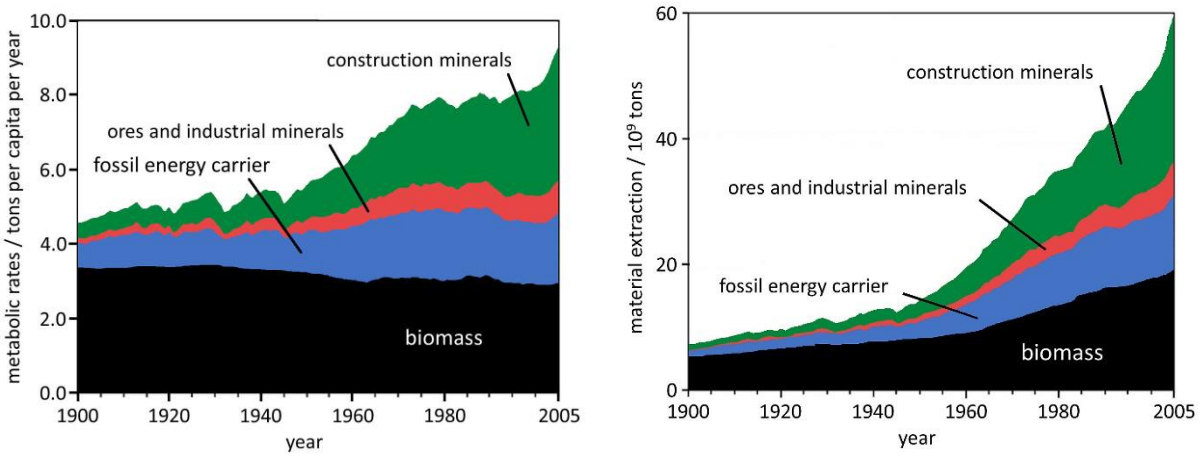

Figure 2: Left: the metabolic rates of material and energy carrier consumption per capita. Right: the total global material and energy carrier exploitation (left).[11] ¥¥

Secondly, the combustion of fossil fuels results in the release of huge amounts of anthropogenic CO_2 (figure 3, top). As a consequence a continuously rising CO_2 concentration in the atmosphere starting from the pre-industrial era to our present time is observed (figure 3, bottom).[12] Carbon dioxide is an active greenhouse gas and there is scientific consensus that anthropogenic CO_2 emissions significantly contribute to global warming and climate change.[13–16] Estimated consequences of global warming range from increasing sea levels, greater risks of weather extremes such as tornados or tsunamis, droughts, crop failure and dramatic changes of ecosystems.[12,17] The latter can be retraced by the recent outbreaks of diseases, for instance the Zika virus disease or the dengue fever. These infections are caused by mosquito bites of the two species, *Aedes aegypti* and *Aedes albopictus,* transferring the virus from the insectoid host to the human system in the process. These mosquitos usually inhabit hot and tropical climate zones. In recent years the infection carrying animals were able to duplicate their population by reducing the incubation time of each generation and by expanding to more temperate climate zones due to higher mean annual global temperature and shorter winters with less days of extreme cold. As a consequence disease outbreaks have been reported in several so far untouched regions (figure 4). Although climate change is not solely responsible for the spreading of these sicknesses but rather one of several factors, such as human population grow, urbanization and travel behavior, its impact nevertheless cannot be disregarded.[18–20]

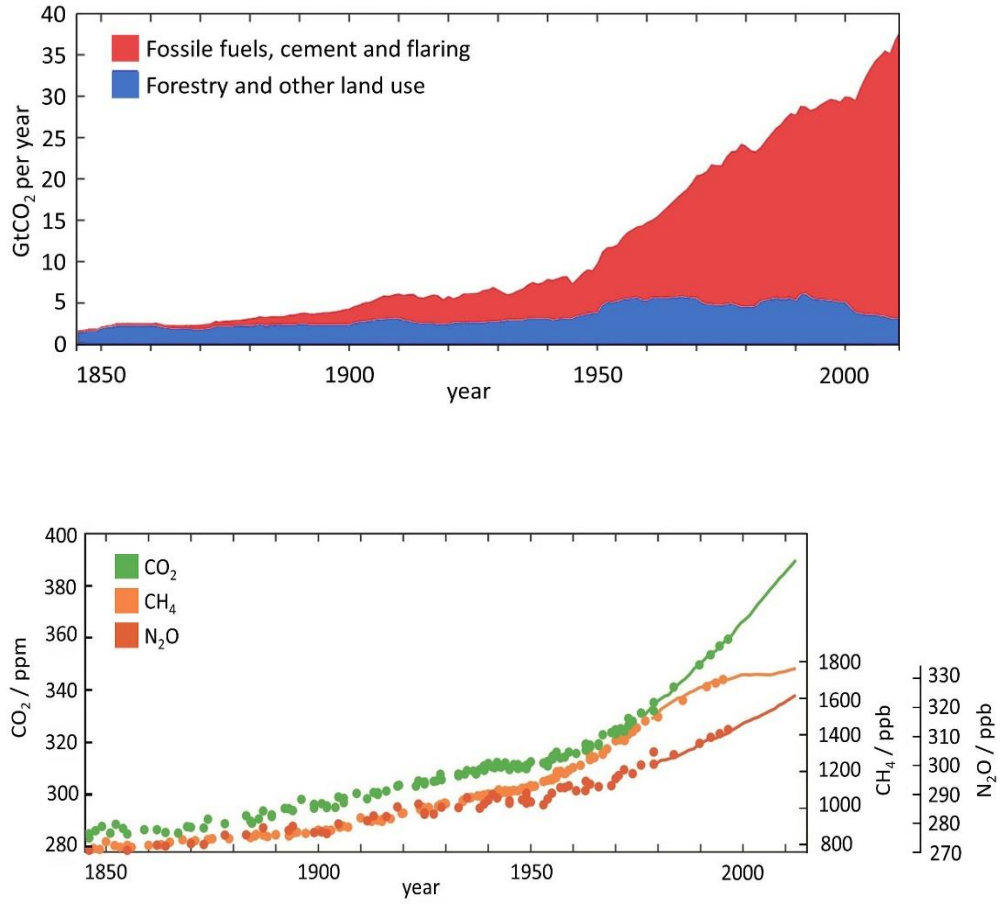

Figure 3: Top: global anthropogenic CO_2 emissions per year from forestry and other land use as well as from burning of fossil fuels, cement production and flaring. Bottom: historic development of the atmospheric concentrations of the greenhouse gases carbon dioxide, methane and nitrous oxide determined from ice core data (dots) and from direct atmospheric measurements (lines).[17]

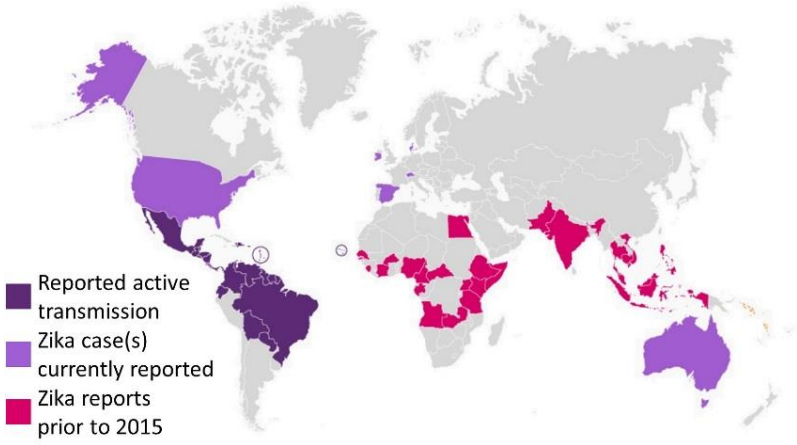

Figure 4: Countries with present and past Zika virus infections as of February 2016.[21] ¥¥¥

To mitigate the effects of global warming, clear tasks have been presented by the scientific community and its strongest committee, the intergovernmental panel on climate change IPCC. One major task is to limit the global warming to < 2 °C of the pre-industrial era by drastically reducing the greenhouse gas emissions (GHG).[12,17,22] Calculated trajectories, to estimate the mean global temperature development and to achieve the goal of limiting its increase, are conveyed in the representative concentration pathways (RCP), which embody the expected greenhouse gas concentration in the atmosphere (figure 5).

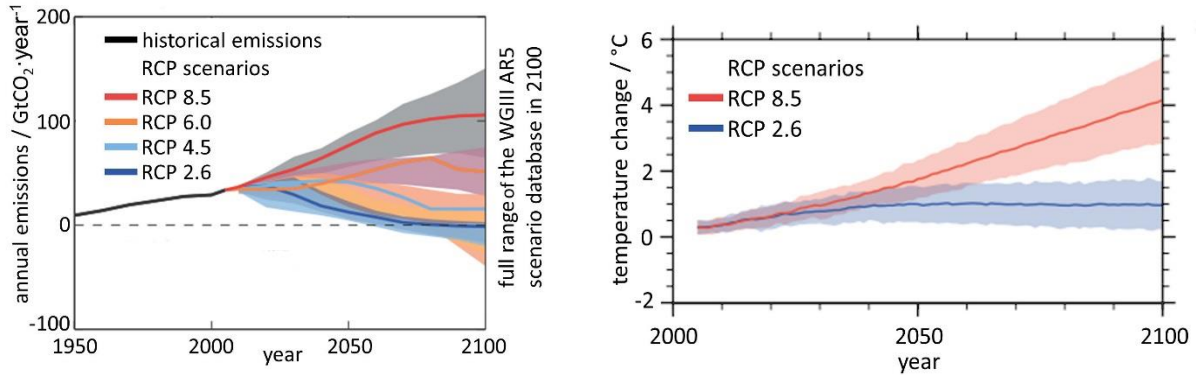

Figure 5: Left: annual anthropogenic CO_2 emissions in the different scenarios and its associated representative concentration pathways (RCPs). Right: global average surface temperature change, relative to 1986 – 2005, in two RCP scenarios including uncertainty bars.[17]

Two courses of action were proposed that can substantially contribute to the reduction of GHG emissions: the decarbonization of the energy sector and the replacement of fossil fuels with renewable sources.[12,17] A decarbonized energy sector requires the transition from most of our current energy conversion technologies and rely mostly on wind and solar power generation. According to the IEA energy statistics of 2015 (figure 6, left) only 8.4% (including 4.8% nuclear) of the total energy production currently does not rely on carbonaceous fuels. This current situation requires huge efforts to achieve a decarbonization and would require the increase from nuclear power. The replacement of fossil fuels with renewable carbonaceous feedstocks allows a faster transition based on well-established technologies while maintain a zero-net CO_2 emission balance. Both proposed pathways are not excluding each another but instead are intertwined and thus should be pursued jointly.

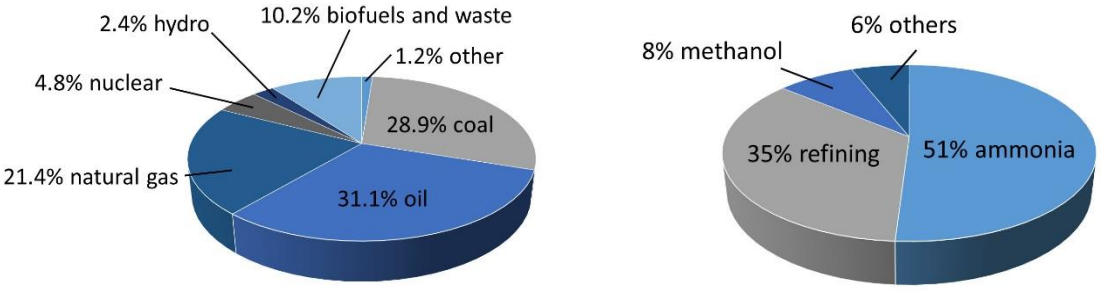

Figure 6: Left: total primary energy supply of 13541 Mtoe according to its resources (2013). Other includes geothermal, sun and wind. Coal includes peat and oil shale.[23] Right: the main hydrogen consuming sectors world-wide (2011).[24] ¥¥¥¥

In this context hydrogen is considered as a promising contribution to a future renewable energy mix. Currently hydrogen is primarily utilized in industrial processes as a bulk substance, while its share in the energy sector is marginal (< 2%) (figure 6, right). The increase of hydrogen for energy purposes offers the perspective of a clean fuel without any pollutant emissions, such as CO_2, CO, SO_2, NO_2 and particles. The implementation of hydrogen requires significant investments in the production-, distribution- and supply infrastructure to play a key role in fulfilling the global energy demand. However, hydrogen is a secondary energy source thus its environmental impact is defined by the resources and their production and purification processes. Potential sustainable production routes are electrolysis from wind or solar and the conversion of hydrocarbons from renewable feedstocks, such as ethanol and biogas, which enable substantial reduction of GHG emissions. These pathways are pursued by serval different technologies which are already under operation in prototype or industrial scales and available in commercial development status. However they usually suffer from higher hydrogen production costs compared to conventional large scale plants, which hinders their market penetration.[24–27]

Currently hydrogen is mainly produced in large scale reforming plants with fossil hydrocarbons or coal as feed. The steam reforming of hydrocarbons is currently the most common application with the highest hydrogen yield of the three possible reforming processes (eq. 1). The reforming process is usually followed by a 2-step water-gas-shift process (eq. 2) and final CO clean-up, e.g. pressure swing adsorption (PSA). The current hydrogen supply chain excels as reliable technology with a very high efficiency in large scale plants under stable operation conditions. The technology benefits from low production costs and the low cost resources.[24–26,28,29] Thus, hydrogen is nowadays produced in centralized plants transported over long distances by trucks and stored on-site in huge quantities. This distribution and storage logistic significantly contributes to the production costs of hydrogen.[30,31]

$$C_mH_n + mH_2O \rightarrow mCO + (m + 0.5n)H_2 \qquad \Delta H^0_{298K} = +205\ kJ{\cdot}mol^{-1} \qquad (1)$$

$$CO + H_2O \rightarrow CO_2 + H_2 \qquad \Delta H^0_{298K} = -41\ kJ{\cdot}mol^{-1} \qquad (2)$$

Currently the net production costs for hydrogen are primarily driven by the natural gas prize (figure 7, left), which results in significant deviations between global markets. Hydrogen production cost range from 0.8 €·kgH_2^{-1} to 2.0 €·kgH_2^{-1} with the USA at the lower end and the European Union at the upper boundary of the dispersion.[32–35]

For transportation purposes between the production plants and the filling or distribution stations, the hydrogen is usually compressed up to 500 bars or liquefied and transported by trucks or delivered via pipeline systems at 30 bar. For mobility applications hydrogen is filled into cars at a pressure of up to 900 bars. The hydrogen transportation, storage of large quantities and the gas compression are significant cost aspects in the hydrogen production chain and increase the hydrogen price at the filling stations considerably.[24,36–39] The cost contributions of transportation by trucks or via a pipeline system are depicted in figure 7, right. Truck transportation is favorable over short distances and in rural areas with a low hydrogen demand. A pipeline distribution system requires an initial high investment but excels in delivering high amounts of gas over long distances and in areas with a well-developed infrastructure.[36,39,40] The costs for gas compression to the final filling pressure of approximately 900 bar lies within the range of 0.5 €·kgH_2^{-1}. On-site storage costs are in the range of 0.09 – 0.29 €·kgH_2^{-1}, which incorporate a buffer to compensate for potential supply interruption. An Austrian case study assuming hydrogen production at the refinery in Schwechat and the utilization in Graz with a transportation distance of 200 km results in costs for the distribution of 1.45 – 1.65 €·kgH_2^{-1} and 1.71 – 1.91 €·kgH_2^{-1} for pipeline and trucks transportation respectively.[30,31] The calculated values are in good accordance with literature data and match the DOE targets for distribution costs in 2020.[39,41] Hence, in correlation to the net production costs (2.0 €·kgH_2^{-1}), the share of supply and distribution of the total costs (without taxes) in a centralized infrastructure is approximately 40% – 50%.

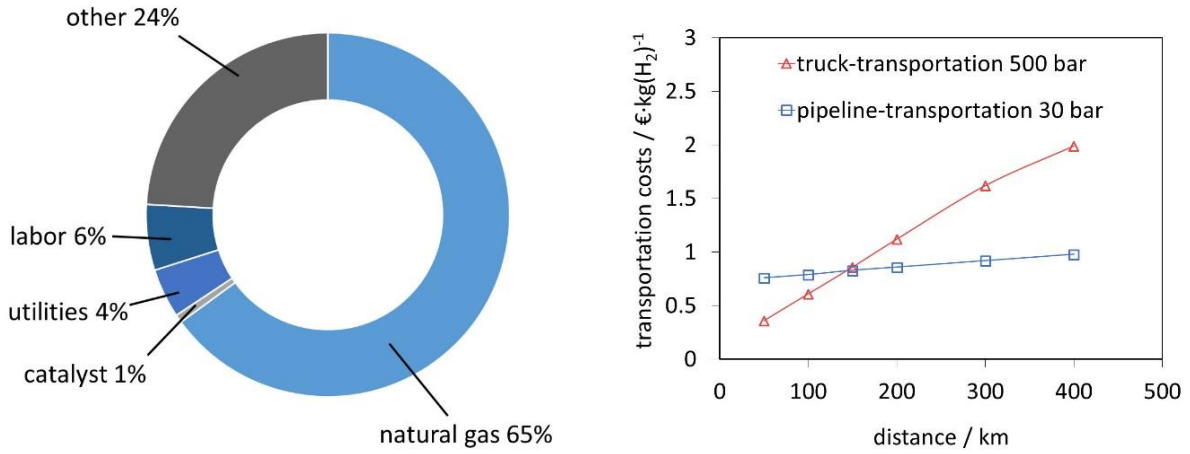

Figure 7: Left: hydrogen production cost distribution by steam methane reforming.[35] Right: hydrogen transportation costs with trucks or via pipelines.[31]

The hydrogen dispensing for mobile applications is dominated by two critical segments, the gas compression and the hydrogen storage systems. According to a study on hydrogen infrastructure for mobility these two segments contribute to more than 60% of the investment costs for hydrogen filling stations, and thus should be the main focus for technological improvements.[42,43] In conclusion, a restructuring of the energy production and distribution logistics can significantly accelerate the market penetration of hydrogen as an energy carrier. These technology vectors should be actively pursued and the research should happen parallel to the development of new technologies. This approach could enable fast transitions from the reliance on fossil fuel to a sustainable energy supply.

An auspicious approach to reshape the infrastructure for fuel distribution, while reducing the GHG emissions is the decentralized production of hydrogen based on renewable energy carriers. A decentralized, on-demand hydrogen production can greatly improve the cost efficiency of an area-wide hydrogen infrastructure by eliminating the transposition over long distances and the necessity to store large amounts of hydrogen on-site.[24,31,44] Decentralized hydrogen may still rely on conventional steam reforming of local available renewable resources to a hydrogen rich synthesis gas, followed by a two-step water gas shift reaction. However, in this process the produced hydrogen is diluted with CO_2. In the ideal case of pure methane as the hydrocarbon feedstock the produced gas consists of 80 vol% hydrogen (15 wt%) and 20 vol% carbon dioxide (85 wt%). Hence, for mobility applications an additional purification step has to be implemented in the process. These systems suffer from a substantial loss in efficiency declining from 70 – 85% to 51% when down-scaled for decentralized purposed and thus resulting in high production costs.[34]

As an alternative, decentralized small-scale chemical looping water splitting (CLWS), a modification of chemical looping combustion (CLC), is a very promising technology to produce pure hydrogen by cyclic operation. At Graz University of Technology the reformer sponge iron cycle (RESC), a chemical looping hydrogen system was introduced.[45,46] In contrast to other published systems, which currently focus on the utilization of two- or three-interconnected fluidized beds for large-scale applications,[47–49] the RESC is operated with fixed bed reactors. The absence of moving parts in the reactor and the equal temperature distribution in the system are expected to show advantages for the small scale decentralized hydrogen production. The process was subjected to an extensive evaluation of the thermodynamic potential and experimental studies for component development.[50,51] Finally, this led to the development of the reformer steam-iron process, which offers the perspective of a decentralized, on-demand, emission-free hydrogen production out of renewable hydrocarbon feedstocks (e.g. biogas). This technology enables:

- The production of environment-friendly hydrogen utilizing renewable hydrocarbons to reduce the global CO_2 emissions
- Decentralized production logistics to reduce hydrogen transport and storage demand and lower total production costs.

The reformer steam-iron process, depicted in figure 8, combines the conventional steam reforming with the chemical looping water splitting process. Both processes are executed in fixed beds, which are mutually placed inside one tubular reactor. A hydrocarbon feedstock is converted with steam by heterogeneous catalysis in the reforming bed to a hydrogen-rich synthesis gas (eq. 1). The syngas is directly used to reduce the iron-based oxygen carrier from hematite Fe_2O_3 or magnetite Fe_3O_4 to a more reduced state (wustite FeO or iron Fe) (eq. 3-5). In the subsequent process step steam re-oxidizes the oxygen carrier by releasing hydrogen (eq. 6). The oxidation with steam can only oxidize iron to magnetite due to thermodynamic limitations. The oxidation with air or oxygen leads to the formation of the initial state of the oxygen carrier (hematite) (eq. 7). The new reactor design and advancements in the process were filled for patent: WO 2016011473 A1, “Verfahren zum Herstellen von Wasserstoff”, by S. Nestl, V. Hacker and G. Voitic, issued 2016.[52] A detailed description and experimental results of the reformer steam-iron process are presented in the doctoral thesis by Nestl S..[53]

$$Fe_2O_3 + 3(H_2/CO) \rightarrow 2Fe + 3(H_2O/CO_2) \quad (3)$$

$$Fe_3O_4 + H_2/CO \rightarrow 3FeO + H_2O/CO_2 \quad (4)$$

$$FeO + H_2/CO \rightarrow Fe + H_2O/CO_2 \quad (5)$$

$$3Fe + 4H_2O \rightarrow Fe_3O_4 + 4H_2 \quad (6)$$

$$2Fe_3O_4 + 1/2O_2 \rightarrow 3Fe_2O_3 \quad (7)$$

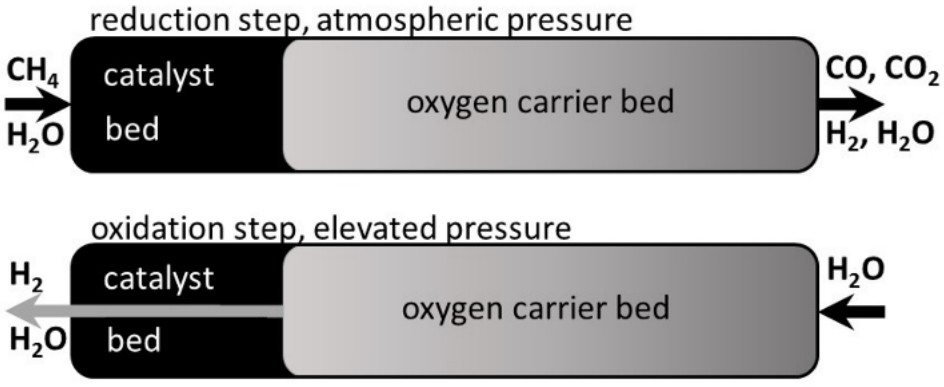

Figure 8: The reformer steam-iron process schematic with a reduction at atmospheric pressure and methane as fuel and a subsequent oxidation at elevated pressure in a fixed bed reactor.[54] ¥¥¥¥

Further improvements in the operation of the steam iron process were accomplished at Graz University of Technology. These enable the production of pure compressed hydrogen without additional gas compression. The pressurized oxidation is performed by pumping liquid water into the system which is evaporated in the heated inlet. The steam oxidizes the oxygen carrier by releasing hydrogen. The pressure build-up is achieved by closing the outgoing valve after the cooling system. The unreacted steam is condensed and the pressure increase can be directly related to the amount of produced hydrogen.

Successful proof of concept experiments of up to 11 bar(g) and a thermodynamic evaluation of the process were presented and explained in detail by Nestl et al..[55] A summary of the most important findings which were presented in this work are:

- It is necessary to perform the synthesis gas generation and the reduction of the oxygen carrier at ambient pressure to achieve high conversion efficiencies in the reformer steam-iron process
- It is possible to perform the steam oxidation at an increased pressure level
- Hydrogen produced with the reformer steam-iron process was obtained at a very high purity off 99.93% with only carbon dioxide as impurity.

The direct production of compressed pure hydrogen and its influence in the production process and hydrogen economy was investigated by previous publications. A general conclusion, which can be drawn from these sources, is that an higher production pressure, irrespective of the technology, reduces investments and energy demand for downstream compression and thus raises the system efficiency and the efficiency of the hydrogen infrastructure.[56,57]

The effects of an increased system pressure in chemical looping combustion CLC have been investigated by several other work groups. The feasibility of CLC systems with moving beds at elevated pressure has already been demonstrated by several sources.[58–63] However, their work primarily focused on the reduction behavior and the complete cycle under pressure with the oxidation performed with air/oxygen. Regarding the pressure behavior of oxygen carrier in cyclic redox systems two conflicting insights can be found in the literature. Several publications report a negative influence of an elevated pressure during redox reactions of different types of oxygen carrier.[59,64–66] Reduced reaction rates were measured, which resulted in extended kinetically controlled regimes. Hence, the reaction time is increased. The impact of pressure on the internal structure of the oxygen carrier is a probable explanation. A higher risk of solid carbon formation by a pressure elevation was also reported.[65] On the other hand some work suggest positive effects of a higher system pressure by increasing the carbon conversion indicated by an increased outlet-CO_2 concentration.[60–62] Thus a lower reduction degree of the oxygen carrier is achieved within the reaction time. The improved reduction was

observed from 0.1 to 0.5 MPa, while at higher pressure levels a worsening of the reaction kinetics became apparent.

The usual operation procedure in chemical looping systems maintains the pressurized condition during the complete cycle (reduction and oxidation), whereas the reformer-steam iron process benefits from the reduction under atmospheric conditions and the oxidation under elevated system pressure. Thus, the literature lacks of a comprehensive knowledge of the pressure behavior and the influences on chemical looping hydrogen systems.

1.1 Objectives and Structure

The primary purpose of the investigations presented in this thesis was to examine the chemical looping hydrogen technology under pressurized oxidation conditions. Based on previous work in our work group the specified objectives were defined as follows:

- Investigation of a preparation method for iron based oxygen carriers for the quick manufacture of different compositions
- The examination of the behaviour of oxygen carrier under pressurized oxidations in terms of cycle stability and structural integrity in the fixed bed reactor system
- Investigation of compressed hydrogen production from carbon based feedstocks. Evaluation of the impact of pressure on the hydrogen purity and the contaminations. Analysis of the correlation of pressure and coking behaviour.

This thesis is structured into six parts. The first segment introduces the issues of increasing energy demand, and the relations with CO_2 emissions and global warming. Decentralized chemical looping hydrogen generation is proposed as a possible transition from fossil fuels to renewable sources. The second chapter presents the recent advancements in scientific literature in the field of chemical looping water splitting technology. Chapter 3 discusses the oxygen carrier preparation method and analyzes the cycle stability of different sample compositions. Chapter 4 describes pressure experiments with pure hydrogen as reducing agent. The stability and structural integrity of an oxygen carrier is discussed. Chapter 5 presents the reductions with a syngas mixture and evaluates carbon contaminations at increased oxidation pressure. A conclusion in chapter 6 finalizes this thesis.

The work presented in this thesis has been published in peer-reviewed journals as follows:

Gernot Voitic and Viktor Hacker, *Recent advancements in chemical looping water splitting for the production of hydrogen,* RSC Advances 2016, **6**, 98267 – 98296.

Gernot Voitic, Stephan Nestl, Michael Lammer, Julian Wagner and Viktor Hacker, *Pressurized hydrogen production by fixed-bed chemical looping*, Applied Energy, 2015, **157**, 399 – 407.

Gernot Voitic, Stephan Nestl, Karin Malli, Julian Wagner, Brigitte Bitschnau, Franz-Andreas Mautner and Viktor Hacker, *High purity pressurised hydrogen production from syngas by the steam-iron process,* RSC Advances 2016, **6**, 53533-53541.

Stephan Nestl, Viktor Hacker and Gernot Voitic, *Verfahren zum Herstellen von Wasserstoff*, WO 2016011473 A1, PCT/AT2015/050177, issued 2016.

2 Recent advancements in chemical looping water splitting for the production of hydrogen

2.1 Introduction

Chemical looping hydrogen CLH, represents a promising technology that enables the use of renewable, CO_2 neutral resources and facilitates efficient CO_2 sequestration capabilities.[47] Historical, the chemical looping process for hydrogen generation was first introduced by Howard Lane as the "Lane Hydrogen Producer" in 1903 and used coal gas as reducing agent followed by a steam oxidation. This system was filed for patent in 1911 by Messerschmitt under the name "steam-iron process" (SIP).[67–69] The reactors were operated in a fixed bed with iron oxide as solid material in a cyclic operation mode at 750 °C. Hydrogen with a purity of 95 – 99% and a yield of 200 m³ per ton of coke was obtained.[67] In the following decades patents describing a continuous operation mode were granted to Parsons[70] and Marshall.[71] These inventions discussed the movement of oxygen carrier through the reactions zones by gravity and the recirculation by mechanical devices, for instance a conveyor belt. Substantial modifications were also discussed by Reed,[72] who utilized a three-reactor circulating fluidized system with the addition of an air oxidation reactor. Bergius[73] and Marshall mentioning improved operation conditions under elevated system pressure. The steam-iron process was successfully used for the commercial hydrogen supply in the first quarter of the 20th century but eventually it was replaced by the more cost competitive reforming process of hydrocarbons. Although the technology never again reached a commercially competitive status in the second part of the last century, research on the technology of hydrogen production by redox reaction of solid oxygen carrier continued successfully. Encouraging results were published, however due to economic considerations the steam-iron process never again progressed beyond testing operation.

Today sometimes still called the "steam-iron process", it is usually referred to as a modification of the chemical looping combustion process CLC and is thus named "chemical looping hydrogen" CLH, "chemical looping water splitting" CLWS or "cyclic water gas shift" CWGS. Generally, chemical looping technology (figure 9) uses a solid oxygen carrier which supplies oxygen for the combustion of a fuel while reduction the solid material (eq. 8). This omits the utilization of air as oxygen supply and thus enables the fuel conversion to a pure stream of CO_2 and H_2O, which can be easily separated by condensation. The solid material is re-oxidized with air to regenerate the depleted oxygen (eq. 9). The addition of a third reaction step enables the production of pure hydrogen by initially re-oxidizing the oxygen carrier with water (eq. 10). An air oxidation may still be executed to close the looping cycle but it reduces the hydrogen production rate and thereby the maximum efficiency of an integrated system as discussed by Hacker et al. in relation to different fuels.[46,50]

$$C_nH_{2m} + (2n + m)Me_xO_y \rightarrow mH_2O + nCO_2 + (2n + m)Me_xO_{y-1} \quad (8)$$

$$Me_xO_{y-1} + 0.5O_2 \rightarrow Me_xO_y \quad (9)$$

$$Me_xO_{y-1} + H_2O \rightarrow H_2 + Me_xO_y \quad (10)$$

This chapter surveys the very recent research data and scientific achievements presented in literature on the subject of hydrogen production by chemical looping technology. The studied publications were divided into the main sections (i) oxygen carrier development, (ii) reactor design, (iii) process development, (iv) process simulation and (v) kinetic studies. An overview of the evaluated data is presented in tables in the appendix section 8.2.

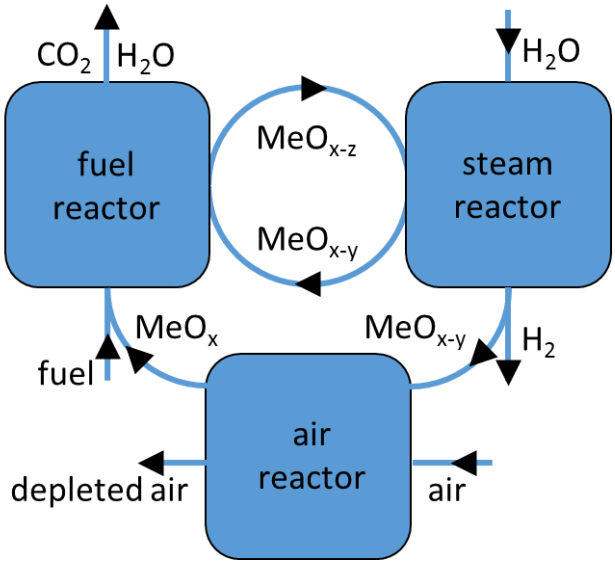

Figure 9: Process schematic of the chemical looping hydrogen production process with an air oxidation as third step.

2.2 Oxygen Carrier Development

The oxygen carrier functions as a transport intermediate to deliver pure oxygen without nitrogen dilution from the oxidizing stream, air or water, to the fuel. The utilization of a suitable oxygen carrier is of great importance in chemical looping systems for hydrogen production. Thus, a great deal of literature deals with improvements mainly implemented by means of two different approaches, (i) optimizing the composition or (ii) optimizing the particle structure. A summary of the utilized oxygen carrier is presented in section 8.2, table 7. Key properties for industrial applications, which must be met by suitable oxygen carriers are:[28,74–83]

- A high oxygen exchange capacity
- Favourable thermodynamics and reactivity regarding the selected fuel for the reduction reactions
- A low risk of carbon formation
- Structural stability under continuous reduction and oxidation cycles
- High reactivity in the oxidation reactions
- Good fluidization properties and resistance to attrition, which is important in fluidized reactor systems
- Feasible material and production costs
- Environmental friendly characteristics.

Various metals viz. Fe, W, Sn, Ni, Cu, Mn and Ce have been tested as the main active component. However, the more recent work almost exclusively investigated iron based oxygen carrier.[84] As pure metals do not fulfil the listed requirements, inert components such as ZrO_2, TiO_2 SiO_2 Al_2O_3 as additives are used to improve the mechanical and chemical properties.[85] Additionally, the active component can be incorporated into a mineral structure, for instance a perovskites or a spinel structure, which are known for their mechanical resistance or two active metals are combined as a bimetallic oxygen carrier to generate synergetic effects of their components.[86]

2.2.1 Zirconia as additive

Liu et al.[87] achieved a stable hydrogen yield of 90% based on the theoretical value over 20 cycles by adding up to 30 wt% of ZrO_2. The structural analysis revealed partial sintering of iron particles but the pore structure was maintained and no chemical interaction between the active redox component and the support, which leads to the unreactive component Fe-Zr-O, was observed. Cho et al.[88] analyzed the structural changes of an oxygen carrier with a 20 wt% loading of Fe_2O_3 on ZrO_2 at 750 °C. After 10 redox cycles the iron particles were homogenously distributed with only slight signs of sintering as long as a deep reduction was avoided and reduction was stopped at wustite. However, after deep reductions to Fe, diffusion of iron particles to the outer regions and significant growth of iron grains were found. Therefore,

samples reduced to wustite performed better in terms of hydrogen yield. The oxygen carriers were successfully applied in a fixed bed reactor at 800 °C using methane as the reducing feed.[89] The redox reaction results were used to determine the design guideline for a 1 MW_{th} chemical looping plant with a bed inventory of 170 – 220 $kg \cdot MW_{th}^{-1}$. The stability was further enhanced by using an yttrium-stabilized zirconia (YSZ) defect support, which provides strong support and inhibits iron sintering.[88] The iron diffusion, which leads to uneven distribution of active metal and support, can be avoided by preventing particle sintering. It was found that the stability was increased by an activation process consisting of 10 cycles of reduction including air-oxidations. The formation of large cracks and pores occurred, which directed the iron diffusion towards the newly formed cavities. Thus, a heterogeneous particle distribution was maintained. Samples, which underwent an activation method, provided higher reduction rates using methane as feed compared to reference samples without the prior treatment. Kosaka et al.[90] reported similar improvements of redox behavior with iron oxide supported by yttrium-stabilized zirconia (YSZ) compared to Fe_2O_3/ZrO_2 reference samples. A positive correlation between the reduction rate constant and the oxide ion conductivity of YSZ due to Y-doping was observed in the reduction step and the oxidation reaction. Improved reaction rates compared to ZrO_2 were reported, when using samples with CeO_2 and $Ce_{0.8}Gd_{0.2}O_{2-\delta}$ (GDC) support. In contrast to the enhanced ion conductive of YSZ, CeO_2 and GDC increase the electronic conductive and accelerate the reduction kinetics of FeO to Fe significantly (figure 10).[86] This suggests that oxygen vacancy formation by cerium plays an important role in the acceleration of the redox reaction. The GDC support, which contained both attributes, the ion- and electric conductivity, possessed the highest performance in redox experiments at 550 – 800 °C with hydrogen as reducing feed followed by a steam oxidation.

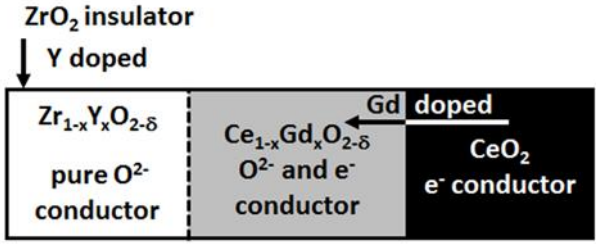

Figure 10: Physical properties of the support materials utilized by Kosaka et al.[90] §

2.2.2 CeO_2 as active component

The stabilizing effects of a ZrO_2 support with CeO_2 was investigated by Zheng et al..[91] Samples with a metal ratio of Ce/Zr = 8/2 and with pore sizes ranging from 100 – 200 nm were prepared using the colloidal crystal method. The pore sizes were controlled by the sizes of the PMMA template spheres. A nonporous sample prepared by co-precipitation was used as a reference sample. H_2-TPR measurements revealed a single reduction peak (at around 650 °C) for the macro-porous samples, whereas the nonporous oxygen carrier showed two separated reduction peaks, which can be related firstly to the exchange of bulk oxygen (600 °C) and secondly to the lattice oxygen (900 °C). The merging of the two reduction peaks suggested an

improved mobility of lattice oxygen in the macro porous samples, which enhanced its reducibility. Cyclic experiments were performed in a fixed bed quartz reactor at 800 °C using methane as reducing agent. The macro porous samples indicated an average methane conversion ranging from 46-50% and a H_2/CO ratio approaching the stoichiometric value. The hydrogen consumption increased with declining pore sizes. The methane conversion of the nonporous sample was 4% points lower with a H_2/CO ratio of two, which suggested methane cracking induced by a deficiency of oxygen, and thus an increased risk of carbon formation. A similar trend was observed in steam oxidations. A declining pore size raised the hydrogen production rate and the amount of hydrogen. Stability measurements over 10 cycles revealed a clearly visible continuous decrease of produced hydrogen. SEM images showed that the three-dimensionally ordered macro-porous structure had collapsed, however the samples maintained a sufficient porosity. The influence of different calcination temperatures on redox performance and structural traits of the proposed macro-porous CeO_2-ZrO_2 oxygen carrier samples were studied.[92] Increasing calcination temperatures from 450 °C to 850 °C changed the structure due to the growth of larger grains. Lower calcination temperatures resulted in higher structured samples (figure 11), which yielded better CH_4 conversions and H_2/CO ratios. A similar trend for the steam oxidation was observed, a decreasing hydrogen production rate with increasing calcination temperature. The results suggest that the structural properties of $CeZrO_2$ strongly influenced the mobility of lattice oxygen, thus effecting conversion efficiency during the redox reactions. All samples revealed a loss of produced amount of hydrogen after 10 consecutive cycles. However, a high calcination temperature led to a complete loss of the initial macro-structure but preserved the microscale porosity (figure 11). Lower calcination temperatures stabilized the three dimensional structures, even if the samples were used at high reaction temperatures. Nevertheless, stability experiments indicated a gradual loss of the skeletal structure, which left the long term cycle stability disputable.

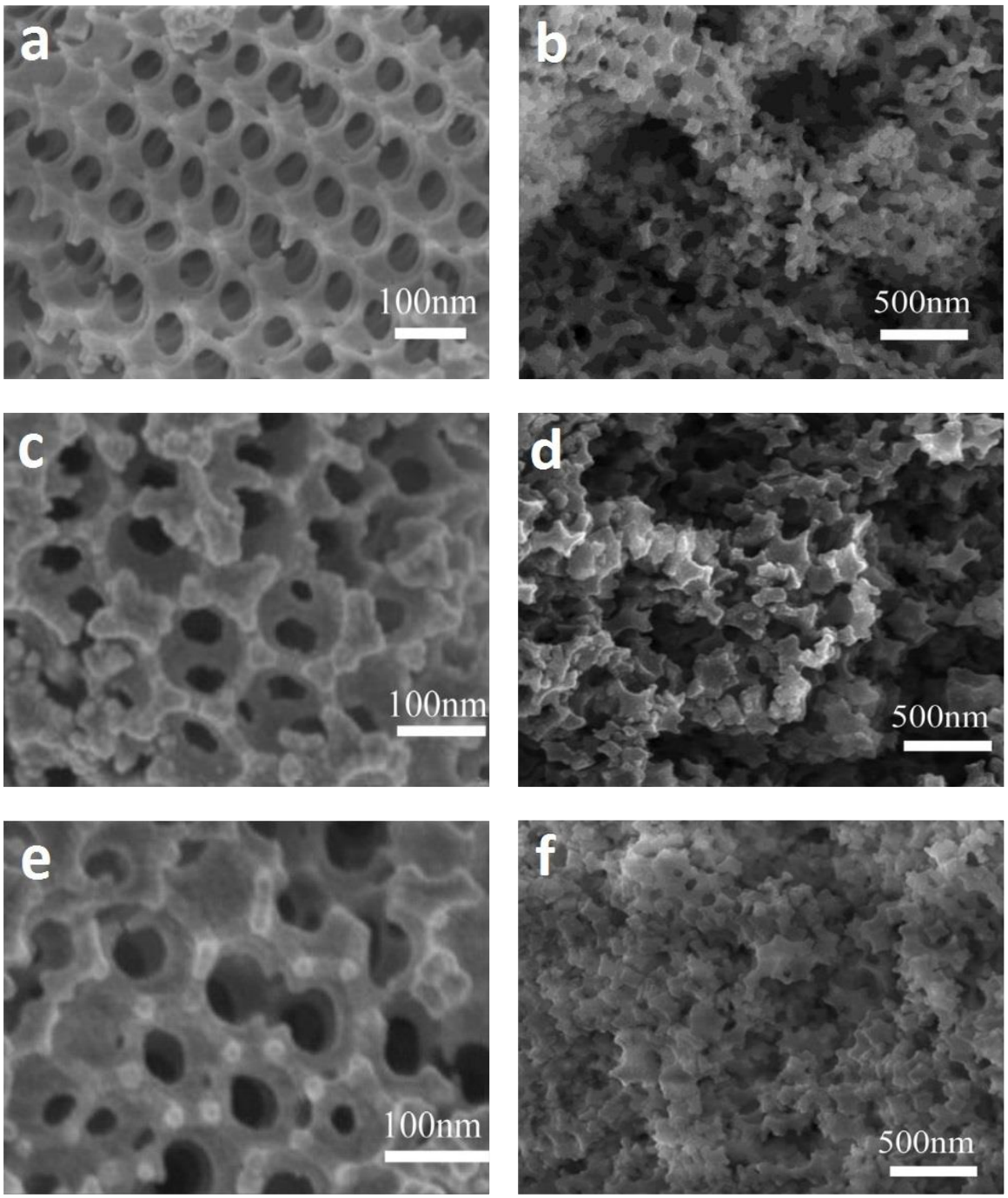

Figure 11: SEM images of CeO_2/ZrO_2 oxygen carriers. Left column: fresh samples after a calcination step, right column: after 10 redox cycles. Samples were calcinated at different temperatures: (a), (b) 450 °C; (c), (d) 750 °C; (e), (f) 850 °C.[92] §§

2.2.3 CeO_2 as additive

Synergetic effects of a mixture of CeO_2 and Fe_2O_3 were investigated by Zhu et al..[84,93] CeO_2 was used as support material with iron oxide dispersed on the surface. Fe^{3+} was partially imbedded in the CeO_2 lattice structure, thus changing the chemical properties of the particles. An enhanced reducibility of the mixed Ce-Fe oxide was observed in H_2-TPR measurements and CL-SMR at temperatures of 800 – 900 °C with a higher lattice oxygen mobility compared to

single oxides. An increasing iron content raised the amount of released hydrogen in the oxidation step due to the high oxygen intake capability. The sample with the molar ratio of Ce/Fe = 1 was selected for 10 consecutive cycles with fixed reduction and oxidation reaction times at 850 °C. A steady decrease of the CH_4 conversion from roughly 63% to 55% was observed, while the amount of produced syngas and the H_2/CO ratio remained unchanged. The oxidations showed only a slight decline in the produced hydrogen with no carbonaceous impurities. During the methane reduction step, the formation of $CeFeO_3$ occurred by means of a solid−solid reaction, which was re-oxidized to CeO_2 and Fe_3O_4 during the steam oxidation step. However, a Ce−Fe−O phase equilibrium was preserved with constant composition during the redox process, thus increasing the oxygen mobility by the formation of abundant oxygen vacancies. Gu et al.[94] reported a significant improved reducibility of surface and bulk oxygen in iron oxide supported with CeO_2 prepared using the co-precipitation method. Samples produced by mechanical mixing exhibited only a slightly better performance. Thus the formation of a solid solution of $CeFeO_3$ and the structural change, which were strongly related to the synthesis method, were key to enhancing the redox performance. The increasing Ce content increased its specific surface which reached a maximum at the composition of Fe/Ce=80/20 and decreased afterwards. Small Ce-particles with a high dispersity and strong chemical interaction were formed and stabilized the structure after several redox cycles. The improved stability of iron oxide particles by adding Ce was also reported by Romero et al.[95] Small amounts of CeO_2 were added to iron oxide supported on Al_2O_3 with the final composition of $Fe_2O_3/Al_2O_3/CeO_2$ 98/1.75/0.25%. The sample did not suffer from any deactivation during 17 cycles at 500 °C when fully oxidized, but the cycle time slightly increased.

2.2.4 MoO_3 as additive

When replacing CeO_2 with MoO_3 with a content of 0.25%, a better steam oxidation behavior was observed, however a reduced cycle stability, especially within the first 8 cycles led, to a decreasing amount of produced hydrogen.[95] The combined addition of CeO_2 and MoO_3 did not improve either the redox behavior or stability. Datta et al.[96,97] impregnated iron oxide samples supported on 20 wt% $Ce_{0.5}Zr_{0.5}O_2$ with different molybdenum concentrations to achieve a final Mo loading of 0.96 – 5.5 wt%. The formation of a spinel-type ferrite $Mo_xFe_{3-x}O_4$ was reported, which inhibited the contact between the iron particles and impeded the deep reduction from FeO to Fe. This hindered sintering and deactivation of the active component. The increasing Mo content led to a higher temperature for the reduction with hydrogen and a higher air-oxidation temperature. However, decreasing reduction activation energy with increasing molybdenum content was observed. A significant improvement in stability was reported for Mo-impregnated samples compared to a reference Fe_2O_3–$Ce_{0.5}Zr_{0.5}O_2$ sample. A Mo content of ≥ 1.5 wt% preserved a hydrogen production amount of at least 90% from the theoretical value after 100 cycles at 750 °C. A further extended stability test with 200 cycles revealed a loss of 10% from the initial amount of produced hydrogen within the first 40 cycles followed by a stable production afterwards. The trade-off for higher stability was the amount

of produced hydrogen per cycle, which was only 30 – 34% of the amount theoretically possible. Wang et al.[98] reported a decrease in the activation energy by adding small amounts of Mo < 10 mol%. TPR experiments revealed a shift of the reduction peak of iron towards lower temperatures from 610 °C to 572 °C. A third broad peak at 758 °C was visible, which was related to the reduction of Mo^0 and to the formation of $Fe_2Mo_3O_8$. An increased production rate and higher amount of hydrogen during steam oxidation were measured. A shift to lower oxidation temperatures was observed from 400 °C to 350 °C, with the sample consisting of 8 mol% Mo revealing the best performance.

2.2.5 CaO as additive

Improved stability of iron based oxygen carriers by the combination with CaO was investigated by some work groups.[99–101] Datta[99] added 2.5 wt% CaO to Fe_2O_3 samples supported with either SiO_2 (7.5 wt%) or Al_2O_3 (5 wt%). The combination of SiO_2 and CaO enabled a stable hydrogen yield of 95% of its initial value over 100 cycles as long as the reaction temperature remained below 750 °C. A significant stability loss was observed at higher temperatures caused by the agglomeration of SiO_2. The sample with Al_2O_3 and CaO stabilized the oxygen carrier to a hydrogen amount of 70 – 80% of its initial value after 100 cycles. Datta suggested that the formation of CaO formed a dispersed ferrite structure, which inhibited sintering. Ismail et al.[100] prepared mixtures of Fe_2O_3 with 50 mol%, 57.3 mol% and 66.7 mol% of CaO. After calcination CaO, $CaFe_2O_4$, $Ca_2Fe_2O_5$, CaO and Fe_2O_3 were identified in the different samples depending on the mol% of CaO. Deviations from the expected equilibrium compositions were detected as a result of inhomogeneous mixing and slow solid-state diffusion during the calcination process. The calcium ferrite samples were successfully reduced with CO and H_2, forming the stable component $Ca_2Fe_2O_5$, and efficiently re-oxidized with CO_2. Equilibrium partial pressure values suggest that the oxidation of $Ca_2Fe_2O_5$ enables a higher steam conversion to hydrogen compared to the unmodified iron to wustite oxidation. The mixed metal ferrites achieved a stable gas conversion during consecutive redox reactions over 20 cycles, whereas the pure iron sample, which started with a high amount of exchanged-oxygen/sample-mass, indicated a loss of approximately 90% within 10 cycles. Deep reduction experiments resulted in the formation of segregated phases of Fe and CaO, hence a significant degradation of the cycle stability. Fluidized redox experiments indicated high attrition losses of the calcium ferrite samples of 4 – 6 %wt. Thus, the mechanical strength needs to be improved for industrial applications. Chan et al.[101] observed high steam conversion efficiencies with an equilibrium composition of 75/25 mol% H_2/H_2O in a single oxidation step using a $Ca_2Fe_2O_5$ sample. A complete recovery to the initial stage of $Ca_2Fe_2O_5$ was achieved without the requirement of an air oxidation. The amount of released hydrogen was 88.9% compared to a Fe_2O_3/ZrO_2 reference sample. However, $Ca_2Fe_2O_5$ suffered from a slow reduction rate, which was about twice as long as pure iron oxide caused by an unfavorable reduction equilibrium. To overcome the trade-off and utilize the higher steam oxidation efficiency a combination of two oxygen carriers in two reactors was suggested. During reduction the feed initially reduces the $Ca_2Fe_2O_5$ containing bed. The off-gas can still convert a pure iron oxide bed and enables

complete conversions to CO_2 for efficient carbon sequestration. During oxidation the flow direction changes and passes first through the iron bed and finally through the CaO+Fe bed. Thus, the higher steam conversion capabilities are utilized.

2.2.6 Al_2O_3 as additive

It is well known that the addition of Al_2O_3 can stabilize the cycle stability of iron based oxygen carriers. However sample studies of deeply reduced iron oxide supported by Al_2O_3 have shown that the formation of unreactive hercynite $FeAl_2O_4$ occurred.[102–105] Liu et al.[106] investigated possibilities for inhibiting the formation of hercynite and preserving the initial reduction rates by adding Na2O and MgO. These additives were expected to prevent the formation of $FeAl_2O_4$ by forming the stable compounds $MgAl_2O_4$ and $NaAlO_2$ instead, which also act as support materials. The two oxides were prepared by precipitation with the compounds Fe, Al and Na (NAFO) and Fe, Mg, Al and Na (NMAFO). When cycled under conditions suitable for producing hydrogen at 1123 K, both oxygen carriers showed stable performance over 20 cycles, demonstrating approximately 100% and 80% of their theoretical hydrogen capacities, as long as an air oxidation was included in each step. Cycle experiments without air oxidation revealed a conversion loss of roughly 50% for NAFO, while the NMAFO sample retained its stability regardless of the oxidation procedure. The gradual formation of $NaFeO_2$ led to free Al_2O_3 and the formation of hercynite in consecutive cycles. However, in the presence of Mg^{2+} cations, Al_2O_3 formed the stable compound of $MgAl_2O_4$ thus stabilized the NMAFO sample (figure 12).

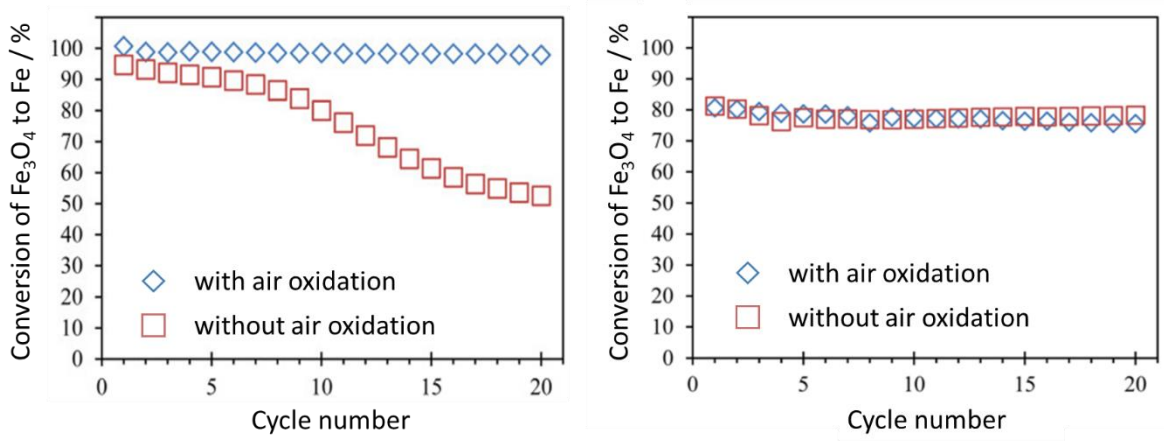

Figure 12: The conversion degree of Fe_3O_4 to Fe as a function of cycle numbers with 0.3 g of NAFO (left) and NMAFO (right) in a packed bed reactor at 850 °C with or without an air oxidation step.[106] §§§

2.2.7 Natural minerals as oxygen carrier

The application of oxygen carriers from natural deposits in chemical looping has attracted the attention of several research groups in the past.[107–109] Ku et al.[110] considered the utilization of natural-ilmenite (Fe_2TiO_5) as an inexpensive and abundant oxygen carrier. In a segmented reduction the sample was gradually reduced to Fe_2TiO_4 and $FeTiO_3$ and finally Fe and TiO_2. The

consecutive air oxidation led to the formation of a sample containing only Fe_2O_3 and TiO_2. Hydrogen generation by steam oxidation was feasible at 900 °C and Fe_3O_4 and $FeTiO_3$ were found in the oxidized sample. The stability tests showed no significant changes at 900 °C after 100 cycles with an oxygen storage capacity of approximately 33%. Sample analysis revealed agglomerated structures of Fe_2O_3 but due to the presence of cracks and pores, the reactivity was maintained. Xiao et al.[111] compared ilmenite with different natural iron ores in a reducing feed using different CO/N_2 ratios. The ilmenite samples had the lowest weight loss during the reduction because of the lower iron oxide content, however a very high resistance to solid carbon and iron carbon formation was observed. Tong et al.[112] suggested that the introduction of Fe_2O_3 in a TiO_2 network leads to the formation of lattice substitution and interstitial defects in the support framework. These defects increase the rate of oxygen anion diffusion. In unsupported iron oxides the outward iron cation diffusion was dominant, whereas in a supported iron oxide, like ilmenite, both the outwards diffusion of iron cations and the inwards diffusion of oxygen anions occurred. Liu et al.[113] impregnated natural hematite, which consisted of Fe_2O_3 supported with SiO_2 and Al_2O_3, with a solution of KNO_3, to achieve a loading of 10 wt% KNO_3. After calcination, $K_2Fe_4O_7$ and $K_2Fe_{22}O_{34}$ were found in the samples, which showed signs of sintering and displayed a lower degree of porosity than the unmodified ore. Redox experiments were performed in a fluidized bed reactor at temperatures ranging from 750 – 900 °C with CO as feed followed by steam oxidations. A loading of 10 wt% KNO_3 significantly accelerated the reduction reaction and enabled a greater reduction degree of the iron oxide. Thus, higher amounts of hydrogen were obtained in the consecutive oxidations. Additionally by reducing the reduction time and increasing carbon conversion efficiency less coking occurred. The cycle stability was improved efficiently without the loss of produced hydrogen by maintaining a porous structure, whereas the unmodified ore lost 24% of its initial production capacity (figure 13).

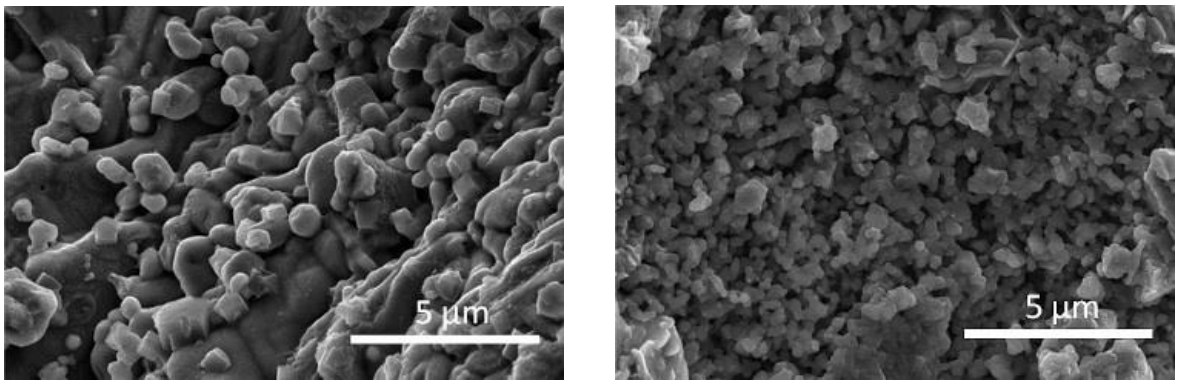

Figure 13: SEM images of the oxygen carrier after 10 cycles, original iron ore (left) and iron ore loaded with 10 wt% KNO_3 (right).[113] §§§§

2.2.8 Bimetallic oxygen carrier

Chiron et al.[114] proposed the use of a bimetallic oxygen carrier to enable a synergetic effect of different redox behavior of two metal oxides CuO and Fe_2O_3. In contrast to other metal oxides CuO is reduced by methane by releasing heat. Combining CuO with endothermic reacting metal oxides can reduce the external heat demand and lower the heat transfer requirement to the fuel reactor. Samples supported by Al_2O_3 consisting of either pure Fe_2O_3, pure CuO or a bimetal with varying compositions were prepared by an incipient wetness impregnation (IWI) and co-precipitation (CoPr) method. Most samples prepared by (CoPr) could not be fluidized since large slugs were observed that filled the entire cross-section of the reactor and an unsteady pressure drop occurred. Samples prepared by IWI were easily fluidized and reached their maximum solid conversion by steam oxidations significantly faster than samples prepared by CoPr. The bimetallic samples revealed a low solid conversion of approximately 10% irrespective of the preparation method. The highest conversion of 27% was measured with pure iron prepared by co-precipitation.

2.2.9 $CoWO_4$ as oxygen carrier

$CoWO_4$ has been reported as a suitable oxygen carrier for hydrogen production with methane as the reducing feed.[115] De los Ríos Castillo et al.[115] impregnated cobalt tungstate $CoWO_4$ with Ni and La_2O_3 to enhance its reactivity towards methane reduction. Reduction experiments at 850 °C with CH_4 indicated improved reaction rates up to 6 and 2.5 times by the addition of 10 wt% Ni and 10 wt% La respectively. However, the reactivity improvements diminished gradually at increasing reduction temperatures. In the second cycle the unmodified $CoWO_4$ sample displayed higher reduction rates compared to the first cycle. This was related to the incomplete re-oxidation of Co by steam and the catalytic activity of the metal species. Nevertheless, samples promoted with Ni and La had improved reactivity but with smaller margins. Similar trends were reported regarding the activation energies. The inclusion of Ni and La significantly reduced the activation energy and thus improved reducibility. Again, the difference between the promoted samples and the reference sample disappeared after the first cycle.

2.2.10 Perovskites

Perovskite structured oxygen carriers are reported to have a good thermal stability and a high ionic and electronic conductivity.[116,117] Zhao et al.[118] studied three-dimensionally ordered macro-porous (3DOM) $LaFeO_3$ and nano-$LaFeO_3$ perovskite oxides synthesis gas and pure hydrogen using CH_4 as fuel. 3DOM-$LaFeO_3$ enabled a stable partial oxidation of methane at 850 °C in a fixed bed reactor over 10 cycles. An average methane conversion of 50% and the production of hydrogen by steam oxidation with small amounts of CO_2 was achieved. The amount of released hydrogen decreased within the first 3 cycles but remained stable afterwards. The nano-$LaFeO_3$ enabled both a very high methane conversion > 90% and a high molar ratio H_2/CO of 9 in the first cycles, which meant a high risk of carbon formation. Within

10 cycles the methane conversion decreased and ended up below the 3DOM-$LaFeO_3$ sample. The three-dimensional skeletal structure in the fresh sample gradually collapsed within repeated cycles caused by thermal and chemical stress. This led to a decrease in crystallinity and grain sizes, nevertheless a porous structure with little agglomeration was maintained, which preserved a stable cyclability (figure 14).

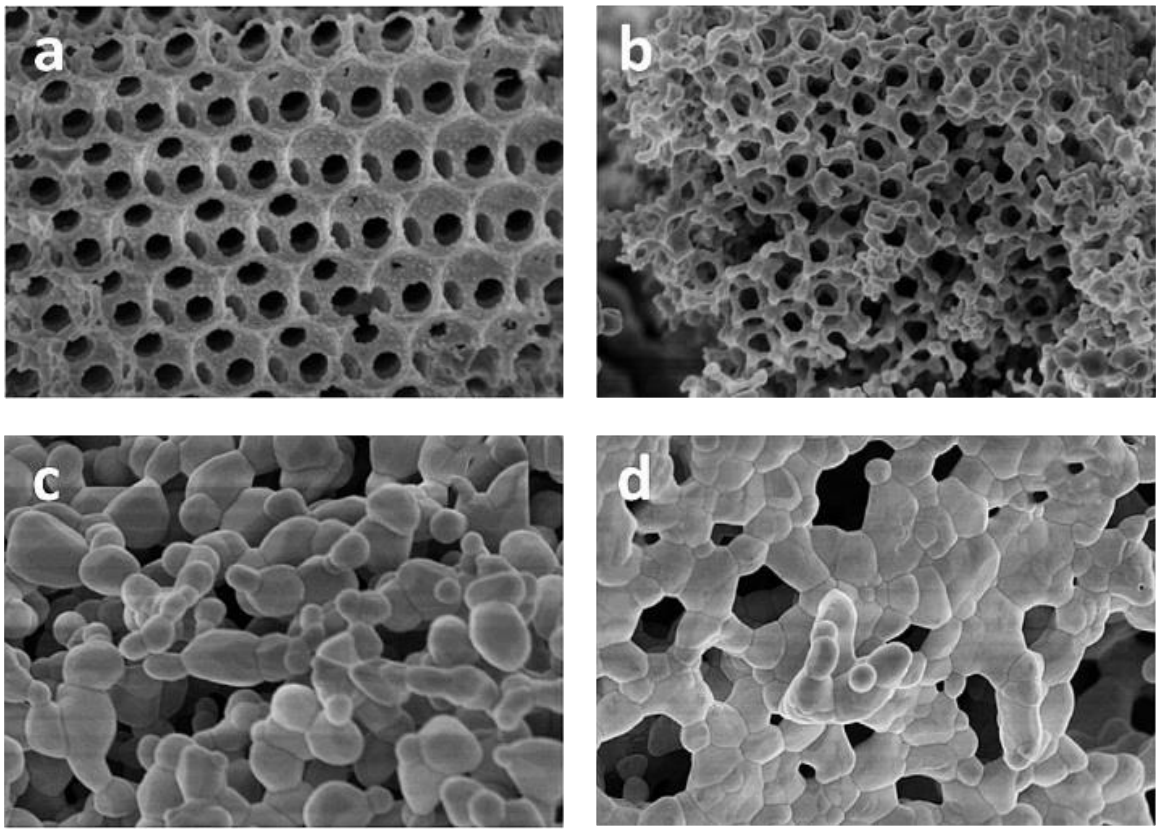

Figure 14: SEM images of three-dimensionally ordered macro-porous $LaFeO_3$. A fresh sample (a), after 1 cycle (b) and after 10 cycles (c). A nano-structured-$LaFeO_3$ after 10 cycles is depicted in (d).[118] §§§§§

Zhao et al.[119] further enhanced the performance of $LaFeO_3$ perovskite oxides by doping with Co, which is expected to increase the vacancies sites, thus improving the redox activity.[120–122] Perovskite-type oxides $LaFe_{1-x}Co_xO_3$ maintained their crystalline structure despite the doping with Co. An increasing Co content resulted in a higher concentration of oxygen vacancies, in a greater resistance to reduction and in a longer period of time required to reach a stable fuel conversion of > 90%. Nevertheless, all sample compositions were completely reducible, indicated by the appearance of La_2O_3, Fe_2O_3, FeO, CoO and Co. A Co molar ratio of 0.3 and 0.5 yielded the best performance regarding low risk of carbon formation, amount of produced hydrogen and stable CH_4 conversion. Hence, $LaFe_{0.7}Co_{0.3}O_3$ was used for consecutive redox cycling experiments. A steady feed conversion of 86% was achieved over 20 cycles with slight improvements within the first 5 cycles. A hydrogen production potential of 4 $mmol \cdot g^{-1}$ was obtained with an average purity of 96%. Post experimental analysis revealed degradation

caused by sintering but these degradations were compensated by an increased oxygen vacancy concentration. Liang[116] investigated the effects of CeO_2 on perovskite supported iron oxides (Fe_2O_3 15 wt%, CeO_2 5 wt%, $LaNiO_3$). The addition of cerium oxide slightly reduced the pore volume and pore diameter by partially filling void zones with CeO_2. TPR experiments indicated a shift of the three iron oxide reduction peaks to lower temperatures, which suggests the promotion of the reduction reaction. In addition, the appearance of a fourth peak at 520 °C was observed, which corresponded to the reduction of CeO_2. Redox experiments were executed in a fixed bed reactor at 800 °C, consisting of a reduction with CH_4, a steam oxidation and a final air oxidation. The reference sample without CeO_2 exhibited a complete methane conversion and a stable hydrogen production. After 57 cycles, a sharp drop in the hydrogen yield was measured, which was a result of the decomposition of the perovskite structure, leading to isolated Fe_3O_4 and FeO. The sample enhanced by CeO_2 did not suffer from deactivation over 100 redox cycles, with a stable hydrogen yield slightly lower than the reference sample. The formation of a solid solution of $CeFeO_3$ was observed, which increases the oxygen content and improves stability and activity.

He et al.[123] used the perovskite $La_{0.8}Sr_{0.2}FeO_{3-\delta}$ (LSF) as a supplement to iron oxide for a higher steam conversion efficiency during the steam oxidation step. $La_{0.8}Sr_{0.2}FeO_{3-\delta}$ is harder to reduce but offers a high resistance to carbon deposition. A reactor with a two-layer filling was proposed, consisting of an iron oxide rich phase at the bottom with small amounts of LSF to prevent loss of stability by sintering and a LSF layer at the top (figure 15, right). Reduction reactions were executed with CH_4 supplied from the top, which yielded an average methane conversion of 99% and a syngas production efficiency of 62%. After the reduction the LSF layer consisted of Fe, La_2O and small amounts of $LaSrFeO_{4-\delta}$. The oxidations were performed by supplying steam from the bottom, which initially oxidized the iron rich layer to iron oxide. The gas mixture, which consisted of 62.3% H_2 and 37.7% steam, was able to oxidize the upper layer further by forming $La_{0.8}Sr_{0.2}FeO_{3-\delta}$ resulting in a total steam conversion of 77.2% and a hydrogen purity of 98.5% (figure 15, left). The higher steam conversion efficiencies are expected to significantly increase the process efficiency. The material characteristics with a high oxygen defect concentration of the LSF are responsible for the high affinity towards steam oxidation. The total amount of exchanged oxygen of the LSF was little compared to the iron rich layer, but the favorable thermodynamic equilibrium enabled a higher steam conversion efficiency. Galinsky et al.[86] reported significant reduction rate improvements by supporting iron oxide on LSF. Experiments were performed with H_2, CO and CH_4 in a TGA system. A faster reduction rate resulting in a higher degree of solid conversion and a high reactivity at lower temperatures were reported. Two material properties were attributed to the performance increases. Firstly, the electronic and ionic mixed conductivity enabled efficient transport of O^{2-}-ions in the solid material and a full accessibility of bulk oxygen. Secondly, Fe_2O_3 crystallites with small grain sizes of 100 µm were distributed evenly within the LSF support. Compared to TiO_2 supported samples, a reduction rate acceleration of one magnitude was observed. The LSF samples indicated very high cycle stability with a capacity loss of 4% within 50 cycles.

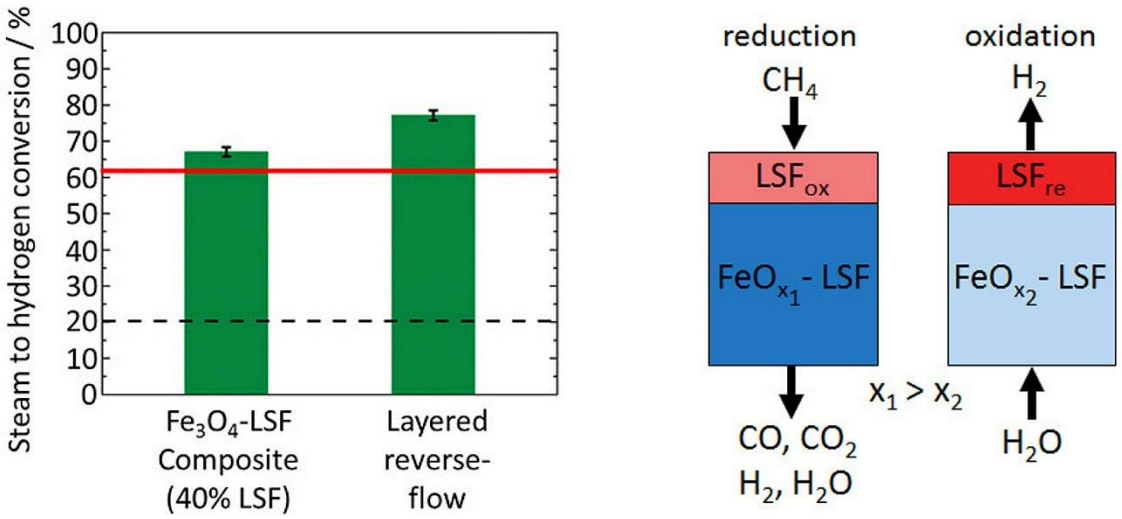

Figure 15: Left: steam to hydrogen conversion at 930 °C. The red line displays the thermodynamically maximum conversion. Right: schematic of the proposed layered reverse-flow redox process.[123] §§§§§§

2.2.11 Oxygen carrier with spinel structures

Spinel structured ferrites have been widely investigated widely in the last couple of years. Modifying physical and chemical properties by selecting suitable cations offers the prospect of preparing a specific oxygen carrier optimized for the selected application and a structural stability at high reaction temperatures and mechanical stress.[124–127] Aston et al.[83] investigated two mixed metal spinels, $NiFe_2O_4$ and $CoFe_2O_4$ prepared by incipient wetness method, with ZrO_2 as substrate. The Ni ferrite and Co ferrite were expected to possess higher reducibility with H_2 and CO and to be fully re-oxidized by steam.[128] The reductions of the oxygen carriers were performed with syngas until a breakthrough of H_2 and CO was observed. A period of full syngas conversion greater than 99% was visible, followed by a gradual increase of H_2 and CO. The complete oxidation of the two spinel samples with steam took significantly longer than the oxidation of a pure iron reference sample. After an initial high steam conversion an extended transition phase with a low conversion efficiency was observed, which resulted in reaction times that were 3 times and 16 times longer for $CoFe_2O_4$ and $NiFe_2O_4$ respectively. Both samples were finally fully re-oxidized. Compared to pure iron a higher amount of hydrogen with a factor of 7 – 9 per mass of metal oxide can be generated, while maintaining a full syngas conversion during the reduction. However, in an industrial application the impact on the system efficiency due to the low steam conversion needs to be addressed.

$CoFe_2O_4$ spinel structured oxygen carriers using methanol as a reducing agent were investigated by Crocella et al.[129] and Cocchi et al..[130] Samples were prepared by co-precipitation and calcined at either 450 °C (CF450) or 750 °C (CF750). In the first reduction cycle at 300 °C the CF450 exhibited significantly faster reduction rates compared to CF750 and reached a complete solid conversion, which was attributed to a higher active surface and the presence of larger amounts of surface octahedral sites. In both samples the formation of iron carbide Fe_3C was detected, which decomposed to Fe and solid carbon and acted as a carbon

source during the steam oxidation. The amount of Fe_3C increased with the reaction time and the formation was intensified at higher temperatures. When comparing the influence of the different calcination temperatures, it was found that the ratio between the Fe_3C and the CoFe alloy was lower in the CF750 sample. Several consecutive redox cycles indicated that the CF450 sample underwent irreversible structural changes, which resulted in an increase in crystallinity and loss of active octahedral sites, while the CF750 retained its structural origin state. Eventually, both samples possessed similar structural attributes. After the steam oxidations the presence of Fe_3O_4 was found, which revealed that a full recovery of the oxidized state was not possible, due to kinetic restrictions. Additionally, an incomplete removal of carbon was visible, meaning that an accumulation over several cycles occurred. This oxidation behavior suggested that a final air oxidation is required to remove solid carbon and to regenerate the oxygen carrier. Trevisanut et al.[131] analyzed the spinel $NiFe_2O_4$ as an oxygen carrier using ethanol as a reducing agent. Samples prepared by co-precipitation were studied in a fixed bed reactor at 450 °C. A high ethanol conversion, close to 100%, and a high activity was reported. The $NiFe_2O_4$ oxygen carriers led to a higher amount of fully oxidized components compared to pure iron oxide, which suggests greater accessibility of surface oxygen. The spinel sample enabled an enhanced reduction rate, despite it having similar surface areas to Fe_3O_4. Hence, the redox reactivity might be attributed to an increased mobility of bulk oxygen. The presence of separated Ni and NiFe alloy was observed after a steam oxidation at 450 °C, indicating an incomplete oxidation due to slow oxidation kinetics. Hydrogen was obtained with significant amounts of CO_2 and CO, which were related to carbon formation during the reduction. Sample analysis reassured the presence of iron carbides and solid carbon during the reduction. To overcome this incomplete steam oxidation Vozniuk et al.[132] prepared binary and ternary ferro-spinels $M^1_{0.6-x}M^2_xFe_{2.4}O_y$ using Co and Mn with different atomic ratios from x = 0 to 1. Samples with uniform morphology and particle size distribution were obtained. The integration of the metal cations strongly modified the reducibility towards hydrogen by changing the structural characteristics and the oxygen mobility. Direct ethanol reduction experiments in a fixed bed quartz reactor identified acetates and carbonates as the primary intermediates of the redox reaction if Co modified oxygen carriers were used, while samples with solely Mn as additives exhibited a complete absence of carbonates and a reduced reactivity. An initial complete ethanol conversion was achieved with all oxygen carrier samples. The concentrations of CO_2 and CO suggested that the partial oxidation of ethanol was the main reduction route. Acetone, which indicated the aldol reaction route and the decomposition of ethanol to acetaldehyde was detected in the beginning and decreased over time. With the ongoing experiments the amount of coke and higher hydrocarbons was increasing due to the limitation of exchangeable oxygen in the oxygen carrier. It was concluded that the modification of Co improves the reducibility of oxygen carriers with ethanol, while Mn enhanced the resistance to coking, but did not completely exclude it. $Co_{0.3}Mn_{0.3}Fe_{2.4}Oy$ was identified as the most promising candidate because of its high hydrogen yield during reduction and a significantly reduced carbon formation. The complete carbon conversion was not achieved during the oxidation, which still required a final carbon removal step by air. Kuo et al.[133] investigated a NiAl-spinel ferrite

$NiFeAlO_4$ as oxygen carrier for hydrogen generation. After a calcination temperature of 1300 °C a single cubic spinel phase of $NiFeAlO_4$ was observed with a crystalline size distribution between 100 – 300 nm. After a complete reduction Al_2O_3 and the bimetal FeNi was formed, which possessed a high porosity and efficiently prevented agglomeration by a large triple phase boundary area. The oxygen carrier was submitted to 10 consecutive redox cycles to investigate the cycle stability. The amount of weight loss increased within the first four cycles, possibly by the formation of additional pores by the phase changes and finally stabilized without any signs of degradation. A slight decrease of the redox reaction rate was observed. The steam oxidation yielded hydrogen and a phase mixture of Ni, Fe_3O_4 and Al_2O_3, which was oxidized by air to the original spinel phase. Bhavsar et al.[134] focused on preparing a nanostructured oxygen carrier support based on barium hexaaluminate (BHA). A carrier structure with a high porosity and sponge-like nanostructure, which suppressed migration and prevented sintering, was obtained. Depending on the application, a selected active metal oxide can be embedded as nano-particles in the support material. In case of chemical looping hydrogen production nano-sized iron particle were applied (figure 16). The carrier showed a high stability at temperatures up to 900 °C without any signs of deactivation. Redox reaction revealed similar reduction rates compared to conventional oxygen carrier supports, however, significantly accelerated oxidation rates were measured. The steam oxidation rates were further improved by decreasing the particle sizes from 54 nm to 16 nm.

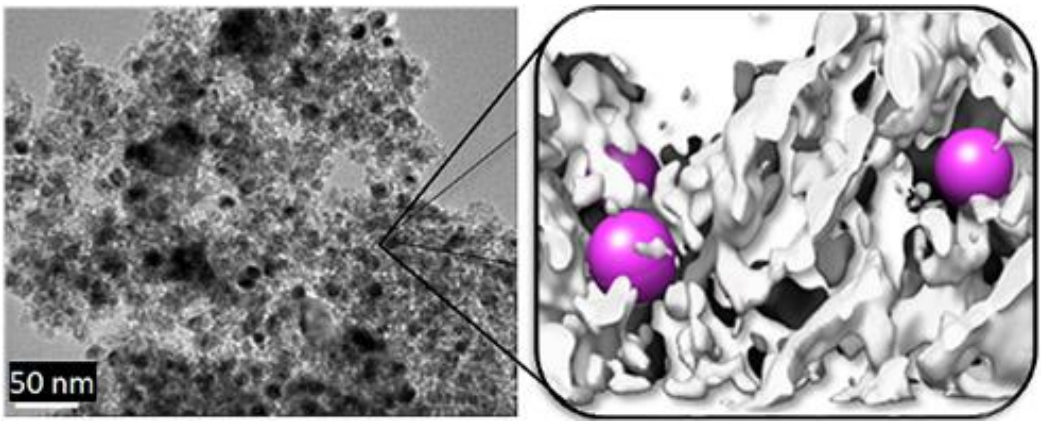

Figure 16: Left: TEM image of a Ni-BHA nanostructured carrier (Ni = 40 wt%). Right: 3D tomographic reconstruction of the carrier nanostructure from a set of TEM slices. The white structure represents the BHA carrier with the embedded metal nanoparticles shown as pink spheres.[134] §§§§§§§

2.3 Reactor Design

Two reactor designs, the fixed bed reactor and the fluidized or moving bed, were successfully operated and presented in the surveyed literature (summarized in table 8). The fixed bed reactor system is operated in batch mode by switching the operation gases. The oxygen carrier is kept in place, while the reduction and the oxidation reactions are executed consecutively. This enables a design with a low degree of complexity due to the absence of moving parts. High purity hydrogen is obtained because the carbon containing fuel streams and the hydrogen stream are completely separated. The fluidized or moving bed system circulates the oxygen carrier between separated reactors or reactor sections. The moving solid material increases the system complexity and mechanical strain, however, the higher technological complexity enables several beneficial properties. In contrast to a fixed bed reactor these systems are operated in continuous mode and thus enable an (i) uninterrupted hydrogen production combined with pure separated streams of CO_2 and N_2.[28,135,136] In each reactor the same reaction, either reduction or oxidation, is performed, which permits (ii) a specific reactor layout regarding materials, design and operation parameters to optimize gas yield and solid conversion.[137–140] (iii) The solid materials, which suffer from cycle stability can be continuously replaced during normal operation modes. (iv) The oxygen carrier can participate in the heat management of the system by delivering heat from the exothermic oxidations to the endothermic reduction and thus reduce the required amount of external heat.[135,141] However attrition losses due to movement of the solids and a lower hydrogen purity caused by the gas slip between the reactors are to be excepted.[136,142]

A 25 kW_{th} sub-pilot syngas for syngas chemical looping (SCL) was introduced by Ohio State University (figure 17, left).[48,112,143,144] Sridhar et al.[143] discussed the adaption of the system to a three-reactor iron based system for the co-generation of pure hydrogen and electricity. The fuel reactor and the steam reactor were operated in a co-current moving bed system and a fluidized bed air reactor, which acted as a riser. The reactors were separated by a system of two ball valves. The solid flow rate was controlled with a rotary disc feeder. Experiments were performed with syngas (CO/H_2 = 2/1, flow rate 15 $L \cdot min^{-1}$) at 900 °C and a solid flow of 150 $g \cdot min^{-1}$. First operations demonstrated that a hydrogen production with an average purity of 94.5% and in situ carbon capture is feasible in this system. Tong et al.[48] optimized operation parameters and investigated the redox performance of two iron based oxygen carriers with 2 mm and 4.5 mm diameters during a total operation of 300 hours. Both samples provided sufficient high cycle stability, whereas the smaller particles possessed a faster reaction rate, probably due to the higher surface area. Both samples performed similarly well regarding syngas conversion and hydrogen purity. The smaller particles had a lower fluidizing velocity and required less air in the rise to be transported. Hence, smaller oxygen carriers are expected to show better flow properties and a higher resistance to attrition. System improvements by reducing gas leakage between the reactors were achieved by replacing mechanical seals[143] with a non-mechanical valve consisting of a standpipe with injected nitrogen.[48] Furthermore, a gas preheater for the synthesis gas feed was installed to prevent carbon deposition at lower temperatures and a dual syngas injection was added to optimize to axial gas concentration

profile and increase the syngas conversion from 78.34% to 92.23%. A final hydrogen purity > 99% at steady conditions was obtained. The system was also operated using methane with a feed conversion of 99.99% while maintaining a high oxygen carrier conversion of 32.50%.[144] A reduced solid flow rate increased the reduction degree to 48.82%, however the CH_4 conversion dropped to 80.35%. The results suggested that a complete fuel conversion is predefined by a critical solid/gas flow ratio. Flow ratios that exceed this ratio result in a non-reacting zone in the top of the moving bed. The counter-current moving bed used in this system is expected to increase the oxygen carrier conversion by up 5 times compared to a co-current fluidized bed systems with 11%.[112,145] In an experimental investigation lasting 2 hours, an oxygen carrier conversion in the reducer reactor of 35.54%, related to the theoretical value of 39.6%, was achieved, while maintaining a syngas conversion of > 99%.[143] Based on previous results with a syngas feed, the 25 kW_{th} sub-pilot unit was utilized for the coal direct chemical looping process (CDCL) in continuous operation lasting 200 hours. A coal conversion ranging from 90 – 99% with an average conversion of 99.7% was obtained. These experiments were not combined with the steam oxidizer, hence no conclusion can be drawn on the possible hydrogen purity, however, combustor gas analysis for carbon sequestration indicated a CO_2 purity of 99.7% with CO 0.2% and CH_4 0.1% as the main impurities.[112]

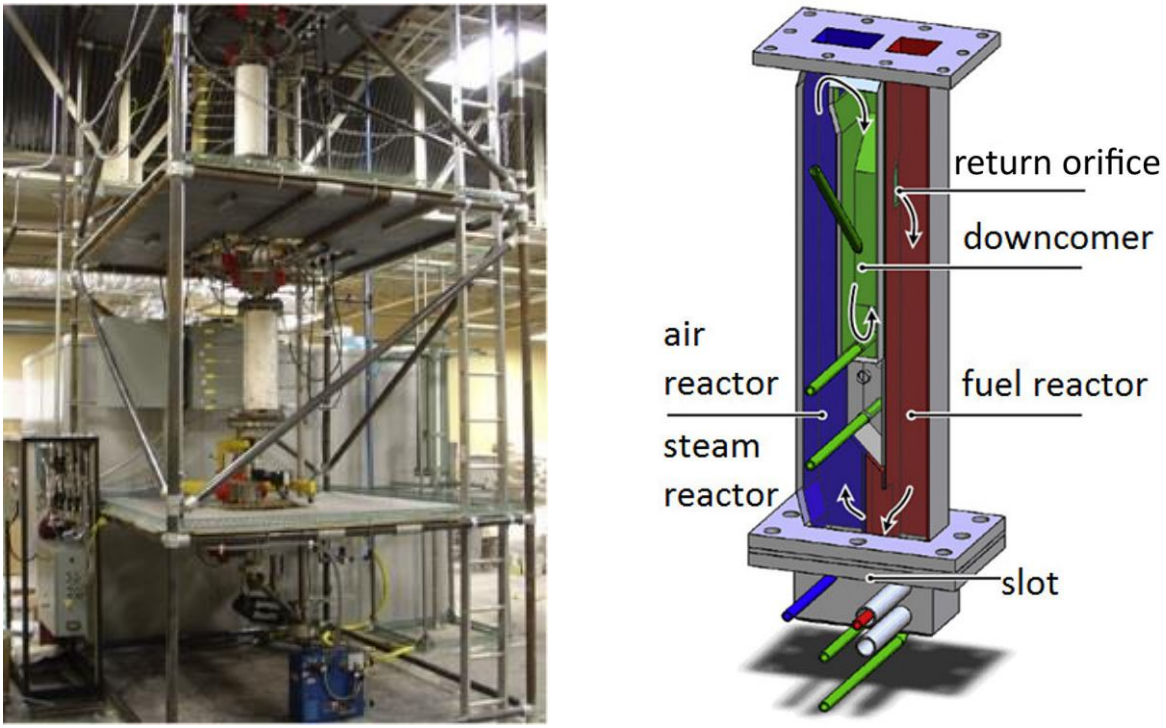

Figure 17: Left: photo of the 25 kW_{th} sub-pilot SCL unit at The Ohio State University.[112] £ Right: schematic representation of the two-compartment fluidized-bed reactor proposed by Rydén et al..[135] ££

Rydén et al.[135] examined a two-compartment fluidized bed reactor for hydrogen production at temperatures between 800 – 900 °C (figure 17, right). The system with 300 mm in height consisted of a steam reactor (25x25mm) which transported the oxygen carrier upwards to the down-comer, where the particles passed into a J-type loop-seal and were transferred to the fuel reactor through an orifice. The fuel reactor was operated as a bubbling bed. At the bottom, the oxygen carrier returned past a U-type slot to the steam reactor and closed the circle. Experiments were executed with syngas or CO as feed (0.5 – 1.25 $L \cdot min^{-1}$) and steam (4.0 – 5.0 $L \cdot min^{-1}$) as oxidant. An iron based oxygen carrier (60 wt% Fe_2O_3 and 40 wt% $MgAl_2O_4$) in the diameter range of 90 – 250 µm was applied. The operation started with a full conversion of the fuel due to the presence of Fe_2O_3. After the initial reduction to Fe_3O_4, CO an incomplete conversion was observed due to reduction stage of Fe_3O_4 to FeO. Particles reduced to FeO were transferred to the steam reactor. A stable operation without problems of de-fluidization was maintained for up to 4 hours with a gas conversion between 75 – 80%, which increased with a decreasing fuel flow. These results were slightly higher than expected by thermodynamic predictions, probably caused by gas leaking from the fuel reactor into the steam reactor. In the steam reactor the FeO particles were oxidizing with a hydrogen production rate of 0.5 $L \cdot min^{-1}$, which matched the theoretically value as long as the fuel gas flow was kept at low values. The impurities CO_2 19% and CO 5% were detected in the hydrogen as a results of gas leakage.

Moghtaderi[146,147] developed a miniaturized chemical looping steam reformer CLSR in micro-reactor assembly, which is suitable for on-board mobile fuel enrichment with hydrogen (figure 18, left). The miniaturized system is expected to show improvements compared to conventional designs with regard to (i) volumetric productivity, (ii) safety issues, (iii) operation costs, (iv) scalability, (v) pressure drop and (vi) surface-to-volume-ratio. The micro-reactor assembly used in the experiments consisted of a single stainless steel plate with a zigzag shaped engraving (0.05 m length, cross section area: 200x100 µm) (figure 18, right). Fe_3O_4 on alumina support with a layer thickness of 1 µm and a particle size of 20 – 40 µm was utilized as an oxygen carrier. Reduction experiments at 900 °C with methane resulted in a rapid reduction to FeO and the formation of solid carbon by catalytic decomposition of methane. The consecutive steam oxidations started with an initially fast oxidation rate, which decreased significantly at a solid conversion of 80%. The complete oxidation took approximately 4 times longer than the reduction. A series of 4 reactors was proposed, each consisting of one µ-CLSR unit as described before, to equalize the different reaction times and compensate for the longer oxidations. The proposed operation procedure consisted of consecutively executed reductions and simultaneously performed oxidations in the 4 reactors. The experimental results suggested that, within the timeframe of 48 seconds, a solid conversion degree of 30% in all participating µ-reactors was achieved followed by a complete re-oxidation yielding a hydrogen product stream with 96% purity. Thus, the layout of 2x4 reactors enables a continuous production of hydrogen in a µ-CLSR system.

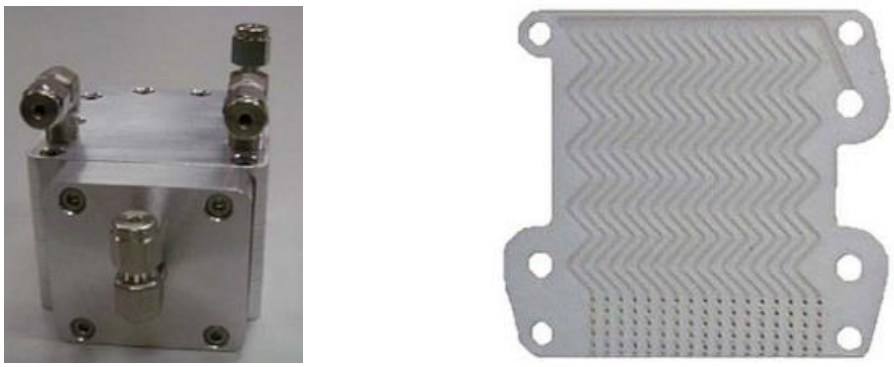

Figure 18: Left: the CLSR micro-reactor proposed by Moghtaderi. Right: a single reactor plate with the zigzag shaped pattern, which are used in the CLSR micro-reactor.[146] £££

Xue et al.[140] developed a three-reactor fluidized-bed system in the range of 50 kW. The system was constructed and operated as a cold-flow model. A fluidized fuel reactor was proposed as a key component, which consisted of a base bubbling bed at low velocity and an upper fluidized bed at high velocity (figure 19, left).[139,140,148] Fe_3O_4 particles entering near the bottom bubbling bed react with the fresh fuel gas and leave the reactor in reduced state at the bottom. The reduction of Fe_3O_4 takes significantly longer than the reduction of Fe_2O_3, thus a sufficiently large bubbling bed guarantees the required residence time in the bottom part to ensure a desired solid conversion. The partially reacted fuel gas moves through the upper reactor section, where Fe_2O_3 particles from the oxidizer are supplied. The Fe_2O_3 particles are partially reduced by completely converting the reduction gas to H_2O and CO_2. The fuel reactor design was successfully operated for 600 minutes using aqueous bio-oil.[139] Xue et al.[140] integrated the reactor into a 50 kW three-fluidized–bed reactor system to investigate operation parameters and solid circulation characteristics. The main design values were an operation temperature of 900 °C, methane as fuel, a particle size of 100 – 305 µm, a solid inventory of 5 kg and gas flows between 24 – 31 $Nm^3 \cdot h^{-1}$. Cold-flow operations were performed with He/air in all three reactors with glass beads as particles. By varying the gas flows and changing the fluidizing conditions, the solid circulation rate was manipulated. It was found that the solid circulation rate influenced the gas leaks between the reactors, which is of high importance regarding hydrogen purity and CO_2 emissions. The cold flow operations were performed in long-term operation tests with stable pressure conditions.

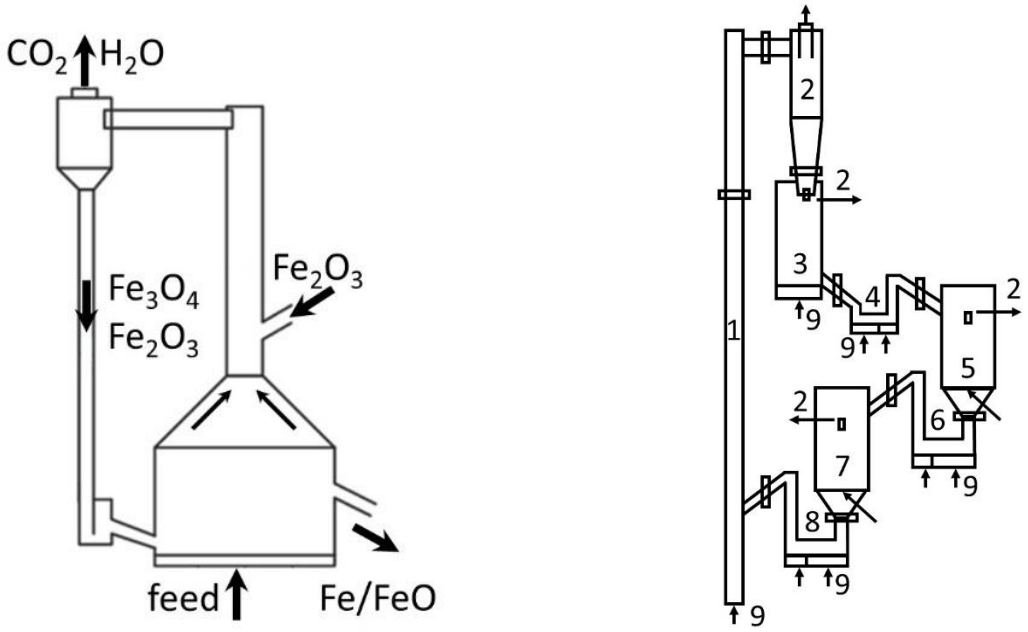

Figure 19: Left: schematic representation of the two-staged fluidized-bed system by Xue et al..[140] ffff. Right: schematic representation of the 300 W_{th} TRCL system operated by Cho et al..[28] 1 Riser, 2 cyclone, 3 air reactor (AR), 4 AR loop-seal, 5 fuel reactor (FR), 6 FR loop-seal, 7 steam reactor (SR), 8 SR loop-seal and 9 distributor. fffff

Cho et al.[28] constructed a 300 W_{th} three-reactor chemical looping system to produce high purity hydrogen out of methane (figure 19, right). Steady solid circulation operation, using Fe_2O_3 supported with ZrO_2 with a diameter of 125 – 300 µm, was executed for 13 hours.[89] The solids showed no agglomeration and only small signs of thermal sintering, which suggested a high durability. An average methane conversion of 94.15% at 900 °C was achieved. Fuel flow analysis indicated that a high methane conversion is possible as long as a moving bed regime is maintained. A transition to a fluidized bed reduced the methane conversion to below 90%. Hydrogen with a purity of 99.95% was produced at 800 °C with minor CO contaminations, when reducing the oxygen carrier to FeO. CH_4 was not detected, which suggested that gas leakage into the steam reactor was negligible. The H_2 production rate was approximately 63% below the theoretical value due to a non-uniform flow pattern. The formation of carbon was investigated under the deep reduction of the oxygen carrier by lowering the solid flow. The higher amount of completely reduced iron catalyzed the deposition of solid carbon. A higher amount of produced hydrogen with a significantly reduced purity was observed, as a result of the oxidation of carbon with steam.

Hong et al.[149] studied the solid flow characteristics of zirconia beads (mean diameter 186 µm) in a multi stage moving bed system. The gas flows into the loops seals were varied to investigate the changes in the flow pattern, the solid mass flux and the solid mean residence time at ambient temperatures. In the moving bed regime the solid mass flux and the pressure drop increased with a rising gas flow in the loop seal. A stable pressure profile was maintained. The higher gas flow correlated with a growing bed height but lowered the mean residence

time of the solid particles because of an enlarged solid mass flux. A further increase of the gas flow changed the flow pattern to a bubbling flow, and finally to a slug flow characteristic. The flow patterns had little effect on the solid mass flux but resulted in significant pressure deviations. As long as a moving bed regime was maintained the solid flux pattern remained similar at different temperatures, however higher gas velocities and a higher solid flow rate were measured. Lee et al.[150] concluded that a riser is required as a 4th module to increase the stability of the system. The selected operation conditions of gas velocities and solid circulation rate enabled a stable pressure profile and prevented gas leakage between the reactors.

Herguido et al.[142] introduced a single reactor with two interconnected beds, a slow reduction bed with H_2/CH_4, and a second fast bed for steam oxidation (figure 20, left). Oxygen carrier with particle size of 150 – 200 µm mixed with silica sand were applied. The two beds are connected with two slits at the bottom and the top. Redox experiments were performed at 550 °C. Three designs of interconnections between the two beds in respect to gas leakage were evaluated, a rectangular slit, a J-connection and an orifice connection (figure 20, right). The orifice connection with a hole-diameter of 0.3 cm and an open area of 0.4 cm² showed a more superior performance than the other design variations. The gas leakage was successfully minimized by reducing the gas velocity difference in the two fluidized beds.

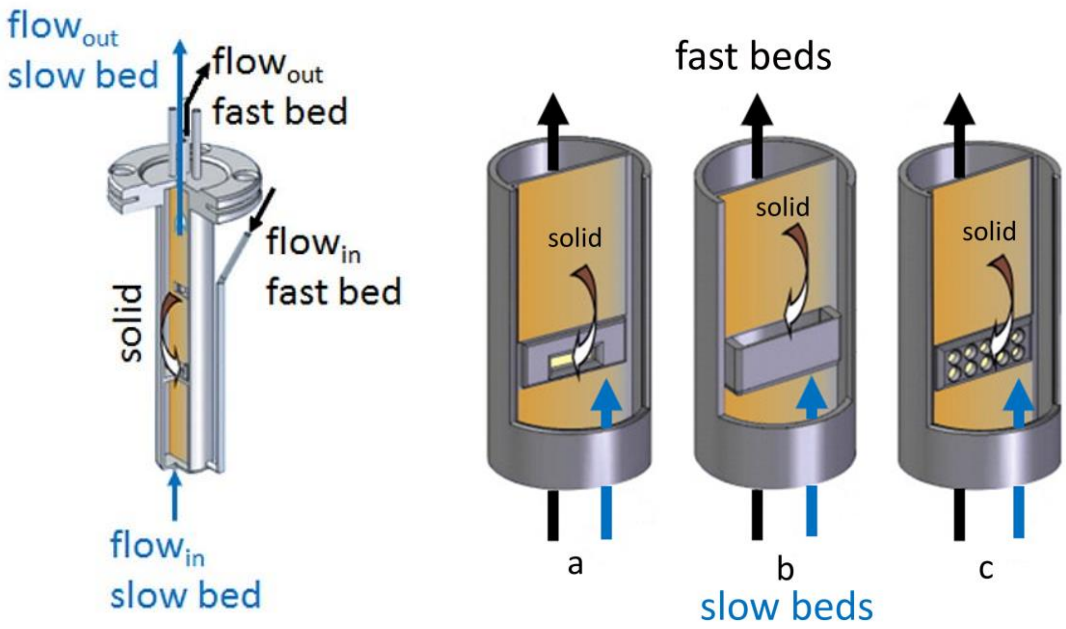

Figure 20: Left: schematic representation of the fluidized-bed system by Herguido et al.. Right: schematic of different connecting devices rectangular connection (a), J-connection (b) and orifice connection (c).[142] £££££

2.4 Process Development

Chemical looping technologies for hydrogen generation are usually operated with a reducing synthesis gas provided by external processes, e.g. from coal gasification or methane reforming. However, recent work has shown that the process can be easily modified to handle a variety of feedstocks, including unconventional resources, either by direct reduction or by the incorporation of the chemical looping system with syngas conversion processes. Herguido et al.[142] investigated the applicability of the chemical looping process for the separation of a mixture of hydrogen and methane. A reactor with two interconnected fluidized beds and an iron based oxygen carrier were used for the fuel processing. Reactions were executed in a temperature range of 500 – 550 °C and with hydrogen fractions between 0.35 – 0.65. The operation conditions enabled a reduction of iron oxide with hydrogen but left methane and other impurities inert. An average hydrogen conversion of 20% was obtained with little influence of the varied parameters (gas velocity, relative velocity and hydrogen content), which suggested that the separation performance is mainly limited by thermodynamic restrictions. The separations system was tested for 44 h and enabled the production of pure hydrogen without carbon contaminations. Small amounts of solid carbon were found in the reactor after the operation, thus coke remained inert during the experiments at the selected oxidation conditions.

2.4.1 Alcohols as feedstock

The same group investigated ethanol[151] and methanol[152] as feed in a fixed bed reactor. Fe_2O_3 supported with CeO_2 and Al_2O_3 was used as the oxygen carrier. Higher temperatures and a higher ethanol partial pressure (0.05 – 0.15 bar) accelerated the reduction rates. However, an increased reduction temperature led to a slower re-oxidation rate in the consecutive steam oxidation, most likely caused by thermal sintering of the particles. The reductions of the alcohol feeds revealed 3 stages: (i) the reduction of Fe_2O_3, (ii) the reduction of Fe_3O_4 to Fe and (iii) a stable thermal decomposition of ethanol and methanol. A higher reduction degree of the solid led to a higher amount of partially oxidized components (CO and H_2) and a lesser amount of fully oxidized components (H_2O and CO_2). The gas composition converged towards the theoretical values of thermal decomposition products after the full reduction of the oxygen carrier. Solid carbon formation occurred in all three stages and was verified by the detection of structured nanotubes after the experiments. The formation of iron carbide, which decomposed to iron and solid carbon, was promoted at 450 °C after the reduction to metallic iron. A process with short-time looping steps may avoid the carbide formation and thus limit the amount of solid carbon to minimize the carbon contaminations.[153] The methanol reduction showed a significantly higher carbon deficit in the carbon balance, which correlated with higher amounts of coke at lower temperatures.[152] The consecutive oxidations with steam at 500 °C produced hydrogen with little CO and CO_2 contaminations (below 1 ppm) in the case of ethanol as feed and no carbon impurities using methanol (50 ppm detection limit). Hence, coke remained mostly inert on the solid particles. Several consecutive cycles suggested that the advisable reaction temperature for ethanol and methanol is 675 °C and 700 °C

respectively. At these temperatures the smallest decay of the oxygen carrier, while providing a sufficient fast reduction rate, was observed. Coke formation occurred over to complete temperature range with both feeds, which demands a decoking step after several cycles to prevent carbon accumulation.[151–153] TPR reduction analysis of three iron oxides, hematite, goethite and magnetite using low concentrations of ethanol in nitrogen was performed by Rosmaninho et al.[154] All samples revealed the reduction intermediates Fe_3O_4 and FeO before the complete reaction to Fe, irrespective of the initial oxidation state. In all cases the ethanol conversion started at a temperature of 300 °C. The complete conversion of ethanol was reached according to the accessibility of surface oxygen. Hence, hematite and goethite enabled a complete ethanol transformation between 350 – 400 °C, whereas the application of magnetite required a temperature beyond 500 °C to achieve a complete conversion. At 700 °C, a complete reduction of the oxygen carrier to iron was observed. A further temperature increase led to a significant formation of solid carbon and iron carbide, thus 700 °C was identified as the most suitable reaction temperature to achieve a complete reduction and to minimize the deposition of carbon. The oxidation with steam re-oxidized the oxygen carrier to magnetite with small amounts of hematite and wustite. Consecutive redox cycles revealed a degradation of the oxygen carrier, which led to an incomplete reduction and a reduced amount of produced hydrogen of 70% after 5 cycles.

2.4.2 Process combination of reforming of hydrocarbons with CLWS

Plou et al. and Herrer at al. combined the catalytic dry reforming with the chemical looping hydrogen in a single reactor bed.[155–157] As a solid mixture a triple oxide oxygen carrier (Fe_2O_3 supported with CeO_2 and Al_2O_3) and a nickel based catalyst ($NiO/NiAl_2O_4$ with an excess of NiO of 10 wt%) was applied with a weight ratio of OC/catalyst of 85/15 wt%. Experiments were performed with different biogas compositions CH_4/CO_2 50/50 – 65/35 at temperatures from 600 – 750 °C. Three stages were visible in the fixed bed reductions, which were analyzed in detail. The reaction started with a high methane conversion directly followed by a conversion minimum. This phase was initially dominated by the reduction of Fe_2O_3 to Fe_3O_4 and the full oxidation of the feed to CO_2 and H_2O. After the consumption of the lattice oxygen of Fe_2O_3 the reduction of NiO to Ni occurred, which was indicated by the appearance of H_2 and CO. The presence of elemental Ni enabled the catalytic dry reforming of methane to produce a stable fraction of CO and H_2 in combination with the deep reduction of Fe_3O_4 to iron. Once the oxygen carrier was completely reduced, the solely catalytic dry reforming of biogas was observed. An increasing reaction temperature enhanced the reaction rates and the transition to the stable reforming stage, whereas an increased CH_4 ratio slightly accelerated the transition between the stages. The comparison of experimental data with theoretical data showed good accordance for the dry reforming but a constant deviation regarding the iron oxide reduction reaction, which suggests diffusion limitations hindering the mass transfer. The formation of coke by CH_4 decomposition indicated by a too high amount of measured hydrogen and thus the deactivation of the catalysts by blocking of active catalytic sites was observed. The effect was enhanced with increasing CH_4 fractions. Post reaction analysis

reported the presence of graphitic carbon[155,157] and highly amorphous carbon.[156] Coke was only present on the nickel particles, which explained the catalytic degradation. During purging phases with inert gas a mass loss was observed, which increased with higher temperatures. This suggested a solid-solid decoking reaction between the incompletely reduced oxygen carriers and the solid carbon and explained the absence of coke on the oxygen carrier in the post experimental analysis. The oxidations with steam at 500 °C produced hydrogen with a purity of > 99% with carbon dioxide as impurity. The main part of the carbon depositions remained inert during the steam oxidation, and thus accumulates over consecutive cycles without a regeneration step.[54,152,156,157] A combination of a catalytic steam reforming and the chemical looping hydrogen process in one reactor with two adjacent fixed bed was investigated by Nestl et al.[55] Investigations of methane reforming were executed, varying temperature, pressure and the S/C-ratio, emphasizing a high conversion of CH_4, the avoidance of carbon depositions and a reformate-gases with a sufficient reduction potential. The results suggested that high CH_4 conversion of > 99% is possible, however higher system pressures require a significantly greater S/C ratios, and thus yield synthesis gas with increased water content and a lower reduction potential. It was concluded that the reforming in combination with the reduction step of an iron based oxygen carrier should be performed at ambient pressure. The oxidations with steam were executed at elevated pressure up to 8 – 11 bar to produce hydrogen with a purity > 99%. Small amounts of CO_2 were detected, which implied the formation of solid carbon during the reduction, although not predicted by the simulations.

2.4.3 Pressurized oxidations

Voitic et al.[54,158] analyzed the correlations between the increased oxidation pressure and the cycle stability, the conversion efficiency and the structural integrity of an iron based oxygen carrier. Steam oxidations were performed at 750 °C and at different pressure steps up to 55 bar. The results revealed no repercussion of an increased system pressure on the oxygen carrier conversion and on the oxidation rate. A high purity hydrogen was obtained by pressurized steam oxidation in the range of 99.95 – 99.999% with CO and CO_2 as impurities. The amount of carbon impurities was not influenced by the increased system pressure, however a correlation with the length of the reduction reaction was observed. The mass balances indicated an incomplete oxidation of solid carbon by steam. This resulted in an accumulation of solid carbon and a gradually decrease of hydrogen purity. Hence, an air regeneration step had to be included to completely remove carbon contaminations and to regenerate the oxygen carrier.[54,151,152] A linear decay of the oxygen carrier stability was visible which was related to thermal sintering of iron by deep reduction. A porous structure was maintained in the particles despite the pressure load, which demonstrates the applicability of the chemical looping water splitting process in a fixed bed configuration for high pressure hydrogen production with a hydrocarbon feedstock.

2.4.4 Heavy fraction bio-oil as feedstock

Zeng et al.[139,148] and Xiao et al.[111] investigated the reduction behavior of a bio-oil heavy fraction from a cotton stalks pyrolysis unit with a water content of 18.54 wt%. Ilmenite was selected as the proper oxygen carrier in a fixed bed redox reaction for its resistance to carbon depositions and reducibility at temperatures > 950 °C. Preliminary experiments yielded a carbon conversion in the range of 57% – 82%, which was enhanced by an increasing temperature with an optimum at 950 °C. Beyond 950 °C a declining carbon conversion was measured, which was related to an increased methane crack reaction and the formation of solid carbon. In several consecutive cycles, the ilmenite sample achieved a stable hydrogen yield of 93 – 96 $Nm^3 \cdot kg^{-1}$ within the first 10 cycles. However, after 10 cycles, sever sintering, which led to a lower active surface and average pore diameter, and a drop in released hydrogen was observed. Significant amounts of carbonaceous contaminations were detected with a hydrogen purity below 85%. The gasification of solid carbon with steam was identified as the source of contaminates. The heavy fraction of the used bio-oil contained a high amount of phenolic compounds, thus increasing the tendency towards carbon deposits. In order to improve the hydrogen purity steam was added during the reduction process. A steam/oil ratio of 2.0 improved the carbon conversion of the fuel to > 99% and enhanced the hydrogen purity to > 99%. However higher amounts of steam decreased the oxygen carrier reduction degree, thus lowering the amount of produced hydrogen.

2.4.5 Hydrothermal hydrogen generation

Hydrothermal hydrogen generation by the oxidation of iron enables the operation at very mild temperatures in the range of 100 – 200 °C. This reduces the complexity of the oxidation process significantly compared to conventional chemical looping water splitting, which usually requires temperatures > 600 °C. Feasibly studies were performed by Tsai et al.[159] in an autoclave by measuring the pressure profile and gas phase at different reactor temperatures. Reference tests were performed with solely water as reactor filling. The supplement of iron powder led to a constant pressure increase, which was further raised by the amount of iron, the reactor temperature and smaller particle sizes.[159,160] After oxidizing the iron powder the pressure remained at a constant level. The gas phase consisted of pure hydrogen with a low water content of 0.525% at 120 °C. Michiels et al.[160] further enhanced the hydrothermal process by using a 1 molar potassium hydroxide solution. The system was put under CO_2 pressure, which dissolved in the aqueous solution and formed potassium carbonate in the presence of potassium hydroxide. The reactor was heated to temperatures up to 200 °C. Iron in the presence of carbonate was oxidized with water to magnetite, H_2 and CO_2 within a reaction time of 16 h. After cooling down, hydrogen was measured in the gas phase with a purity of > 99 mol%. Experiments focusing on the role of compressed CO_2 in the system revealed that the dissolved carbon dioxide was critical for the process by forming carbonate ions to promote the oxidation of iron to hematite. The absence or deficit of CO_2 resulted in a reduced amount of produced hydrogen. An excess of CO_2 caused the formation of siderite instead of magnetite, thus a lower amount of hydrogen with significant CO_2 contaminations

was detected. The presence of potassium hydroxide was vital in the system to promote the solubility of CO_2 and the formation of CO_3^{2-}-ions. The absence of potassium carbonate resulted in a lower amount of hydrogen. The system did not suffer from a net-carbonate-ions loss within one complete cycle. Hence, the aqueous solution can be reused in the sequential cycle by adding the amount of consumed water.

2.5 Process Simulations

The main research focus in the field of chemical looping hydrogen technology is currently on three-reactor systems. These systems are very flexible in terms of the fuel input, while maintaining a superior total efficiency compared to conventional hydrogen production processes. Additionally they offer the possibility of a high carbon capture rate with low energy penalties, which makes chemical looping hydrogen systems promising for renewable and fossil feedstocks alike. Particularly emphasizing renewable sources, different feedstocks were considered and analyzed with regard to their hydrogen production capabilities and system efficiencies. The systems were optimized with the defined specifications of (i) a high solid conversion, (ii) low concentrations of H_2 and CO in the fuel reactor outlet, (iii) no coking, (iv) minimized wt% of support material, (v) minimized external heat input, (vi) low solid flow rates and (vii) a maximized product gas yield.[145]

2.5.1 Three-reactor chemical looping systems

Cormos et al.[161–164] evaluated a three-reactor chemical looping system for the co-generation of hydrogen and power using direct coal gasification. Two cases were considered, which differed in their heat integration strategy. Case 1 supplied the required heat in the fuel reactor by the oxidation to Fe_2O_3 in the air reactor and case 2 supplied oxygen with an air separation unit (ASU) to the fuel reactor for the partial oxidation of the coal feed. The reduction in the fuel reactor was conducted between Fe_2O_3/FeO at 38 bar and 650 – 900 °C and produced a pure CO_2 stream for carbon capturing. Hydrogen released in the steam reactor was consumed in a gas turbine for power generation or compressed to 60 bar for a hydrogen infrastructure. Results focusing solely on power generation yielded a net electrical efficiency in the range of 41% – 42% for both cases with a carbon capture rate of > 99%. The two benchmark systems, a conventional IGCC with Selexol pre-combustion capture and an IGCC with an upstream shell gasifier and a downstream TRCL system yielded a slightly lower efficiency of 37.11% and 38.38% respectively. The IGCC chemical looping system enabled a carbon capture rate > 99% whereas the conventional coal gasification facilitated a carbon capture rate of roughly 91%. The net efficiency of case 1 was further improved to 49.88% by increasing the hydrogen output to approximately 50% of the overall power output. Mukherjee et al.[165] analyzed a coal gasification power plant in the range of 400 MW using three-reactor chemical looping for electricity and hydrogen generation. In the operation focusing on gas yields, with a hydrogen power output share of 78%, a total plant efficiency of 59.4% and an exergy efficiency of 53.0% was possible, while maintaining a CO_2 capturing efficiency of 99%. Two benchmarks systems based on IGCC with PSA or Selexol for carbon capturing yielded similar energy and exergy efficiencies, however at the cost of lower CO_2 capturing efficiencies of 89.9% and 93.5% respectively. Similar advantages were reported when comparing the iron-based looping systems to calcium-based looping systems. Two calcium based systems with either a pre- or a post-combustion design inhered lower net efficiencies of 4% – 6% points with a carbon capture rate of approximately 96%.[164]

Sorgenfrei et al.[138] analyzed an IGCC-chemical looping hydrogen system using either a shell gasifier or a British Gas/Lurgi (BGL) oxygen-blown moving-bed gasifier. Bituminous coal was selected as feed and iron oxide served as the oxygen carrier. Both systems outperformed conventional IGGC systems in terms of net efficiency in the range of 38.1% – 41.4% and in terms of carbon capturing efficiency. The comparison of the two chemical looping systems indicated an advantage of the BGL gasifier over the shell gasifier regarding efficiency and design simplicity. The BGL systems required less oxygen for the gasification, thus consuming less power in the air separation unit (ASU). However, the chemical looping cycle in the BGL systems required an increased solid flow to convert the synthesis gas completely, and therefore a higher airflow to oxidize the oxygen carrier. The air reactor temperature was identified as a critical parameter for efficiency optimization. An increase of the temperature from 800 to 1000 °C resulted in a reduced solid mass flow and a decreased power consumption, thus raising the efficiency by 4.6% points. The addition of a CO_2 turbine reduced the total system efficiency despite the 60% surplus generation of electrical energy because of its repercussions on the heat recovery in the steam cycle.

Yang et al.[166] integrated a three-reactor system into a Fushun-type oil shale retorting process (OSR-CLH) (figure 21, left). In conventional oil shale plants, a retorting gas with a low heating value is produced and converted to electricity via an internal combustion engine. The chemical looping process instead utilizes this retorting gas for hydrogen production. The process heat provided by the off-gas from the three reactors was used for power generation. The oil-retorting reactor was operated at 520 °C to maximize the hydrogen and shale oil yield. The Fe_2O_3 solid flow rate was adjusted to enable a complete conversion of the retorting gas to H_2O and CO_2 and the steam flow was regulated to fully re-oxidize the iron based oxygen carrier. An exergy comparison and techno-economic analysis was performed between the conventional plant and the OSR-CLH system in a realistic production scale of 375 $t \cdot h^{-1}$ oil shale. The conventional plant suffered from a larger exergy destruction within the combustion engine, meaning that the OSR-CLH system had a higher total plant efficiency of 7.3% points. However, the economic analysis indicated higher capital costs and higher production costs for the chemical looping system of approximately 23% caused by the additional system units and by the oxygen carrier as second material.

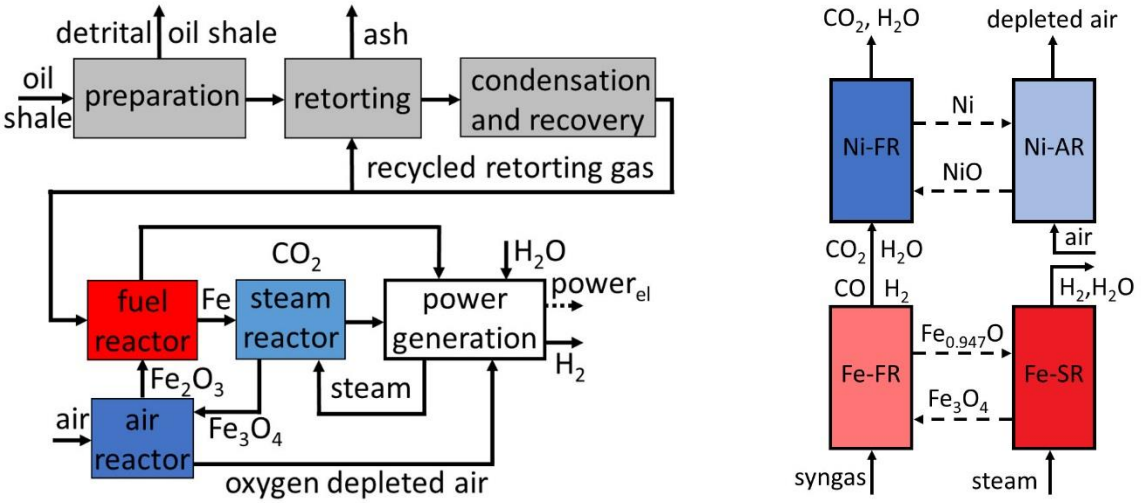

Figure 21: Left: process diagram of the combination of an oil shale retorting process with a chemical looping hydrogen process by Yang et al..[166] ∏ Right: process schema of the combination of an iron based chemical looping hydrogen process with a nickel based chemical looping combustion process by Cheng et al..[167] ∏∏

Zeng at al.[168] simulated a direct coal three-reactor chemical looping plant solely for hydrogen generation using iron oxide. The fuel reactor temperature was operated at 900 °C with a solid conversion of 56.3%. Two pressure conditions 30 atm and 2 atm with a Fe_2O_3/coal flow rate ratio of 1.38 enabled a complete coal conversion. A pressure increase beyond 30 atm reduced the coal conversion efficiency. In the steam reactor, a temperature of 700 °C and a steam/Fe ratio of 1.9 ensured a complete oxidation to magnetite while optimizing the steam conversion irrespective of the selected system pressure. The two operation conditions, pressurized and atmospheric, yielded total efficiencies of 79.69% and 71.36% respectively with carbon capture rates of 99%. The operation at atmospheric pressure had a lower efficiency, however, the absence of gas compressors and expanders significantly lowered the plant investment cost and its complexity. A third case, which considered kinetic limitations with a lower carbon conversion of 95% yielded a total efficiency of 77.24%. The lower coal conversion led to carbon impurities in the produced hydrogen. Hence, a higher purification effort and a larger amount of tail-gas had to be taken into account. The formation of pollutants, which originated from the coal feed were considered. Chlorine was converted to HCl, whereas mercury stayed in elemental form in the fuel reactor. Both pollutants exited the system with the CO_2 stream. Sulphur formed $Fe_{0.877}S$ in the reducer and was mainly carried over to the steam and air reactor where it was re-oxidized, resulting in both H_2S and SO_2 being present in the system.

Chen et al.[141] simulated the integration of a three-reactor chemical looping hydrogen system with a SOFC/gas turbine system for power generation. A shell gasifier was selected to convert bituminous coal to a synthesis gas. The reduction gas was utilized to convert an iron based oxygen carrier to wustite at 950 °C in the fuel reactor. Pure hydrogen was generated in the steam reactor at 750 – 800 °C and supplied to a SOFC. The SOFC anode off gas, which contained 10 – 25% of hydrogen, was burned in a gas turbine. Heat recovery steam generator

systems were installed downstream after the fuel reactor and the gas turbine. The combination of a CLH system with a SOFC and the utilization of pure hydrogen was expected to show advantages regarding (i) better electrochemical kinetics, (ii) the complete prevention of solid carbon formation, (iii) a better heat distribution by avoiding endothermic reforming reactions and (iv) the complete sequestration of carbon from the fuel. The plant analysis yielded an electrical efficiency of 43.53% with complete CO_2 sequestration. A higher system pressure was found to be beneficial for raising the total efficiency, while increasing reaction temperatures in the chemical looping plant had only limited effects on the overall plant efficiency. The variation of the steam reactor temperature raised the power output of the gas turbine but lowered the power output of the steam turbine, hence the two effects annulled each other. The analysis of the three-reactor chemical looping hydrogen system combined with a SOFC by Ozcan et al.[169] yielded a total energy efficiency of 45.39% for full power conversion and 56.92% for combined power/hydrogen production (ratio of 1.5/1). The two cases resulted in total exergy efficiencies of 34.98% and 45.05% respectively. The three-reactor chemical looping components alone contained an energy and exergy efficiency of 65.37% and 57.9% respectively. The highest amount of exergy destruction occurred in these elements due to the high process heat and the low hydrogen yield. Operating conditions required to maintain a complete conversion of syngas and the full re-oxidation of Fe/FeO to Fe_3O_4 were determined. Hence, the ratio of steam to feed played a substantial role in terms of efficiency. Another important parameter was the ratio of utilized/stored hydrogen. The system efficiency was raised by roughly 10% points by increasing the amount of deliverable hydrogen to 40% of the total power output at the cost of electric efficiency.[164,168,169]

2.5.2 Two-reactor chemical looping systems

Chen at al.[167] combined an iron oxide based two-reactor cyclic water-splitting system with a nickel oxide based chemical looping combustion unit (figure 21, right). Syngas, produced by coal gasification in a shell gasifier, was used as a feed. The oxygen carrier was cycled between magnetite and wustite, thus syngas was not fully converted in the Fe fuel reactor. This lean gas reduced the nickel oxide in a second fuel reactor. The Ni-looping cycle was closed by oxidation with air. A pure hydrogen stream was generated in the iron cycle, while the nickel cycle yielded a pure carbon dioxide stream. Both streams were expanded separately for power generation and heat recovery. Two cases were investigated, the first using a supplementary firing unit to increase the turbine inlet temperature of the oxygen deplete air gas stream. Hence, carbon emissions were produced with a carbon capture efficiency of 69.54%. The second cases omitted the supplementary firing unit and enabled a complete carbon sequestration. The total equivalent efficiency for both cases were 70.75% and 57.9% respectively. Operation parameters were varied to optimize the electrical power efficiency and the hydrogen yield for co-generation. A flexible production ratio of hydrogen and electricity was achieved by varying the iron oxide solid flow rate. The hydrogen production efficiency was optimized by raising the steam flow and the temperatures in the steam reactor and air-reactor. The addition of an inert support to the nickel oxide improved the heat

integration in the system and the hydrogen efficiency. Generally, a trade-off between hydrogen production efficiency and total efficiency was visible, hence a raised hydrogen yield was accompanied by a reduction in power efficiency. Both efficiencies were elevated with higher iron fuel reactor temperatures but at the cost of dropping carbon capture rates.

2.5.3 Evaluation of operation parameter

Kathe et al.[145] analyzed CH_4 as fuel in a three-reactor chemical looping hydrogen system using an iron oxide as oxygen carrier supported by Al_2O_3. Sensitivity analyses were executed to maximize the hydrogen production efficiency. Initial thermodynamic simulations explained the benefits of a counter-current moving bed of reactants and solid material compared to a co-current fluidized system. This operation mode reached the thermodynamic constraints of redox cycling more efficiently, thus lowering the required steam/solid ratio to reach a defined solid conversion. Additionally, a higher fuel/solid ratio was possible, while maintaining a complete fuel conversion. An increase of support material increased the reactor outlet temperature and the solid conversion at a fixed solid/CH_4 ratio, which enabled a full conversion of methane without the risk of coking. A value of 50 wt% Al_2O_3 was found to be optimum. The sensitivity analysis of Kang et al.[170] based on a linear empirical kinetic model suggested a content of 20 wt% of Fe_2O_3 on ZrO_2 as suitable content. The reaction temperatures in the steam and fuel reactor reactors were key to minimize the bed material input. In both reactors, an increase in the temperature reduced the required solid inventory to an optimum temperature value. Beyond the optimum, a contrary behavior was observed in the steam reactor, which was related to the exothermic nature of the reaction and the unfavorable equilibrium. Khan et al.[171] reported an increasing CO_2 and H_2 yield by raising the flow rates of steam, fuel and air until the stoichiometric values were reached. A Fe-oxygen carrier with 70 wt% $MgAl_2O_4$ as support yielded the highest amounts of product gases, whereas higher values reduced the gas output. Higher solid mass flow rates enabled an enhanced H_2 and CO_2 yield until an optimum. Kathe et al.[145] analyzed the steam conversion and outlet temperature, based on the oxygen carrier composition by adjusting the steam/solid ratio, steam conversion and outlet temperature. A re-oxidation to 11% of solid conversion yielded the highest amount of heat released at a high steam conversion efficiency. To complete the looping cycle, re-oxidation with air and a split of the solid flow was used, which bypasses the steam reactor and is directly transferred to the air reactor. The operation parameter air flow/fuel and split ratio of solid to oxidizer/bypassing-oxidizer were specified to facilitate auto-thermal operation conditions. The final plant layout for the simulation used a solid stream split of 0.15, which bypassed the steam reactor and was directly fed into the air reactor. In addition, 9% of the natural gas feed was directly injected into the air reactor in order to deliver the required heat duty. Hence, the process enabled a carbon capture rate of only 90%. A hydrogen production rate of 25711 $kg \cdot h^{-1}$, while utilizing 6196 $kg \cdot h^{-1}$ natural gas and a solid conversion of 60%, was calculated and utilized in several case studies. The highest system efficiencies were obtained by performing the process at a system pressure of 10 atm and exploiting a comprehensive energy recovery, which included gas expanders and a heat

recovery steam generation system (HRSG). A cold gas efficiency of 77.6% and a thermal efficiency of 75.1% was obtained compared to 72.1% and 69.7% of the reference case (a conventional SMR system). The chemical lopping system required 8% less natural gas and had a lower cooling demand and water requirement than the SMR case. Sanfilippo et al.[137] reported that an increase in the solid circulation rate required an external electric power input, but could further enhance the hydrogen production capacity and increase the total efficiency. The simulation results indicated a total system efficiency in the range of 78 – 79%, while maintaining a full carbon capture rate. The system variation can alter the process design and capabilities significantly. For instance, an increase in thermal efficiency was obtained by reducing carbon capture capabilities, while omitting the heat recovery units and lowering the operation pressure reduced the system complexity and the capital system costs at the expense of a lower thermal efficiency.[164]

Zhang et al.[172,173] performed thermodynamic and exergetic analyses on a two-reactor chemical looping hydrogen system and different oxygen carriers using methane as feed. The hydrogen produced in the steam reactor was burned with pure oxygen from an air separation unit. The generated steam was used for power generation in a steam turbine. The residual heat after the turbine is re-fed to supply the endothermic reaction in the fuel reactor. In a second system, the power generation unit consisted of a high-pressure and a low-pressure steam turbine. The single turbine and double turbine systems yielded a thermal efficiency of 55.5% and 59.8% respectively, which were 0.9% and 5.2% points higher than conventional combined cycles. The authors assumed a carbon capturing without any additional energy penalties by generation of a stream of CO_2 and H_2O and by the reduction between Fe_3O_4 and FeO in the fuel reactor. Hence, the efficiency was further raised by 7 – 9% points. The work does not discuss how the pure outlet stream in the fuel reactor is produced by the reduction of magnetite with CH_4. The two reactor chemical looping system was integrated into a coal based methanol production system.[174] Heat from the coal gasification, which supplied syngas for the methanol synthesis, was used in the chemical looping system for hydrogen supply. The reduction in the looping fuel reactor was performed with natural gas. The exergy analysis indicated that utilizing the coal gasification heat reduced the exergy destruction compared to the conventional operation of combusting parts of the natural gas. Metals suitable for use as oxygen carrier such as Ni, Zn and Fe enable a steam oxidation at low equilibrium temperatures and thus assist in the conversion of chemical energy with very high second law efficiency. Energy savings are made possible by minimizing the exergy destruction and the lowered consumption of natural gas.[166,173,174]

2.5.4 Unconventional feedstocks

Cormos et al.[175] investigated the replacement of coal with biomass (sawdust) as feedstock. The external gasifier still required a high amount of coal (70%) in the feed because the commercial availability of industrial scale gasifier solely for biomass is limited. The iron based chemical looping systems achieved the highest electric efficiency and a carbon capture rate

> 99% with the lowest carbon capture energy penalty. The reference systems based on gas liquid absorption achieved an energy efficiency 5.7% points lower than the chemical looping plant. Yan et al.[176] added a SOFC unit to the biomass-fed three-reactor chemical looping hydrogen system using coal and wheat straw. Post combustion of the anode off-gas, a steam turbine for power generation and CO_2 sequestration were considered. The amount of hydrogen and the total thermal efficiency were raised by increasing the gasification temperature, which improved the carbon conversions efficiency. Upon reaching a complete biomass conversion no further positive temperature effects were visible. The same behavior was found regarding the S/C ratio in the gasification unit. Below the ratio for a complete biomass conversion an increased amount of steam indicated positive effects on the plant performance, while an excess of steam lowered the total efficiency. The increased oxygen carrier circulation rate raised the amount of produced hydrogen per mass biomass. However, upon reaching the point of full oxidation of CO to CO_2, only hydrogen was consumed for the reduction reaction in the fuel reactor, which lowered the plant performance. The system evaluation yielded a total energy efficiency of 39.9% and total exergy efficiency of 37.6 % with a carbon capture rate of 96%. The comparison of a three-reactor system and a two-reactor system using the same feed gas conveyed the main difference in the behavior of the fuel reactor temperature.[177] Higher temperatures in a three-reactor system increased both the total thermal efficiency as well as the amount of hydrogen per mass feed. The endothermic reduction reaction was thermodynamically promoted at higher temperatures and enabled a greater reduction degree of the oxygen carrier. In the two-reactor system the lack of an air oxidation to meet the required heat supply had to be substituted by combustion of biomass. Thus the thermal efficiency and the amount of hydrogen per mass feed decreased. Both systems enabled a carbon capture rate of > 95%. The two-reactor system had a higher cold gas efficiency of 60% compared to 54% and a higher hydrogen production capability of 0.76 $Nm^3 \cdot kg^{-1}$ compared to 0.66 $Nm^3 \cdot kg^{-1}$. A calcium based sorption enhanced looping system used as reference had a higher cold gas efficiency of 72% with 0.73 $Nm^3 \cdot kg^{-1}$ of hydrogen but a lower carbon capture efficiency of 92%.

The application of bioethanol (12% ethanol and 88% water) from fermentation processes was examined by Cormos.[178] High system efficiencies were achieved in two system variations, (i) an upstream reforming reactor with a syngas based chemical looping and (ii) a direct bioethanol chemical looping system. The total energy efficiencies were 59.78% with an electric power output of 13% and 63.66% with an electric power output of 7%. The carbon capture rate was > 99% in both plant simulations. The conventional reforming system with a gas-liquid absorption as a benchmark yielded efficiencies in the range of 53 – 58%, while enabling a carbon capture efficiency of > 99%.

Gopaul et al.[179] investigated the conversation of unconventional biomass. Three types of biomass were evaluated, assuming the absence of sulphur and nitrogen components. Poultry litter was chosen over wood pellets and oak pellets because of the higher hydrogen yield. Tar products formed during the biomass gasification process were not separated but fed into the chemical looping fuel reactor. Reduced iron and remaining tars were separated from the

gaseous products and fully oxidized in the steam reactor. Both reactors yielded a hydrogen rich synthesis gas (H_2, CO_2, CO, CH_4, H_2O), which was utilized in a reformer at 500 °C to oxidize the residual methane and maximize the hydrogen output. A hydrogen yield of 1.60 $kmol \cdot kmol_{feed}^{-1}$ diluted with 34% CO_2 and 2.3% H_2O with a final hydrogen purity of 63% was obtained. A reference water-gas-shift system generated 0.97 $kmol \cdot kmol_{feed}^{-1}$. Sanz et al.[180] calculated the hydrogen production cost using a two-reactor chemical looping system. A syngas stream with a mass flow of 27820 $kg \cdot h^{-1}$ produced by biomass gasification was assumed as feed. The feed stream contained high amounts of steam and a low reducing potential, thus the stream was cooled-down to condense the water before entering the fuel reactor. Two reactors were assumed in reduction mode per each reactor in oxidation mode, with a total of 12 reactors for handling the used feed stream. The system calculations were based on thermodynamic considerations of the Baur-Glaessner diagram. The reduction off gas was burned to provide heat for the system. Under the consideration of equipment costs, amortization and operation costs a hydrogen production of 4786 $t \cdot y^{-1}$ with production costs of 2.13 $€ \cdot kg^{-1}$ hydrogen were obtained. Comparative data based on a conventional water-gas-shift system resulted in production costs of 1.76 $€ \cdot kg^{-1}$. The techno-economic evaluation indicated higher investment, operation and maintenance costs (O&M) for chemical looping hydrogen systems compared to state-of-the art technology. The high degree of technological complexity and the small number of large-scale applications are the two main cost factors. However, under the consideration of costs per energy output the direct biomass chemical looping system has the lowest costs due to the high system efficiency and low carbon capture energy penalty.[175,180]

Edrisi et al.[136,181] proposed a three-reactor chemical looping technology to produce pure streams of hydrogen and nitrogen as feed for an ammonia production plant and a third stream of pure carbon dioxide for sequestration. In the fuel reactor an iron based oxygen carrier completely converted CH_4 to CO_2 at 726 °C. In the steam reactor a pure hydrogen stream was produced by partially oxidizing iron with steam at 723 °C. In the air reactor, a pure nitrogen stream was generated at 880 °C by fully consuming oxygen in the air stream and completely oxidizing the solid material. The fuel and air fed and the oxygen carrier fed were varied to optimize the operation conditions with regard to the product streams. The ratio OC/CH_4 of 4.0 and the ratio air/CH_4 of 3.206 were found to enable the production of pure streams, while maximizing the reduction degree of the solid material. $MgAl_2O_4$ was added as support material with a ratio of $MgAl_2O_4/CH_4$ of 6 to improve the heat integration of the system.[181] The simulation yielded a hydrogen production efficiency of 80.2%.[181]

2.6 Kinetic Studies

Several papers have been published on the kinetic characterization of the reduction and oxidation of iron based oxygen carriers. Besides pure iron oxygen, supported samples and the interactions between the active components and the supporting components were studied. The kinetic data and redox models gained is important information for modelling large-scale chemical looping plants and process optimizations. The presented data is summarized in table 9. Zhu and Hua et al.[182–184] analyzed the reduction stage distribution in a fixed bed reactor under fuel breakthrough operation. Reductions were performed at 900 °C with a mixture of CO and CO_2 in a tubular reactor divided into 10 separated segments by quartz cotton. The oxygen carrier analyses indicated an uneven solid conversion caused by the reaction front with their different reduction kinetics moving through the reactor (figure 22). The first two layers contained Fe and FeO with a mass percentage of 85 wt% and 7 wt% respectively, while FeO and Fe_3O_4 were found in the remaining 8 layers. In the consecutive steam oxidation the segments 1 – 6 contributed to 90% of the produced hydrogen. Hertel et al.[185] identified the two zones with a stable conversion which corresponded to the reduction zones of Fe_3O_4/FeO and FeO/Fe described by the Baur-Glaessner diagram. Stable zones were separated by transition periods, which are induced by limited gas-solid reaction rates. The simulation results indicated that the travel time of the reaction zones is 3 – 4 orders of magnitude of the gas phase movement. Zhu et al.[182] separated each reduction step by adapting the CO/CO_2 feed-ratio according to the phase equilibrium. The reaction rates of the reductions Fe_2O_3/Fe_3O_4 and FeO/Fe possessed similar characteristics with a rapid increase to a stable maximum. Both steps ended with a fast decline until the conversion rate dropped. Fe_2O_3 was completely reduced, while 36% of FeO remained unreacted after step 3. The second step Fe_3O_4/FeO had the slowest reduction rate, approximately one order of magnitude lower than the other two, with a continuous linear decrease and a reaction stop at a solid conversion of roughly 38%, meaning that it should be the focus of material optimization. The reaction front velocities were in the order Fe_2O_3/Fe_3O_4 > FeO/Fe > Fe_3O_4/FeO. Reduction simulations of Fe_2O_3 with CO in a temperature range of 973 K – 1173 K were executed with the phase boundary kinetic model.[184] However, the addition of 50 wt% Al_2O_3 revealed a transition from a phase boundary to a diffusion controlled kinetic model to better match the experimental results. An explanation was provided by SEM analysis. Larger pores were found in the reduced pure sample, whereas the supported oxygen carrier possessed grain clusters with reduced porosity, which are expected to hamper the gas diffusion. Kang et al.[186] performed an extensive isothermal kinetic investigation on iron oxide supported with 80 wt% ZrO_2 at temperatures of 740 – 900 °C. The reduction with methane was separated into two steps Fe_2O_3 -> FeO and FeO -> Fe, while the reduction with H_2 and CO was considered a one-stage reaction. According to the Hancock and Sharp method the phase-boundary controlled mechanism was suitable for describing all reduction and oxidation reactions except the second step of the methane reduction, which showed a linear behavior. Nasr et al.[187] studied the reduction kinetic of a natural iron ore with CH_4. Reactions were performed in a TGA in the temperature range of 800 – 950 °C. Based on the Hancock and Sharp method, a phase boundary controlled mechanism was used to describe the solid conversion. The

impurities in the natural ore, mainly SiO_2, CaO, MgO and Al_2O_3 were expected to lower the activation energy which resulted in a value of 215 kJ·mol^{-1} for the reduction reaction.

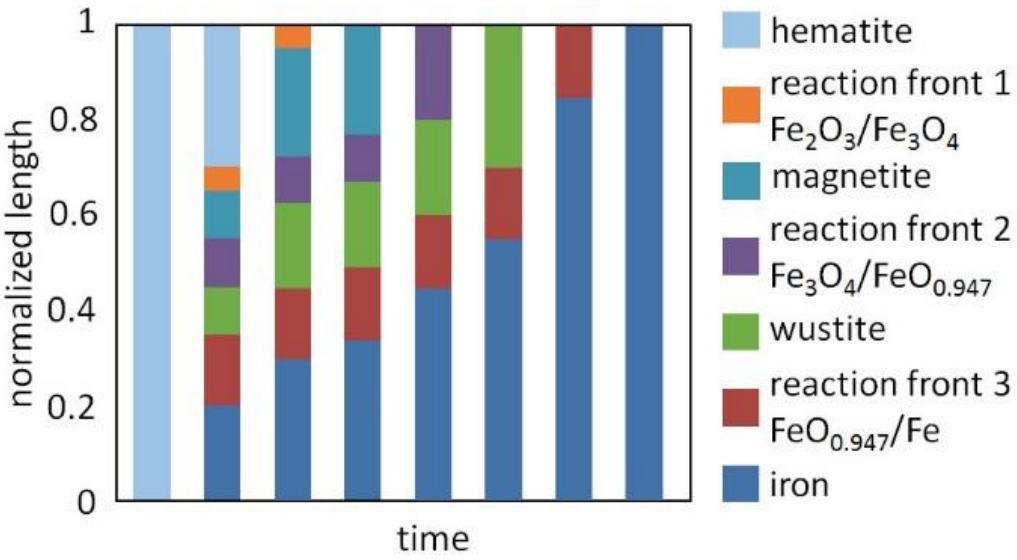

Figure 22: Schematic temporal progression of the reaction fronts in a fixed bed at 800 °C.[183] ℓ

Monazam et al.[188] analyzed the reduction kinetics of hematite particles to wustite with 20% hydrogen in a thermogravimetric analysis system (figure 23). Changing values were obtained for the activation energies, depending on the solid conversion initially decreased from 23 to 8 kJ·mol^{-1} (0.025 < solid conversion < 0.1) followed by an increase to 47 kJ·mol^{-1} (0.1 < solid conversion < 0.33) and finally declined to 30 kJ·mol^{-1} (0.33 < solid conversion < 1), suggesting a double-step reduction kinetic. In a temperature range of 700 – 800 °C a 1D nucleation growth model including an induction period was used to describe the reaction process. At temperatures beyond 900 °C the induction period diminished and the single-step nuclei growth reaction became dominant. A similar approach was used for the reduction kinetics of hematite with CH_4 (15 – 35 vol%).[189] However, the kinetic models did not properly describe the reaction. The analysis of the activation energy corresponding to the solid reduction degree indicated a descending trend from 56 to 36 kJ·mol^{-1} with the conversion progressing from 0.1 to 0.5. Hence, a multi-step parallel model with a superposition of a first order reaction and a nucleation model was applied. Activation energies for the two reaction steps of 34.4 ± 0.5 kJ·mol^{-1} and 39.3 ± 1.6 kJ·mol^{-1} were obtained. Zhang et al.[190,191] analyzed the reduction kinetics of 25 wt% and 45 wt% Fe_2O_3 on Al_2O_3 with a low concentrated CH_4 feed of 0.5%. The reduction step of Fe_2O_3 -> Fe_3O_4, with a phase change of rhombohedral to cubic, was described with the 2D growth of nuclei up to solid conversions of 0.7. At a higher solid conversion, a 3D nuclei growth Avrami Erofeev mechanism yielded better fitting results. The reduction for magnetite to $FeAl_2O_4$ was significantly slower and described by a diffusion-controlled reaction mechanism. The 3D diffusion Jander reaction mechanism fitted best and indicated a strong correlation between the iron content of the sample and the reduction reactivity.

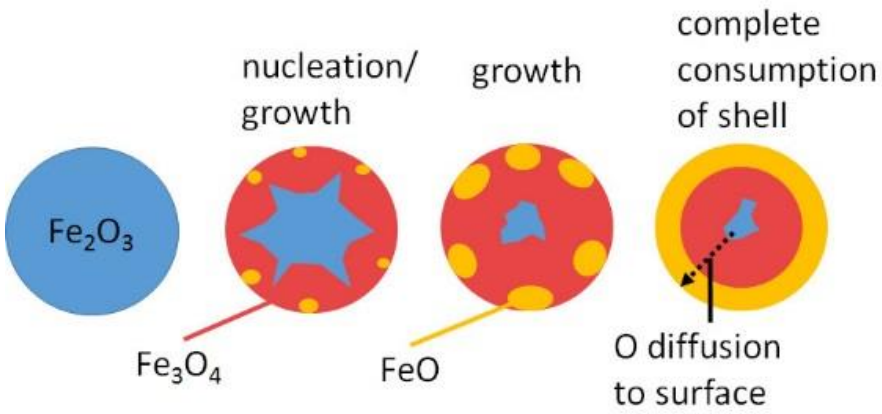

Figure 23: Schematic representation of the progression of the reduction of Fe_2O_3 to FeO.[188] ℓℓ

Ksepko et al.[192] compared the reduction of Fe_2O_3 supported on 20 wt% TiO_2 with a bimetallic sample of Fe_2O_3/CuO supported on Al_2O_3 (60/20/20 wt%) with hydrogen in the temperature range of 600 – 950 °C. The reaction model of a first order reaction and a phase boundary controlled mechanism was found to be suitable for the Fe_2O_3 sample, whereas the 3D diffusion Jander equation and the first order reaction yielded better results for the reduction of the bimetallic oxygen carrier. Jeong et al.[193] investigated the redox kinetics of iron oxides with three different main iron phases FeOOH, Fe_2O_3 and Fe_3O_4 with initial surface area of 93.5, 7.5 and 1.7 $m^2 \cdot g^{-1}$. Hence, the transformation to bulk Fe_3O_4 with a homogenizing of the different grain sizes was observed. The Jander equation was used to determine the kinetic parameter of the redox reaction. It was suggested that the reduction and oxidation of magnetite led to the highest reaction rate and lowest activation energy. Liu at el.[194] investigated the reduction kinetic of wustite particles in a fluidized bed using H_2 and CO. The solid reduction and the formation of metallic iron were divided into three separated conversion stages. The first stage with a solid conversion of $0 < X < 0.05$ was identified as the partial depletion of oxygen in wustite. In the second stage $0.05 < X < 0.2$ surface nucleation and the formation of isolated Fe grains took place. The reaction mechanism was controlled by dissociative adsorption and described by a linear reaction model. The final stage $0.2 < X < 1$ was identified as the thickening of the iron particle with a final formation of a uniform Fe product layer and the changing of the reaction rate to a diffusion limiting system. The random pore model was able to describe the solid conversion reactions. The three stages were also measured when mixtures of H_2 and CO were applied resulting in a superposition of their non-interacting reduction rates. The hydrogen reduction rate was significantly faster than the CO reduction rate but the overall reduction rate was dominated by the slow diffusion of oxygen atoms in the solid particle.

Plou et al.[195] incorporated the influence of thermodynamic equilibriums into differential kinetic measurements to reduce deviations during the initial steam oxidation phase and the transition phases. The Johnson-Mehl-Avrami-Kolmogorov model, which provided the differential kinetic data was amalgamated into an integral data fit method based on the Levenberg-Marquardt method by minimizing the sum of square deviation. The simulations

were able to take the equilibrium compositions and the moving reaction fronts in the fixed bed reactor into account and yielded improved fitting results. The calculations suggested a decrease of the oxidation activity after consecutive cycles, meaning that the oxidation reaction was primarily responsible for the degradation of the oxygen carrier. Stehle et al.[196] performed steam oxidation experiments with a pristine iron rod. At low steam concentrations in the oxidizing feed, a linear correlation with the produced hydrogen was observed, however higher steam concentrations did not further improve the hydrogen production rate. A rapid increase in the production rate in the range of 1075 – 1175 K was found, which suggested a transition from the kinetically limited reaction to a diffusion-limited regime. A detailed investigation of the iron oxide layer after the oxidation indicated an average layer thickness of 5 µm, which deviated significantly in its width after consecutive cycles.[197] The oxide layer possessed a stoichiometric ratio of Fe_3O_4 at the outermost point. A linear decrease to an O/Fe ratio of 0.8 within 80% of the layer width was detected, followed by a sharp bend to zero. 70% of the surface thickness was able to participate in the oxygen exchange reaction with a continuous gradient of oxygen atom concentration, which explained the dominant diffusion limitation. The oxidation of an iron powder with steam in a fluidized bed environment by Singh et al.[198] showed two bends representing the transition of Fe/FeO and FeO/Fe_3O_4. The experimental validation results revealed some deviations from the thermodynamic simulations due to non-ideal mixing of the bed material. At a reaction temperature of 660 °C the influence of kinetic hindrance was clearly visible resulting in a low conversion. A temperature increase to 960 °C diminished the kinetic effects.

2.7 Conclusion

Hydrogen production by chemical looping is a very promising technology, where significant scientific progress has been made over the last years. In the area of oxygen carrier development, the focus was on iron as the active component. New synthesis methods and material composition have shown that mixtures with high melting support materials or the incorporation of iron into thermally stable structures, such as perovskites, can successfully enable long-term cycle stability and a satisfying material strength. The addition of different metal oxides, which act as promoters, enhanced the redox properties and permitted the fabrication of specialized and selective oxygen carrier design for specific process conditions and feed stocks. Two reactor and three reactor moving bed systems in a power range up to 50 kW have been successfully operated. The experiments revealed stable conditions, a high fuel conversion and a continuous production of hydrogen with high purities. Although, some reactor and system developments using fixed bed technology were presented, most research was related to interconnected fluidized beds. Emphasis has been put on the modification of the chemical looping hydrogen process utilizing different feedstocks. Experimental studies and simulations have shown that the process can handle a variety of renewable resources, different fossil fuels and unconventional materials. The operation parameters were optimized to maximize the hydrogen yield. Energy and exergy analyses showed high efficiencies and excellent capabilities for carbon capturing and thus proved the competitiveness of these systems compared to well-established technologies. However, despite the calculated high system efficiencies in system simulations, the chemical looping hydrogen technology still requires prototype plants to be tested in large scale applications in long term operation, which would then demonstrate the advantages under real application scenarios. Furthermore, the oxygen carriers, which indicated satisfying performance in the lab environment, still need to demonstrate their applicability under authentic conditions.

3 Oxygen Carrier Preparation

3.1 Introduction

The development of suitable oxygen carriers is a critical sub-area in the field of chemical looping technology. Besides a high amount of exchangeable oxygen, a high cycle stability and fast redox kinetics are of great importance. In previous work at Graz University of Technology, Markus Thaler has identified iron/iron oxide as a very promising candidate for chemical looping hydrogen production.[51,82,199] Advantageous properties are (i) the high amount of exchangeable oxygen, (ii) it is easy to handle, (iii) nonhazardous and non-harmful to the environment. Due to the abundance and simple accessibility, iron oxide is an inexpensive material. However, pure iron is prone to sintering beyond a temperature of 600 °C and thus deactivates quickly. Additionally, in deep reduced stages it becomes catalytic active, which enables its application in industrial processes for instance in water-gas-shift reactions.[200] This catalytic activity also increases the risk of carbon formation, and the contamination of the produced hydrogen.

In order to investigate a suitable preparation method, which enables fast and easy production of oxygen carriers for small-scale applications (primarily in the Flex Fuel Reformer, described in the patent WO2016011473 A1[52]) the mechanical mixing of powders was selected. A preliminary study of this preparation method was executed in December 2012 at the Technikum Maschinenfabrik Eirich in Hardheim Germany using both an intensive mixer R02E with an enclosed mixing vessel and a pelletizing disc in open design. After an experimental investigation of the prepared samples, the mechanical mixing method in the intensive mixer was classified as eligible for a detailed evaluation with different compositions. The application of the pelletizing disc was not taken into further consideration due to unfavorable results regarding pellets size distribution. Finally, an intensive mixer EL1 was rented from Maschinenfabrik Eirich and operated for one month in the laboratory.

3.2 Material and Methods

3.2.1 Mixing and pelletizing equipment

Two different systems for mixing an pelletizing were investigated in the Technikum Maschinenfabrik Eirich, the pelletizing disc TR04 and the intensive mixer R02E. The pelletizing results are summarized in table 1 and table 2 in chapter 3.3.1.

A pelletizing disc (figure 24, left) consists of a rotating bowl with a variable rotation speed and a fixed skimmer to prevent powder agglomeration on the walls. The bowl is tilted at an angle of 45° – 60°. A dry powder mixture is placed at the bottom of the vessel. The particles are entrained by the rotating disc to the upper part and fall back to the bottom due to the incline. The two parameters, rotation speed and angle, correlate with the kinetic energy of the agitated particles and determine the particle mean size and size distribution. Additional parameters, which need to be taken into account, are (i) the disc wall height, (ii) the nature and size of the feed, (iii) the residence time of the feed and (iv) the feed-rate. The agglomeration of the powder is initialized by spraying water into the disc forming small seeds of mass. These small seeds while performing the circulated movement grow in size by rolling-wet-agglomeration and forming spheres. The amount of liquid and the dosing procedure are additional process parameters. After reaching a specified diameter the pellets are extracted over the disc walls, while the remaining powder and abrasion products remain in the system for further processing enabling a narrow size distribution in the harvested sample.[201]

The intenisve mixer R02E (figure 24, center) consists of an enclosed vessel at a tilt position, which rotates at a very high speed. A skimmer is fixed to the system to prevent agglomeration on the reactor wall and base. In the consentric postition of the vessle a multistage mixing tool rotates in the opposite direct and thus enabling a counter-current movement of the powder at a high speed with pronounced mixing. The closed system allows the application of fine powders without a high dust contamination. The agglomeration liquid (water) is added via an orifice in the cap. The R02E has a capacity of 3 – 5 l and 5 kg.

In our own laboratory the intensive mixer El1 (figure 24, right) was utilized, which has the same features and operation conditions as the R02E but a lower capacity of 1 l. The pelletizing results between the two devices yielded comparable results. The results are summarized in table 2 in chapter 3.3.1.

3.2.2 Chemicals and substances

At the Eirich technical center iron oxide (Fe_2O_3) with a mean particle size of < 1 µm and a bulk density of 760 $g \cdot l^{-1}$ was applied as bulk active substance. α-Al_2O_3 (Alfa Aesar, 99.9%, 20-50 µm spherical powder) was utilized as support material and polyvinyl alcohol (Optapix PAF2, 5% and 10%) as a binder. Water (untreated) was added as agglomeration substance.

The pelletizing experiments at Graz University of Technology were performed with iron oxide powder (Alfa Aesar, 99.9%, 325 mesh, 44 µm) as main component. As additives, α-Al_2O_3 (Alfa Aesar, 99.9%, 20 – 50 µm), CuO (Alfa Aesar, 97%, 325 mesh, 44 µm), SiO_2 (Alfa Aesar, 99.5%, 325 mesh, 44 µm), CaOH (Alfa Aesar, 95%) and C (Sigma Aldrich, activated charcoal, 100 – 400 mesh, 37 – 149 µm) were utilized. Deionized water was used as agglomeration substance.

Figure 24: Pictures of the utilized pelletizing devices, a disc pelletizer (left),[201] ‡ the intenisve mixer R02E (center), and El1 (right) both from the Maschinenfabrik Eirich GmbH & Co. KG. ‡‡

3.2.3 Sample preparation

In a first step, a dry mixture of the materials was added to the vessel and homogenized. Water was slowly added during continuous mixing for the agglomeration. Upon reaching the desired pellet diameter the process was stopped and the solid material was dried at 100 – 150 °C in air and finally fractionized. The fractions were (i) < 0.5 mm, (ii) 0.5 – 1 mm, (iii) 1 – 2 mm, (iv) > 2 mm. The fractions < 0.5 mm and > 2 mm were combined to a residual fraction.

3.2.4 Thermogravimetric analysis

Samples were analyzed in a thermogravimetric analyzer (STA 449C Jupiter Netzsch) with a steam generator (aDROP containing a Bronkhorst hi-tec liquid flow controller). 200 mg of each sample (particle size 0.5 – 1mm) was placed on a crucible made of Al_2O_3 in the TGA system. The system was heated to a temperature of 800 °C with a heating rate of 10 °C·min^{-1} in N_2. Reductions were performed with 100 ml·min^{-1} H_2 and 30 ml·min^{-1} N_2 for 30 minutes. The oxidations were executed with 80 mg·min^{-1} of deionized water mixed with 30 ml·min^{-1} N_2 for 30 minutes. Reductions and oxidations were separated by a purge phase of 10 minutes with 30 ml·min^{-1} of N_2. The weight change of the iron oxide under isothermal conditions was analyzed over consecutive redox cycles.

3.3 Results

3.3.1 Sample compositions

The pelletizing experiments in the Technikum at the Maschinenfabrik Eirich revealed the feasibility of this preparation technique in an intensive mixer. Pellets with a size distribution of 0.5 – 5 mm and with a moisture content 13 – 15.5 wt% were prepared. The sample solely prepared in the disc pelletizer had a significantly higher moisture content of 19 wt%. Each sample required an agglomeration time of 15 – 25 minutes. The addition of a binder narrowed the size distribution, however at the expense of additionally forming very large grains unusable for further processing (figure 25, left). Solely water widened the size distribution with fewer grains beyond the upper and lower limits.

Figure 25: Left: the particle size distribution of the sample V5 induced by the binder Optapix PAF 2. Right: reactor vessel with a solid tense layer at the wall and bottom.

During the sample preparation experiments at Graz University of Technology all sample compositions were successfully pelletized in the intensive mixer with the single exception of the sponge iron V28. This preparation was accompanied by very loud noises and heavy vibrations of the system, possibly by intense friction of the iron precursor material. Hence, the process was stopped prematurely to prevent damage of the mixer, which resulted in insufficient agglomeration. Depending on the solid composition and on the materials and the amount of additives different agglomeration behaviors were observed. Each new sample required a unique preparation procedure with small amounts of water added in steps of 1 – 2 ml and a settling phase to prevent an excess of humidity and too fast particle growth. The reproducibility of each composition regarding the required water was very high and allowed for a quick reproduction.

The critical negative aspect of this preparation method was the production yield. When the agglomeration reagents was applied a packed layer of the powder mixture started to form on the walls and the bottom of the vessel (figure 25, right). These layers hindered the pelletizing process but moreover the material was not pelletized and was lost in the procedure. As a result an average yield of 72% was obtained, while the residual material was disposed of. A

pellet size of 1 – 2 mm was targeted during the preparation procedure. The fractions 0.5 – 1 mm and 1 – 2 mm were successfully utilized in redox experiments in thermogravimetric analysis and larger fixed bed reactor systems (figure 26). The average yield of useable material of those two fractions combined was approximately 60%. The remains consisted of too small and too large pellets, the latter were easily crushed and fractionized to increase the desired particle size yield. The mechanical mixing method in an intensive mixer proved to be very effective and can be easily up-scaled to an industrial level. However the current operation method generates significant amounts of rejects, which have to be considered and recycled.

Figure 26: Sample V7 with a composition of 90 wt% Fe_2O_3 and 10 wt% Al_2O_3 with a diameter of 1 – 2 mm. Fresh sample (left) and after cyclic experiments (right).

Table 1: Results table of the sample compositions and pelletizing results at Maschinenfabrik Eirich GmbH & Co. KG.

Samples	Fe_2O_3	Al_2O_3	Optapix PAF 2 (10%)	Optapix PAF 2 (5%)	Mixing	Mixing	Bulk density	Moisture
	g	g	g	g	rpm	device	$g \cdot l^{-1}$	%
V1	2750				2500/3000/1000/750/500	R02E	1520	12.9
V2	3000		540		2000/2500/750/500	R02E	1450	13.1
V3	2640			800		TR04	1080	19.0
V4	2700	300		490		R02E, TR04	870	14.6
V5	2700	300		585	2500/750/500	R02E	1280	14.4
V6	2700	300	590		2500/500	R02E	1370	14.0
V7	2700	300			2500/750	R02E	1200	15.5

Table 2: Results table of the sample compositions and pelletizing results at Graz University of Technology.

Samples	Precursor weight								Fraction weight			
	Fe_2O_3 g	Al_2O_3 g	SiO_2 g	CuO g	C g	CaO g	H_2O ml	Mixing rpm	0,5 – 1 mm g	1 – 2 mm g	Residual g	Moisture %
V1 - 100% Fe_2O_3	406.2						70	2500	85.2	84.4	-	11
V2 - 90% Fe_2O_3 10% Al_2O_3	639.4	71.5					120	2500	79.4	224.0	219.6	13
V3 - 80% Fe_2O_3 20% Al_2O_3	543.2	135.7					130	2500			548.8	17
V4 - 80% Fe_2O_3 20% Al_2O_3	534.8	133.6					137	2500	51.2	112.0	328.3	14
V5 - 70% Fe_2O_3 30% Al_2O_3	455.1	196.1					144	2500	9.9	83.1	288.4	18
V6 - 70% Fe_2O_3 30% Al_2O_3	315.2	135.5					106	2500	20.4	131.9	123.6	18
V7 - 85% Fe_2O_3 15% Al_2O_3	553.1	98.1					134	2500	132.9	195.9	139.4	16
V8 - 90% Fe_2O_3 10% SiO_2	585.1		65.2				105	2500	26.0	166.7	338.5	13
V9 - 80% Fe_2O_3 10% Al_2O_3 10% SiO_2	520.0	65.5	65.6				121	2500	52.7	240.6	276.4	15
V10 - 80% Fe_2O_3 10% Al_2O_3 10% CuO	519.7	65.8		69.0			120	2500	8.4	147.9	214.3	-
V11 - 85% Fe_2O_3 10% Al_2O_3 5% CuO	552.5	65.4		33.7			127	2500	123.4	234.7	59.2	2
V12 - 75% Fe_2O_3 10% Al_2O_3 15% CuO	487.9	65.2	99.1				110	2500	45.8	121.5	319.0	14
V13 - 75% Fe_2O_3 10% Al_2O_3 15% CuO	488.2	65.6	98.6				115	2500	124.4	174.0	86.2	13
V14 - 85% Fe_2O_3 10% SiO_2 5% CuO	552.6		64.8	32.7			100	2000	17.9	180.2	272.6	-
V15 - 80% Fe_2O_3 10% SiO_2 10% CuO	520.0		65.0	65.3			95	2000	14.9	140.7	359.0	12
V16 - 75% Fe_2O_3 10% SiO_2 15% CuO	487.2		65.0	97.9			96	2000	71.7	281.6	96.5	11
V17 - 80% Fe_2O_3 10% Al_2O_3 10% C	520.7	65.0			65.4		178	1500	35.6	260.6	179.3	22

Table 2: Results table of the sample compositions and pelletizing results at Graz University of Technology (continued).

Samples	Precursor weight								Fraction weight			
	Fe_2O_3 g	Al_2O_3 g	SiO_2 g	CuO g	C g	CaO g	H_2O ml	Mixing rpm	0,5 – 1 mm g	1 – 2 mm g	Residual g	Moisture %
V18 - 85% Fe_2O_3 10% Al_2O_3 5% C	552.5	65.6			32.8		150	1700	97.0	262.5	62.8	18
V19 - 75% Fe_2O_3 10% Al_2O_3 15% C	488.1	66.5			97.6		209	1700	108.5	228.3	143.2	25
V20 - 50% Fe_2O_3 50% Al_2O_3	220.0	220.0					120	2000	8.6	124.4	127.3	21
V21 - 80% Fe_2O_3 20% SiO_2	523.0		130.0				100	2000	56.4	265.5	174.2	12
V22 - 95% Fe_2O_3 5% SiO_2	618.1		33.3				107	2000	96.0	351.6	146.8	13
V23 - 90% Fe_2O_3 5% Al_2O_3 5% SiO_2	585.6	32.7	32.8				110	2000	99.6	274.9	108.1	14
V24 - 80% Fe_2O_3 10% Al_2O_3 10% CaO	521.6	68.0				64.3	120	2000	151.3	194.8	124.6	15
V25 - 80% Fe_2O_3 20% Al_2O_3	520.1	133.8					137	2000	146.6	132.1	109.8	15
V26 - 70% Fe_2O_3 20% Al_2O_3 10% CuO	455.2	130.4		65.5			130	1700	116.5	183.6	91.0	14
V27 - 80% Fe_2O_3 20% Al_2O_3	520.2	129.8					133	1800	109.0	156.4	183.7	16
V28 - 80% Fe_2O_3 20% Al_2O_3	521.2	130.0					130	1800	29.1	12.3	369.0	16
V29 - 90% Fe_2O_3 10% CuO	586.2			65.2			96	1800	172.0	231.4	66.8	12
V30 - 80% Fe_2O_3 20% Al_2O_3	521.8	129.8					131	1800	103.8	263.2	88.9	16
V31 - 100% Fe_2O_3	649.0						102	2000	130.8	190.6	127.2	13
V32 - 80% Fe_2O_3 10% Al_2O_3 10% CuO	520.2	65.0		65.9			107	1800	25.1	244.7	249.8	14
V33 - 90% Fe_2O_3 5% Al_2O_3 5% CuO	585.4	38.4		46.1			109	1800	44.0	247.5	230.4	14

Table 2: Results table of the sample compositions and pelletizing results at Graz University of Technology (continued).

Samples	Precursor weight								Fraction weight			
	Fe_2O_3 g	Al_2O_3 g	SiO_2 g	CuO g	C g	CaO g	H_2O ml	Mixing rpm	0,5 – 1 mm g	1 – 2 mm g	Residual g	Moisture %
V34 - 85% Fe_2O_3 5% Al_2O_3												
10% CuO	552.7	32.7		65.5			99	1800	30.3	219.5	314.1	13
V35 - 95% Fe_2O_3 5% Al_2O_3	617.6	32.5					112	1800	123.7	181.1	136.1	14
V36 - 70% Fe_2O_3 20% Al_2O_3												
10% C	456.7	131.4		55.1			208	1800	101.8	148.8	168.2	24

3.3.2 Thermogravimetric results

Concurrent to the sample preparations, selected oxygen carriers were analyzed in a thermogravimetric analysis system to evaluate their cycle stability and reaction kinetics, which are depicted in figure 27. These preliminary results were used for the selection of additional sample compositions and future extended characterization. Additives with an auspicious cycle stability for instance Al_2O_3 or CuO were utilized for additional sample compositions.

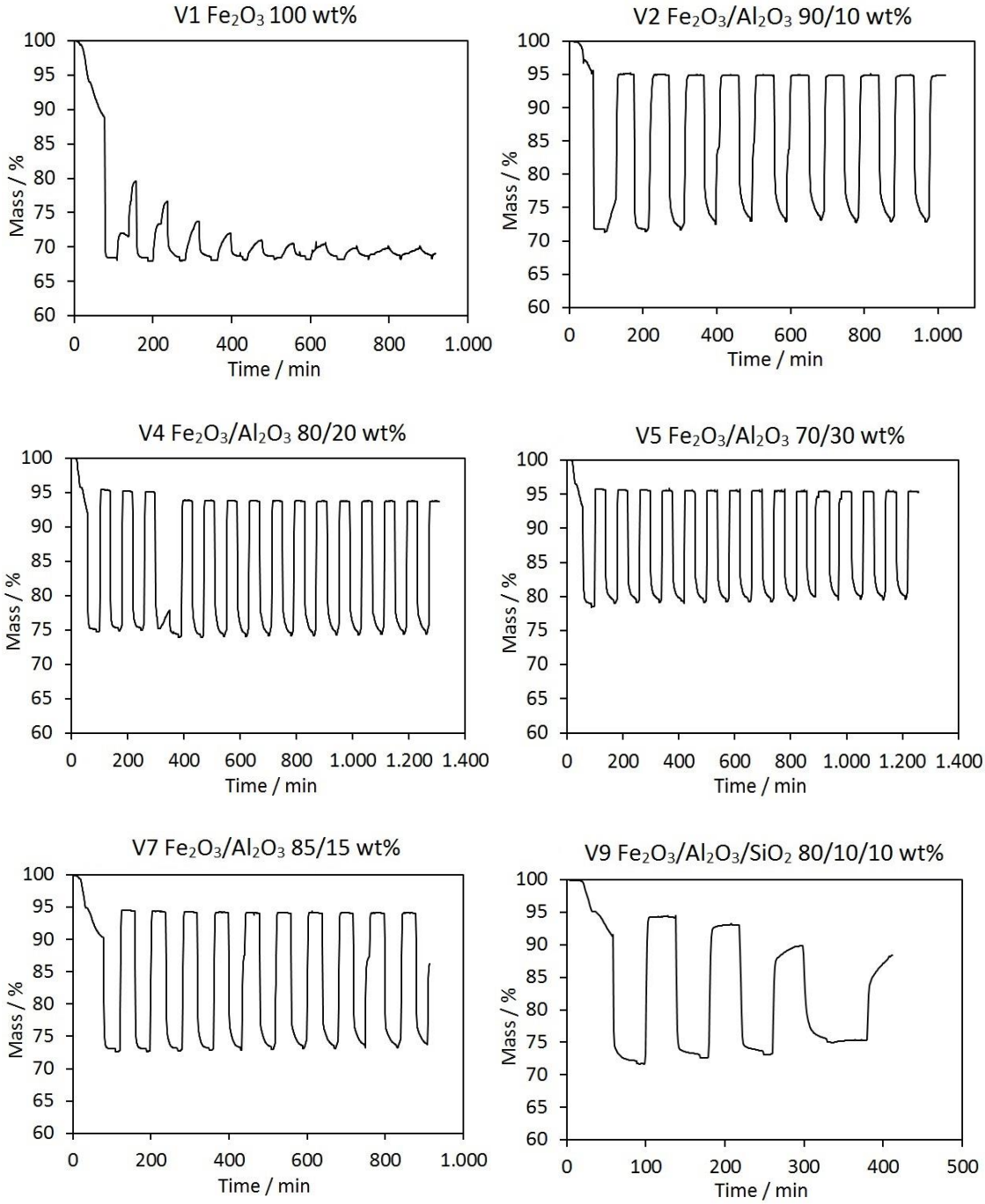

Figure 27: Results of the cyclic redox experiments in the thermogravimetric analysis system.

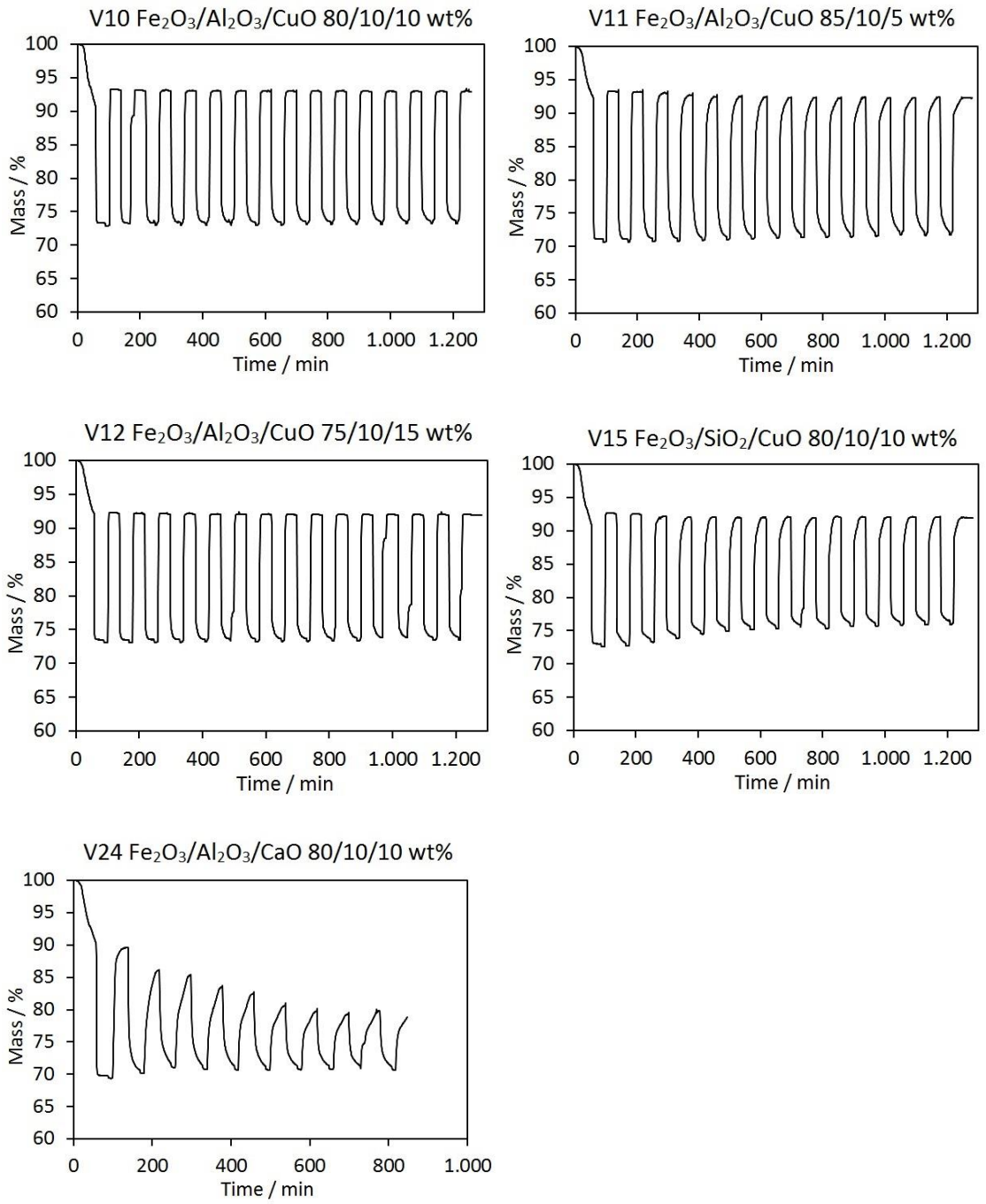

Figure 27: Results of the cyclic redox experiments in the thermogravimetric analysis system (continued).

Pure iron is prone to sintering thus the sample V1 (figure 27) immediately loses its cyclability in the first cycle and becomes inactive within a few subsequent redox reactions. A significant stability loss was also observed for the samples V9, V24 (Al_2O_3/SiO_2 10/10 wt% and Al_2O_3/CaO 10/10 wt%) (figure 27). SiO_2 has been reported by literature as an effective stabilizing additive for chemical looping up to 750 °C. Beyond 750 °C a strong deactivation was observed, which was related to agglomeration of SiO_2 particles.[99] The experiments in the thermogravimetric analysis system were conducted at 800 °C, which explains the severe deterioration of the sample.

CaO on the other hand was successfully utilized with iron oxides as oxygen carrier at high temperatures up to 900 °C. Improved stability and reactivity were observed and attributed to the formation of calcium ferrites.[99–101] However, the CaO/Fe_2O_3 sample V24 prepared by mechanical mixing did not show an enhanced redox reactivity. This indicates that the mechanical mixing method does not provide a homogenous distribution of CaO between the iron oxide particles and thus calcium ferrites were not formed sufficiently to enhance the redox properties.

The addition of small amounts of Al_2O_3 led to a distinctive improvement of the cycle stability compared to pure iron. This behavior has already been reported in literature and was reproducible by the mechanical mixing preparation technique.[82,102,105] The samples V4 and V7 with 20 or 15 wt% of Al_2O_3 respectively possessed the highest stability. All samples with varying Al_2O_3 content indicated a slightly reduced weight change within the first cycles and a stable behavior afterwards. This observation is related to the formation of the unreactive component hercynite $FeAl_2O_4$. The presents of hercynite was verified by XRD in subsequent test series and is further discussed in the chapter 5. The increasing content of Al_2O_3 and the improved stability are accompanied by lower oxygen exchange capability and thus a reduced hydrogen production capacity.

The amount of produced hydrogen per sample mass in each cycle of the most stable sample compositions is analyzed in figure 28. All samples regardless of their additives are prone to a continuous deterioration never reaching a stable condition. The amount of produced hydrogen in the initial cycle lies within the range of 22 – 30 $mg(H_2)\cdot g(oc)^{-1}$ and is related to the content of iron oxide as active component. The proportional difference in produced hydrogen between the samples corresponds to the amount of iron oxide with deviations between 1 wt% and 5 wt%. This suggests that the mechanical mixing method enabled the preparation of desired sample compositions by dry mixing of the precursor powders. The specific amount of produced hydrogen is based on the theoretical amount of iron oxide in the sample. Elemental analysis of the actual oxygen carrier were net conducted at this time. Thus, theses variations can be induced by (i) inhomogeneous dispersion and discrepancy of the amount of active component in the samples, by (ii) incomplete conversion of the solid material and by (iii) chemical interaction between the sample components.

The percentage loss of the four most stable samples is depicted in figure 29. The addition of 15 wt% and 20 wt% of Al_2O_3, in the sample V4 and V5, improved the iron stability limiting the

production loss to roughly 0.5% per each cycle. The most promising results were obtained by the addition of CuO to Al_2O_3 supported iron samples. A composition with 10 wt% and 15 wt% CuO (samples V10 and V12) indicated a very high stability within 15 cycles with a loss of approximately 3.5%, which corresponds to 0.2% per cycle.

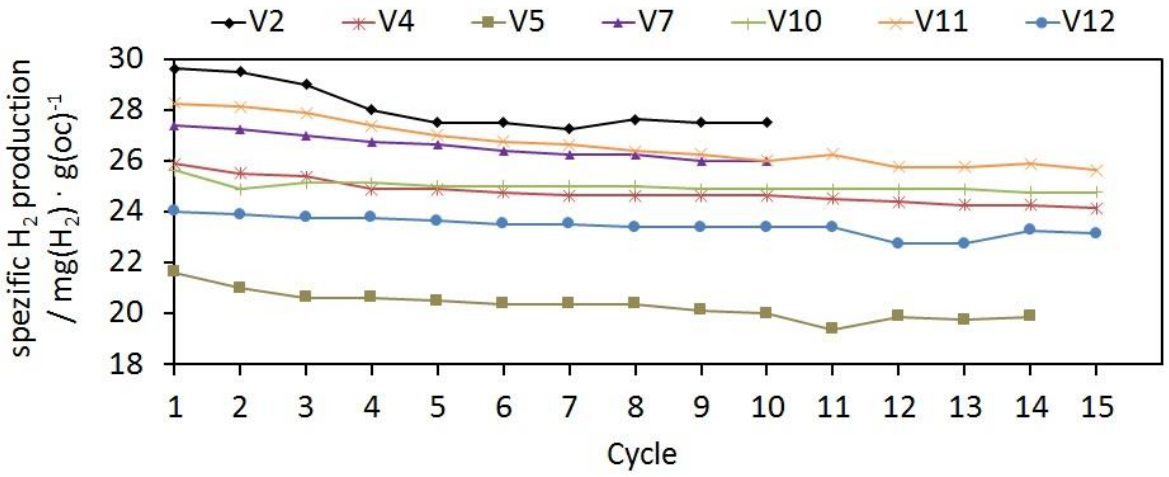

Figure 28: Produced hydrogen per mass oxygen carrier in each oxidation cycle.

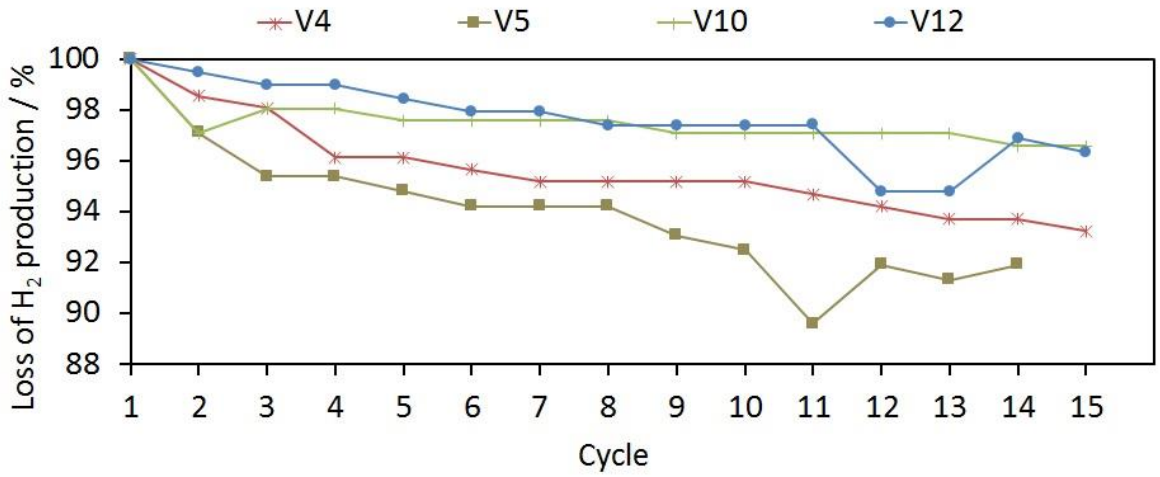

Figure 29: Percental loss of hydrogen production of the four most stable samples prepared by mechanical mixing.

Oxygen carrier with auspicious stability behavior were utilized in several test series. Experiments in the thermogravimetric system and fixed bed reactor with Al_2O_3 supported Fe_2O_3 were published in master's theses by Lammer[202], Malli[203] and Marius[204] and the doctoral thesis by Nestl[53] as well as in papers by Nestl et al.[55] and Voitic et al..[54,158] Details about the different measurement conditions and results can be found in the specific literature sources. The aforementioned literature confirms the results from the thermogravimetric analyses that Al_2O_3 stabilizes the iron based oxygen carrier against thermal sintering but is not able to prevent the loss of stability completely and thus a continuous degradation of the solid material is observed. The extend of stability improvement allowed detailed investigations of the samples in different lab-scaled reactor systems, however, leaves the sample compositions in combination with the preparation method, described in this work, unqualified for real applications.

The sample with the addition of 10 wt% CuO, which show very promising results, was investigated in detail by Karin Malli in her master's thesis. The measurements reassured the stable behavior of the oxygen carrier with a loss of produced hydrogen of 2.2% within 20 cycles. Still, the degradation continuously progressed and the samples never reached a completely stable condition. The sample behavior prepared by different synthesis routes were compared. A reference sample of Fe_2O_3 with Al_2O_3 and CuO prepared by co-precipitation indicated a significantly better performance reaching a stable behavior after approximately 6 cycles. Hence the preparation method is a critical parameter in the performance of an oxygen carrier. The most probable explanation for the difference between the mechanical mixing and the precipitation is the difference in homogeneity of the composition. Precipitation is performed from a liquid solution of the ingredients and thus enables a homogenous distribution on an atomic scale, whereas mechanical mixing utilizes dry powders with particles in the micrometer size. The utilization of nano-sized powder is not feasible in this setup because the vessel is not sealed airtight and would result in combination with the rotation speed in a high contamination of the working environment. The application of micro-meter sized particles leads to the formation of small islands of pure substances in the pellets, which are not stabilized by the higher melting oxides and tend to locally deteriorate. This behavior is clearly comprehensible in figure 30, where fair regions resemble Fe_2O_3 and dark regions resemble Al_2O_3. The compositions of the two separated regions was verified by EDX analyses (figure 31).

The results suggest that the current preparation procedure of mechanical mixing is not feasible for real application, however, it is a viable method for fast processing of new material compositions in sufficient quantities for prototype applications. Still, compared to wet-chemical synthesis critical shortcoming regarding stability and reactivity were observed.

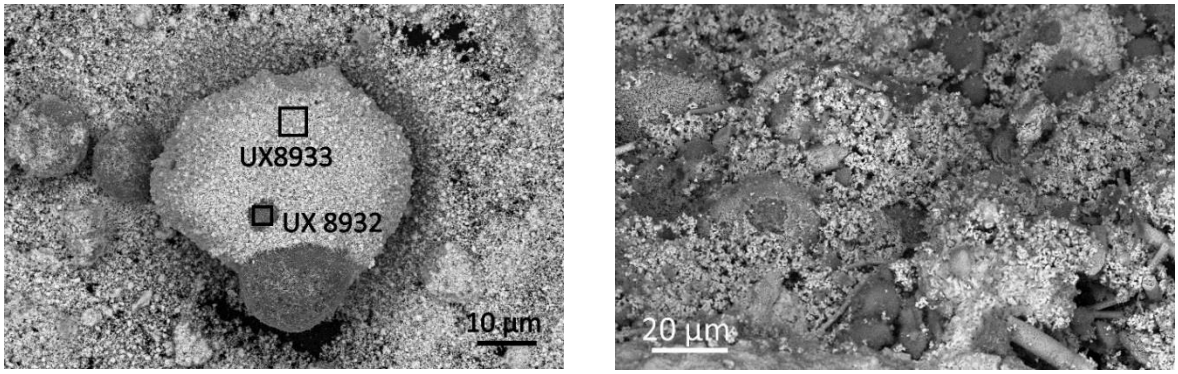

Figure 30: SEM images of two different iron samples with a composition of Fe_2O_3/Al_2O_3 90/10 wt% (sample V2). The unevenly distributed Al_2O_3 are resembled as dark regions within the bulk iron oxide.

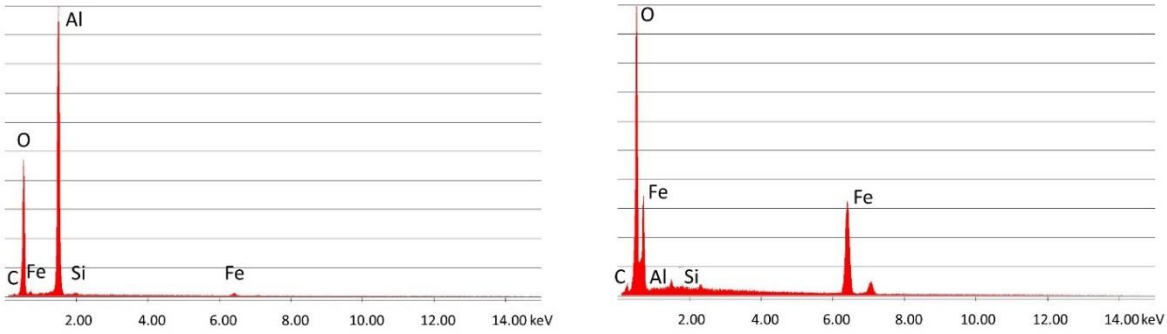

Figure 31: EDX analyses taken from the sample in figure 30 (Fe_2O_3/Al_2O_3 90/10 wt%, sample V2). Left: UX 8932, which consist of Al_2O_3 and right: UX 8933 the pure Fe_2O_3 particle.

3.4 Conclusion

The mechanical mixing of dry powders was investigated as a preparation method for iron based oxygen carriers for chemical looping hydrogen technologies. Two different systems, a rotating disc and an intensive mixer, with an enclosed rotating vessel, were utilized. Pellets with the chosen diameters were successfully manufactured in both systems. The intensive mixer proved to be superior in terms of pellet diameter distribution and spherical shape, simplicity and causing contaminations in the working environment. Following these preliminary results, an intensive mixer was rented and utilized for the preparation of various sample compositions. Iron oxide as active component was mixed with Al_2O_3, CuO, CaO and SiO_2 as stabilizing additives. Dry powders with calculated weight ratios were mixed and homogenized. The agglomeration was initialized by slowly adding water during the mixing. All sample compositions were successfully pelletized except the sample V28 due to intensive mechanical frictions, which used an iron-sponge as precursor. The parameters precursor composition, mixing-velocity, amount of water and feed rate of water, influenced the oxygen carrier size distribution and thus the quality of the preparation procedure.

Selected samples were analyzed in a thermogravimetric analysis system regarding its redox cycle stability for hydrogen generation. The samples were reduced with hydrogen at 800 °C and re-oxidized with steam. Pure iron immediately suffered from severe stability loss within the first redox cycle. Significant stability improvements were achieved by adding Al_2O_3 and CuO. The most promising results were obtained with the compositions Fe_2O_3/Al_2O_3/CuO 80/10/10 wt% and 75/10/15 wt%. However, all samples underwent a prolonged degradation over the 15 cycles and never reached a stable plateau. The coarse-grained precursor and the mixing method results in insufficient homogeneity in the samples, which mitigates the stabilizing effects of the additives.

The investigations proved the feasibility of the preparation method for quickly manufacturing large amounts of oxygen carrier samples with different compositions. However, the samples did not have satisfying cycle stability for commercialized applications compared to other, more complex, synthesis methods. This was related to the inhomogeneous particle distribution. Additionally, the current technique produced a significant amount of waste material, which has to be taken into account for commercialized applications by recycling.

4 Pressurized hydrogen production by fixed-bed chemical looping – Reduction experiments with hydrogen

4.1 Introduction

The essential parts of this chapter were published in the journal of Applied Energy, Volume **157**, November 2015, under the title *Pressurized hydrogen production by fixed-bed chemical looping*, by Gernot Voitic, Stephan Nestl, Michael Lammer, Julian Wagner and Viktor Hacker.[158]

Prior to this study successful proof of concept experiments of direct pressurized hydrogen production up to 11 bar(g) were conducted in our work group. The results were presented and explained in detail by Nestl et al..[55] Oxidations at elevated pressure were identified as a promising approach to improve chemical looping hydrogen systems by the direct production of pressurized hydrogen. This reduces the demand for downstream gas compression and thus raises the efficiency of the process.

Due to lack of available information and scientific data on compressed hydrogen production in CLWS systems with fixed bed reactor technology, experimental work on pressurized oxidations was conducted. The investigations focused on possible drawbacks of the production of compressed hydrogen by stability constrains of the oxygen carrier or operational limitations in a fixed bed reactor system up to 22 bar. Experimental contribution to this publication were made by Christoph Schaffer[205] and Bernhard Maunz[206] and details of their work can be found in their bachelor theses.

4.2 Material and Methods

4.2.1 High pressure hydrogen production

Cyclic reduction and oxidation experiments were performed in a fixed bed tube reactor. 3.57 g of an oxygen carrier (90 wt% Fe_2O_3 and 10 wt% Al_2O_3; particle diameter: 90 – 125 µm) were utilized. Both reactor ends were filled with inert material to preheat the reaction gases and to prevent movement within the fixed bed. The reactor was placed in a modified test rig (figure 32) for catalytic experiments: Microactivity-Reference of PID Eng&Tech. Additional heating and thermal insulation was added, which allowed water vaporization at higher system pressure. Standard valves and tubes were replaced by special materials to withstand temperatures of up to 400 °C.

An experimental cycle consisted of a reduction at ambient pressure and an oxidation at elevated pressure. The reduction reactions were performed at 750 °C with 25 $Nml \cdot min^{-1}$ of hydrogen as reducing agent. The reactions were executed for approximately 164 minutes until the full oxygen carrier reduction was achieved. The oxidations were performed at 750 °C by supplying 0.03 $g \cdot min^{-1}$ of water. The water was evaporated within the hotbox and fed into the tube reactor. The evaporation and the release of hydrogen by oxidizing the iron led to a system pressure increase. During the pressure increase the outlet mass flow controller of the system was slightly opened to ensure a continuous gas flow through the system. The hydrogen gas flow was analyzed by two mass flow controllers (MFC) connected in series. The first MFC functioned as a throttle valve to reduce the outlet gas flow or completely close the system. It also reduced the gas flow to an atmospheric pressure for the second MFC, which was required for correct and reproducible flow measurements. The second mass flow controller was fully opened and measured the actual gas independently of the system pressure.

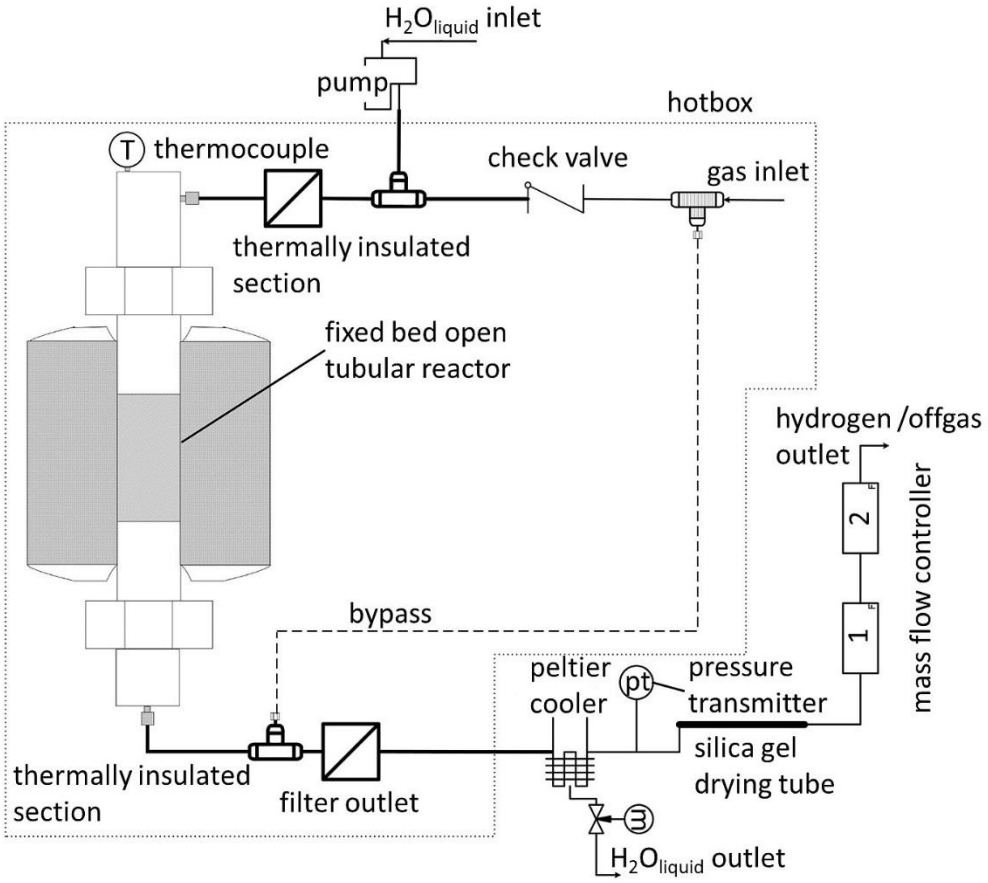

Figure 32: Experimental setup for high pressure hydrogen production.

4.2.2 Oxygen carrier sample

Oxygen carrier samples were prepared by the mechanical mixing technique, which has been described in chapter 3. Oxygen carrier samples with diameters between 90 – 120 µm were used for the experiments.

The oxygen carrier surface morphology after the pressurized cycling experiments was analyzed with scanning electron microscopy technology (Zeiss Ultra 55, acceleration voltage 15 kV) and compared to unpressurized and fresh samples.

4.3 Results

4.3.1 High pressure hydrogen production

Two exemplary reduction results with pure hydrogen at atmospheric pressure and 750 °C are presented in figure 33. The hydrogen conversion (**H_{2conv}**) is defined by equation 11. **H_{2in}** represents the hydrogen feed of 25 Nml·min^{-1} and **H_{2out}** the unreacted hydrogen flow detected at the system outlet.

$$H_{2conv} = 1 - H_{2out} / H_{2in} \quad (11)$$

The reduction from hematite shows three distinctive parts. The first part starts at minute 0 and ends at around minute 11 in figure 33, left. This first peak with the highest hydrogen conversion represents the reduction of Fe_2O_3 to Fe_3O_4. The second stage, which ends at minute 30, represents the reduction of Fe_3O_4 to FeO. The final step illustrates the conversion of FeO to Fe. After this stage the hydrogen conversion efficiency decreases significantly, which indicates the end of the reduction reaction and complete conversion of FeO to Fe. All consecutive reductions were conducted between magnetite and iron due to thermodynamic restrictions of the process (figure 33, right). The reduction reactions were performed until a full oxygen carrier conversion was achieved. This resulted in an increasing reduction reaction per each cycle caused by the reduced kinetics, which is induced by thermal sintering.

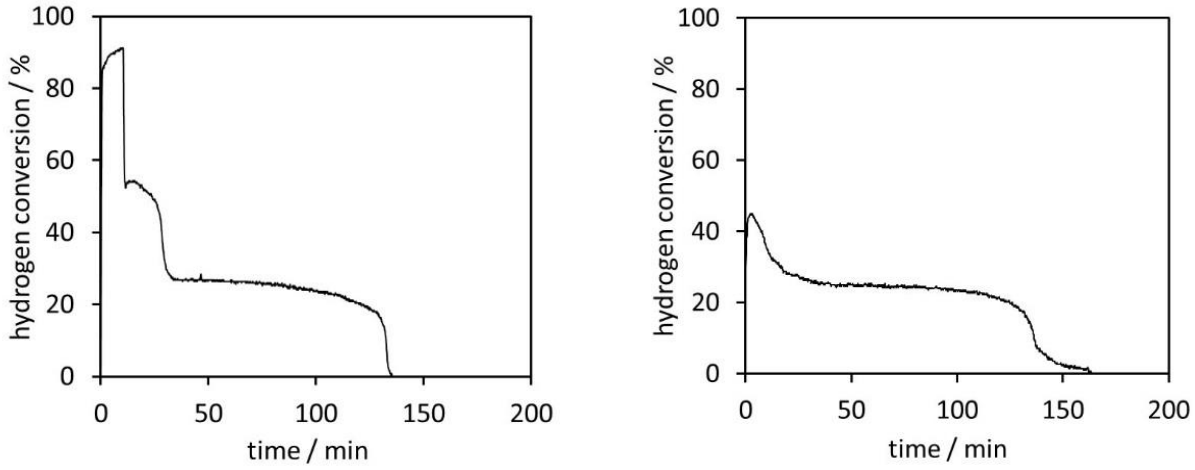

Figure 33: Left: First reduction reaction of the reactor filling from hematite to iron, right: representative reduction from magnetite to iron, which corresponds to reduction 14 in table 3. The reductions were performed with 25 Nml·min^{-1} pure hydrogen at ambient pressure and 750 °C.

The oxidations executed at different pressure levels are illustrated in figure 34 and figure 35. The reaction starts with the pressure increase. During this stage the gas outlet MFC is slightly opened to allow a continuous flow of the reaction gases through the system. At this step the hydrogen conversion rate is higher than 10 Nml·min^{-1} (cycles 2 – 4) respectively higher than 5 Nml·min^{-1} (cycles 5 – 15). This is indicated by a system pressure build-up despite the adjusted hydrogen gas outlet flow. As a representative oxidation, number 9 can be described as followed. After approximately 44 minutes the system reaches its maximum pressure, indicated by a stable pressure signal until minute 69. At minute 50 the outlet mass flow controller is opened to a volume flow of 10 Nml·min^{-1} to decrease the reaction time. The oxidations 2 – 5 were executed with a different volume flow setting. The hydrogen outlet flow was kept at a constant flow of 10 Nml·min^{-1}. Oxidation 1 was used for evaluation of different system settings and is presented here for the sake of completeness of the research. All oxidations were performed until the hydrogen outlet flow dropped to zero, which indicated the complete oxidation of the oxygen carrier. The maximum pressure achieved in the oxidation reaction is determined by the temperature of the steam inlet system, which is also used as the steam generator. The pumping of liquid water into the system and its evaporation causes the pressure increase in the system. In the reactor the steam reacts to hydrogen. Any unreacted steam is condensed in the peltier-cooler at the gas outlet. Due to the constant volume of the system the measured pressure can be directly related to the amount of produced hydrogen. The elevated system pressure, which also implies an increased water vapor pressure, requires a higher temperature at the steam inlet to evaporate the water. Equilibrium between steam and condensed water is maintained at the adjusted inlet temperature, which limits the maximum system pressure. Finally, a pressure decrease is observed. Hydrogen conversion ceases due to the full oxidation of the contact mass. The system pressure falls until atmospheric pressure is reached, which signals the end of the reaction.

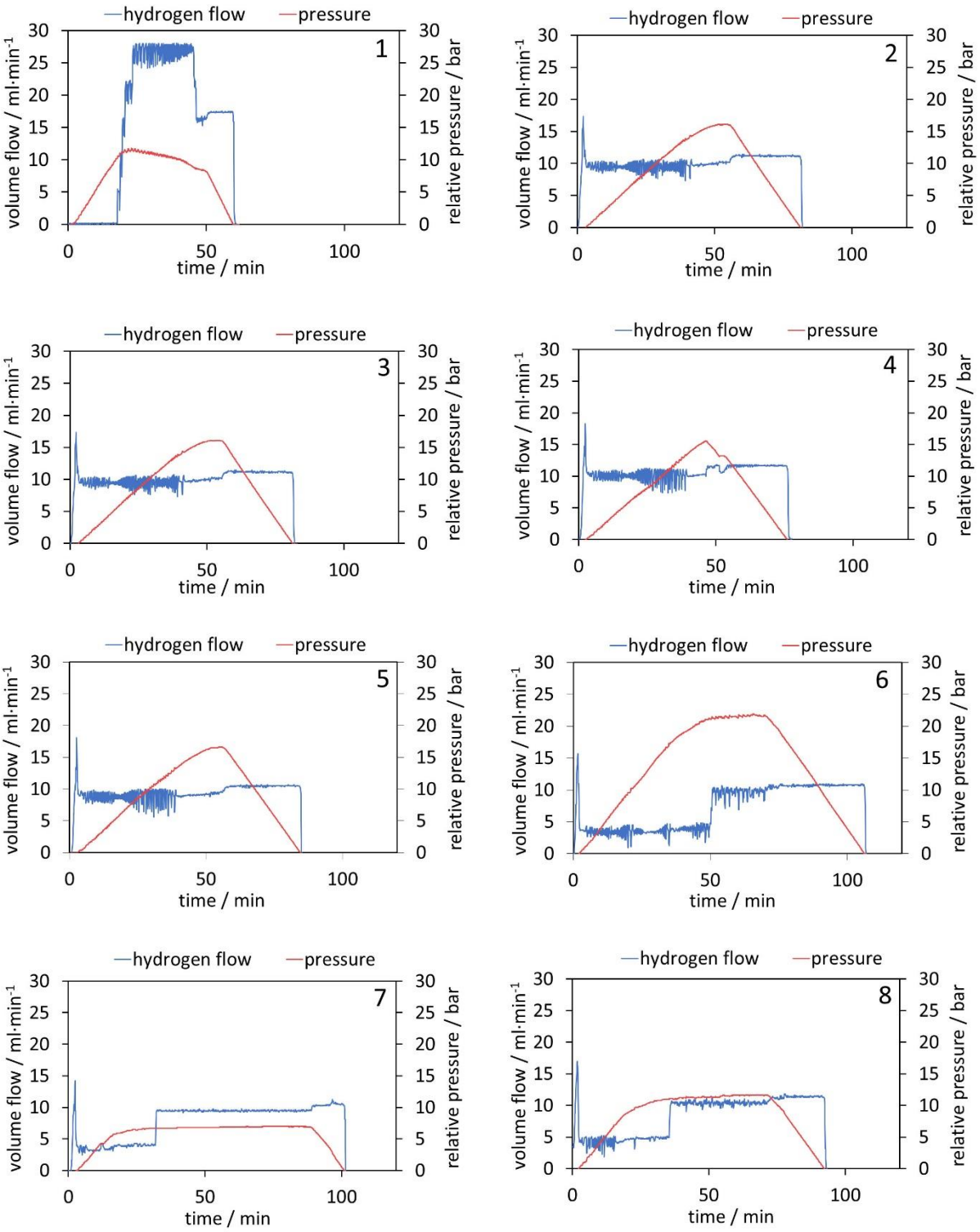

Figure 34: Hydrogen volume flow and the system pressure of the oxidations 1 – 8.

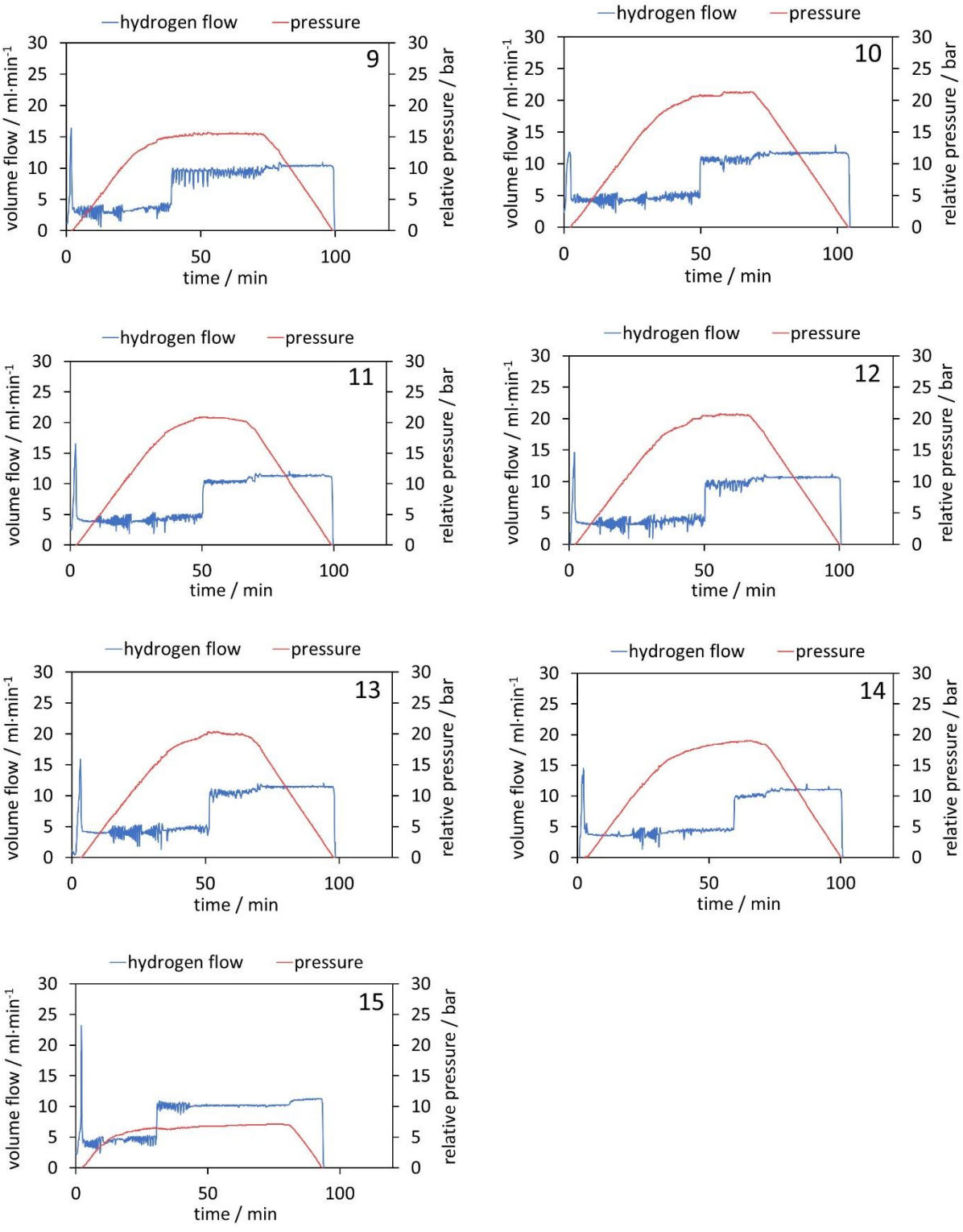

Figure 35: Hydrogen volume flow and the system pressure of the oxidations 9 – 15.

The amount of consumed or produced hydrogen is calculated from the gas flow measured by a mass flow controller at the system outlet. The hydrogen quantity is correlated to the mass of converted iron/iron oxide. The oxygen carrier conversion $\mathbf{OC_{con}}$ can then be defined by equation 12.

$$OC_{con} = 4/3 \cdot \Sigma n_{H2} / n_{Fe} \quad (12)$$

$\mathbf{n_{H2}}$ in mol represents the consumed or produced hydrogen and $\mathbf{n_{Fe}}$ in mol represents the elemental iron in the oxygen carrier. The results are presented table 3. The oxygen carrier conversion results are consistent throughout the whole reduction and oxidation experiments. The differences between reduction and oxidation OC_{con} lie within the error of measurement. The elevated system pressure which causes fluctuation in the steam volume flow is the main source for these errors. The fluctuations in the water volume flow (caused by the piston pump system) and unsteady evaporation induce small pressure impulses in the test system, which significantly influences the stability and reliability of the mass flow controller used for analysis purposes. This effect can be identified in the volume flows instabilities. The MFC measurement errors are proportional to the system pressure, which can be recognized by comparing experiments at lower pressure levels to higher pressure oxidations. To reduce the influence of the pressure pulses on the mass flow measurements a serial construction of two MFCs was installed. The first MFC was used to regulate the outlet gas flow and functioned as a pressure reducer. The second was fully opened and operated as a mass flow meter. Prior to the pressure research, experiments were conducted to evaluate the improvement compared to the single MFC layout. These results showed that the two serial construction was vital to operate the test rig under pressurized conditions.

The analysis of the reduction reactions results (table 3) shows a decrease of consumed hydrogen from 20 $mmol \cdot g_{Fe}^{-1}$ to 18 $mmol \cdot g_{Fe}^{-1}$, which corresponds to a mean decrease of 0.8% between each cycle. These capacity losses of the oxygen carrier are caused by thermal sintering of the iron and are in good accordance with previously performed measurements at ambient pressure.[55] During the reduction 13, a connection error between the test rig and the data logging occurred, which resulted in a loss of the experimental data. Hence, the H_2 conversion is not calculated for this cycle.

The H_2 conversion results presented in table 3 regarding the moles of consumed hydrogen in the reductions and the moles of hydrogen produced in the subsequent oxidations indicate the closing of the material balance within each cycle. To do this the mass flux of the steam at the reactor outlet was mathematically taken into account. This procedure is valid for the two-component system of H_2/H_2O. The possibility of an overlooked mass flux can be ruled out in this case.

Table 3: Experimental results of the performed 15 cycles.

reaction	maximum rel. pressure bar(g)	H_2 conversion (input/output) mmol	H_2 per mass Fe (input/output) mmol·g_{Fe}^{-1}	oxygen carrier conversion %
1. reduction		45	20	84
1. oxidation	12	44	19	82
2. reduction		45	20	83
2. oxidation	16	41	18	77
3. reduction		45	20	83
3. oxidation	16	39	17	72
4. reduction		45	20	83
4. oxidation	17	43	19	80
5. reduction		44	19	82
5. oxidation	22	42	19	79
6. reduction		44	19	81
6. oxidation	7	44	19	81
7. reduction		43	19	81
7. oxidation	12	39	17	72
8. reduction		43	19	80
8. oxidation	16	42	18	77
9. reduction		43	19	79
9. oxidation	21	41	18	77
10. reduction		42	19	79
10. oxidation	21	39	17	72
11. reduction		42	19	79
11. oxidation	21	39	17	73
12. reduction		43	19	80
12. oxidation	20	38	17	70
13. reduction		-	-	-
13. oxidation	19	-	-	-
14. reduction		40	18	75
14. oxidation	7	41	18	76
15. reduction		40	18	74
15. oxidation	7	42	19	78

In order to investigate influences of the oxidations at elevated pressures on the redox reactions the oxygen carrier conversion is analyzed as a function of the maximum pressure. figure 36 (left) depicts the conversion during the reduction reaction, which indicates a consistent decrease caused by sintering effects. The oxidation OC conversion (figure 36, right) shows a similar result: a stable descend with no dependency on the maximum pressure. The oxidations include a greater deviation than the reductions caused by the measurement errors of the MFC, which is significantly higher when operated under quickly changing pressure conditions. The OC conversion of both the reductions and the oxidations shows no spikes (figure 37), which clearly suggests that the process is not influenced by an elevated pressure and can be efficiently used for the decentralized production of pure pressurized hydrogen.

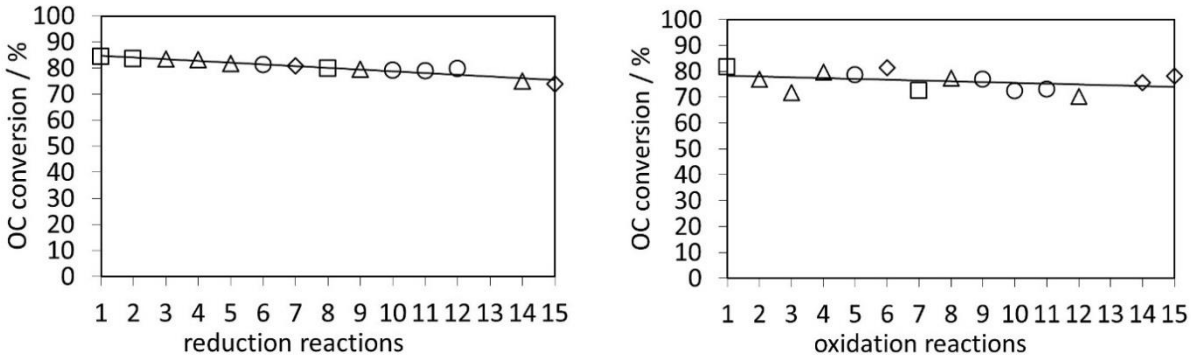

Figure 36: Left: oxygen carrier conversion of the reduction reactions. Right: oxygen carrier conversion of the oxidation reactions. The different markers indicate the maximum pressure during the oxidations (previous oxidations in the left figure), check: < 10 bar, square: 10 – 15 bar, triangle: 16 – 20 bar, circle: > 20 bar.

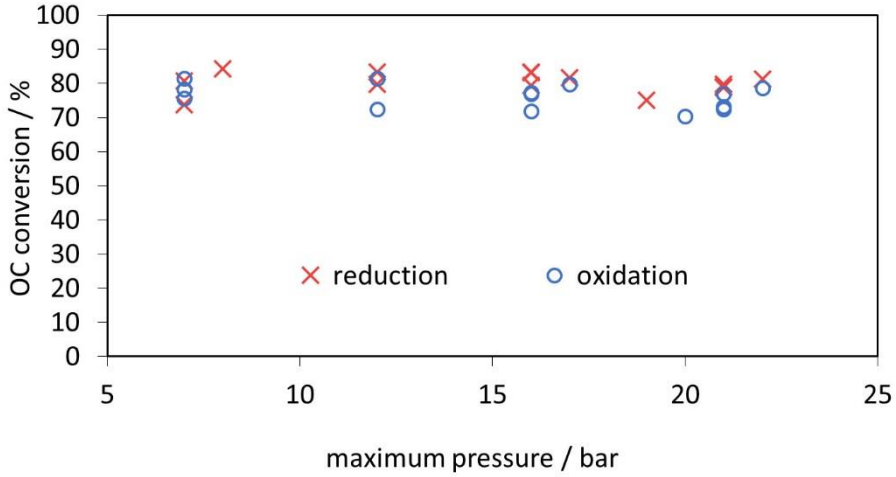

Figure 37: Oxygen carrier conversion of the reductions and oxidations against its maximum pressure and the maximum pressure of the prior oxidation.

The linear pressure increase in the first part of each oxidation reaction is directly related to the hydrogen production rate. Within this period the highest oxygen carrier conversion of each cycle is achieved. The slopes of these pressure rises are determined and compared to each other. Figure 38 shows the comparison of the pressure ascents of oxidations performed with the same test conditions. The linear slope results are in a very good accordance with each other and stay steady throughout the whole research. This indicates that the oxidation reaction rate with steam is not influenced by the system operated at elevated pressures.

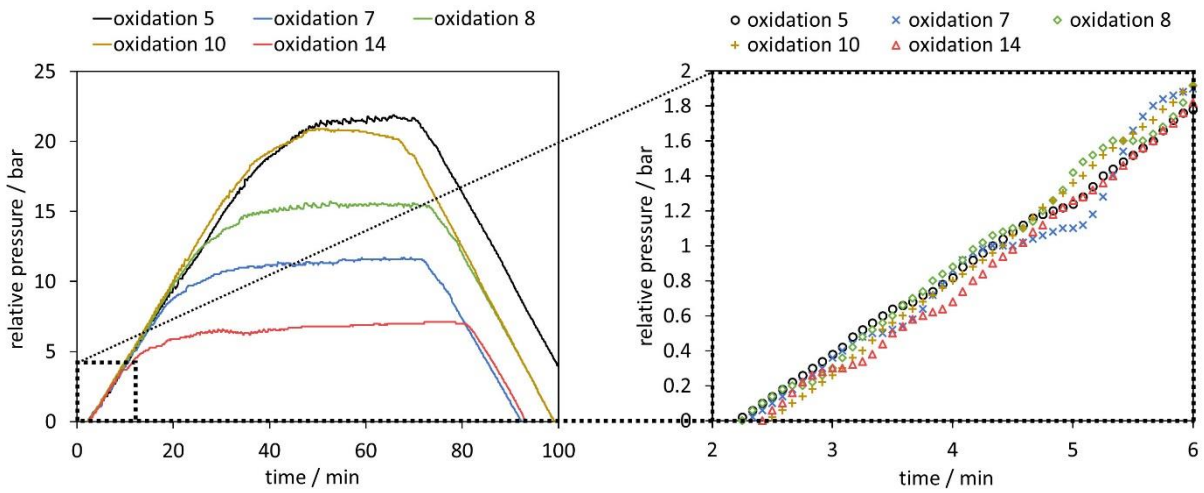

Figure 38: Left: pressure characteristics of the oxidations, which were performed with same test conditions at different pressure levels. Right: the magnified linear pressure increase.

4.3.2 Scanning electron microscopy

The results of the oxygen carrier surface analysis are presented in figure 39. Images (a) and magnified (d) show the oxygen carrier which was used in the presented experiments for the production of compressed hydrogen. As comparison: images (b) and magnified (e) show a sample, which was used in reduction/oxidation experiments (8 cycles) at ambient pressure performed in a thermogravimetric analysis system. Images (c) and magnified (f) show a fresh sample. A clear difference in the grain size of the 3 samples can be identified. The fresh oxygen carrier does have the smallest particle sizes followed by the pressurized sample. All three samples have a rough surface with a sufficient level of porosity to allow the reaction gases to reach its interior. The highest magnification of the structures shows tight packed regions within the pressurized sample (image d) with reduced porosity. The TGA sample on the other hand has a distinctive skeletal structure, with good dispersion of microspores. This structural degradation clearly clarifies the decreasing oxygen carrier conversion, which was measured with each cycle. The reduced porosity can be clearly explained by thermal sintering of the oxygen carrier. The pressurized sample was used in significant more cycling experiments and each cycle took a multiple longer than the unpressurized TGA sample. This long-term thermal load caused the structural degradation, which is indicated by smoothed surfaces and reduced porosity. Besides this no evident negative effect which can be related to the high pressure stress is visible and the sample maintained its structural integrity.

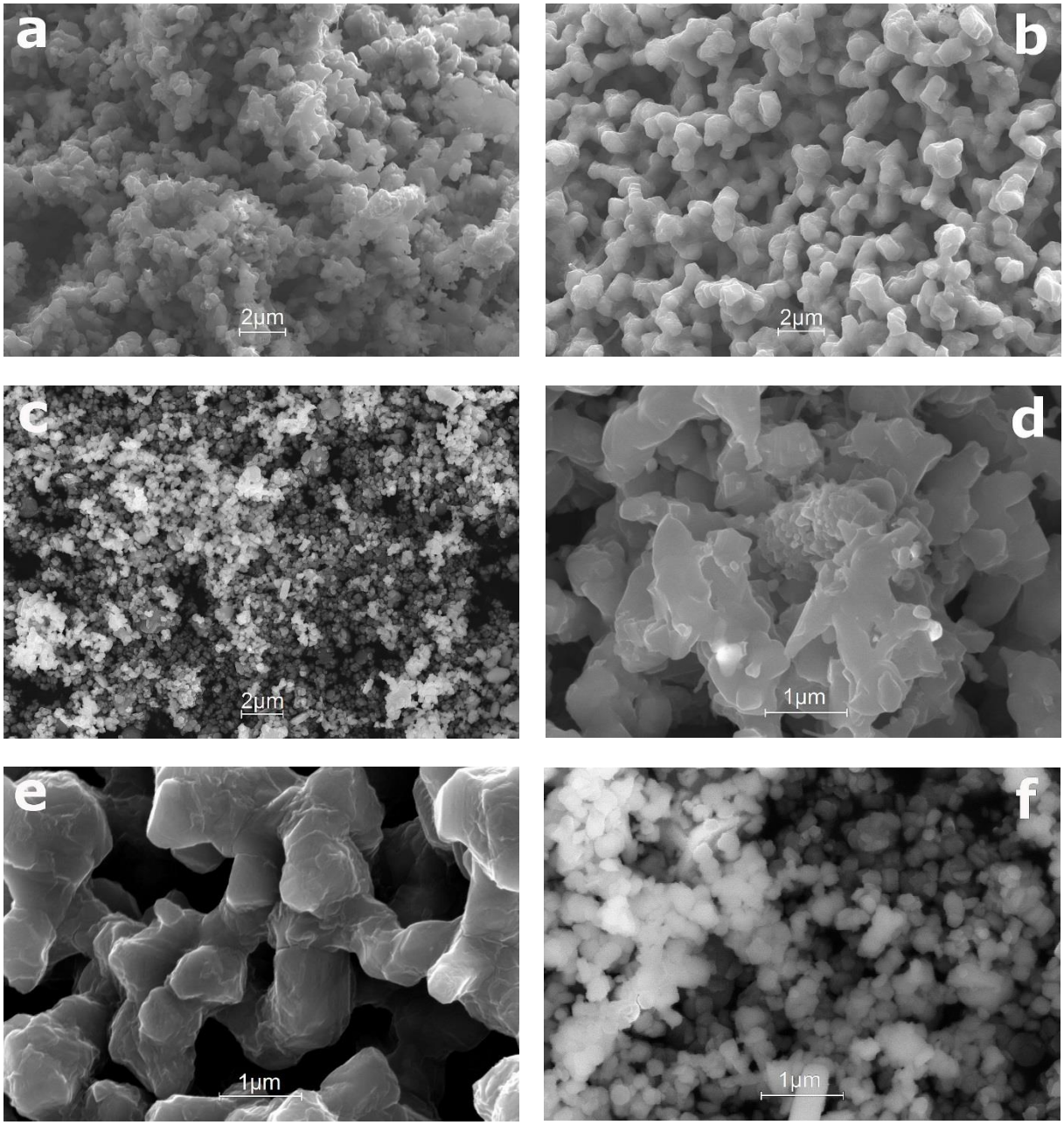

Figure 39: SEM images of the oxygen carrier samples (90 wt% Fe_2O_3, 10 wt% Al_2O_3, 90 – 125 µm), after several pressurized oxidations (a) and after 8 oxidations at ambient pressure in a thermogravimetric analysis system (b). (c) shows an image of the fresh oxygen carrier sample. Magnified SEM images of the pressurized sample (d), the sample used in a thermogravimetric analysis system (e) and the reference sample (f).

4.4 Conclusion

Pressurized hydrogen production experiments based on the steam iron process were performed in a lab scale test rig. The focus of the experiments was on the oxidation at elevated pressure. The main goal was to identify effects of the elevated system pressure on the oxygen carrier conversion of the cyclic reductions and oxidations. 15 cycles were performed, which yielded hydrogen of up to 22 bar(g). The experiments were performed as a sequence of oxidations at high pressure levels (≥ 20 bar) and at lower pressure levels (< 20 bar). Each oxidation was followed by a reduction at ambient pressure until full reduction was achieved. In this way the influence of an elevated hydrogen pressure on the following cycles (oxidation and reduction) can be efficiently identified. A stepwise and steady pressure increase between cycles is also suitable to reveal a performance decrease caused by the pressure but the effects might be concealed by the steady degradation of the oxygen carrier, which is caused by thermal sintering. The oxygen carrier conversion of the reductions, the pressure increase of the oxidations and the structural properties of the sample were analyzed. The oxygen carrier conversion decreased from 84% to 74% over the 15 cycles. The decrease was at a steady level with no evident impact of the different pressure conditions in the prior oxidations. The linear pressure increase in the first part of each oxidation maintained at a stable level throughout the entire investigation. The analysis of the surface morphology revealed structural degradation by thermal sintering, which resulted in a reduced porosity but the overall structural integrity was preserved.

The results show that the stability of the oxygen carrier is reduced by sintering effects which are mainly induced by the high reaction temperatures of 750 °C. The elevated pressure was not identified as a source for reduced conversion efficiency of the steam iron process within the performed cycles. This proofs the principal suitability of the steam iron process for the production of compressed hydrogen without additional gas compression. To verify a long term pressure stability of the oxygen carrier an increased cycle number with different pressure steps is recommended.

5 High purity pressurized hydrogen production from syngas by the steam-iron process

5.1 Introduction

In the previous chapter the feasibility of pressurized oxidation up to 22 bar without any negative impact on the conversion efficiency of the reduction and oxidation reactions and on the mechanical stability of the oxygen carrier, with hydrogen as the only reducing component, was presented.[158] The consecutive work, discussed in this chapter, focused on the reduction of an iron based oxygen carrier with a synthesis gas at ambient pressure, followed by an oxidation at different elevated pressures of up to 50 bar. The aim of the experiments was to study

- influences of an increased system pressure on the hydrogen purity regarding carbon contamination
- the characterization and quantification of the contaminations
- the analysis of the oxygen carrier conversion regarding efficiency and stability
- the verification of the feasibility of the process at further elevated oxidation pressure up to 50 bar.

The essential parts of this chapter were published in the journal of RSC Advances 2016, **6**, 53533-53541, under the title *High purity pressurised hydrogen production from syngas by the steam-iron process*, by Gernot Voitic, Stephan Nestl, Karin Malli, Julian Wagner, Brigitte Bitschnau, Franz-Andreas Mautner and Viktor Hacker.[54] The calculations of the reaction dimensions for higher system pressures were executed by Martin Ziegler and presented in his bachelor's thesis.[207]

5.2 Experimental

5.2.1 Pressure test equipment

The cyclic experiments were performed in a modified test rig for catalytic analysis (figure 40). The main component is a fixed bed tubular reactor (alloy 617, OD 25.4 mm, ID 15.26 mm, length 350 mm), which can withstand a maximum pressure of 100 bar at temperatures of up to 1123 K.

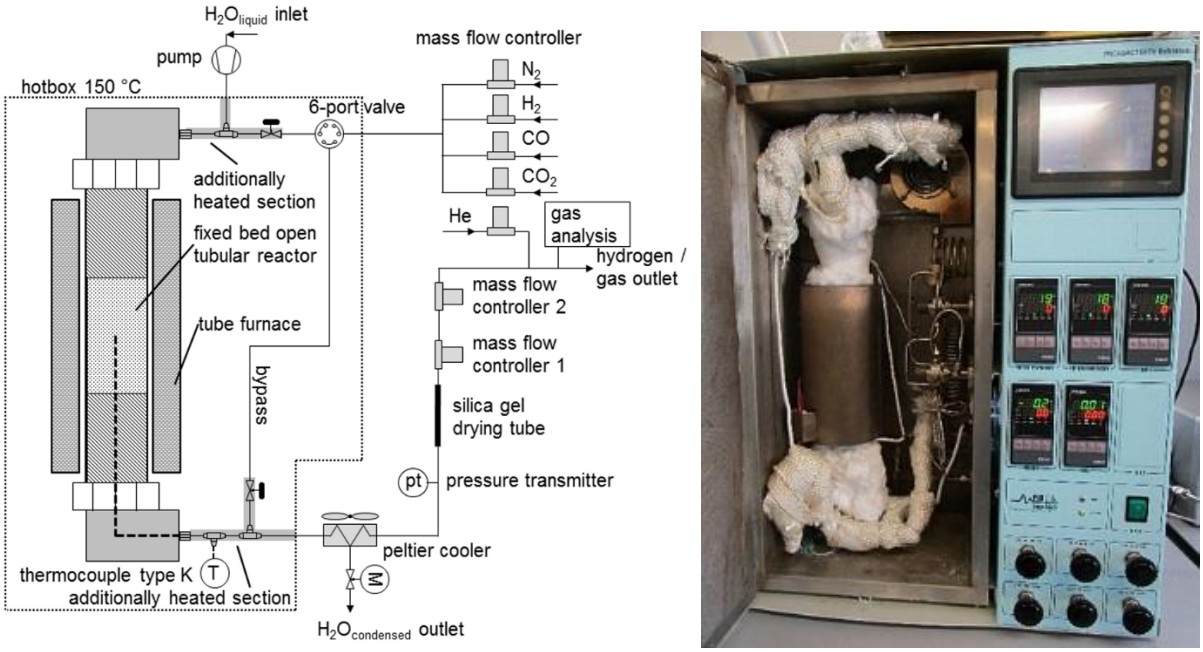

Figure 40: Left: schematic process diagram of the experimental test rig for high pressure hydrogen production out of a synthesis gas mixture. Right: a photo of the modified test rig.

Prior to the cycle experiments a new reactor design was planned to ensure a safe and stable operation at higher system pressures. The defined system requirements were a maximum reactor temperature of 850 °C and a maximum pressure of 100 bar of hydrogen. Under these conditions high grade steel materials, which are usually used, are not fit for this application. Hence, a nickel-chromium-cobalt-molybdenum alloy Nicrofer® 5520 Co, alloy 617, with the chemical composition presented in table 4, was selected as reactor material. This material has an exceptionally strength and oxidation resistance at high temperatures and against corrosion and is used in gas turbines and petro chemical industries. The favored material characteristics are achieved by precipitation hardening at temperatures up to 1150 °C. Seamless tubes of alloy 617 in the selected dimensions were not available. The two possible options, to manufacture the reactor, were (i) a tube bended and welded from a metal sheet and (ii) the drilling of a rod. The latter was chosen. An alloy 617 rod (diameter = 25.4 mm) was purchased from Bibus Metals AG and cut into pieces of 400 mm and drilled through by HSM Stahl und Metallhandel GmbH (figure 41).

Table 4: Chemical composition of Nicrofer 5520 Co, alloy 617 according to Bibus metals supplier.

	Ni %	Cr %	Fe %	C %	Mn %	Si %	Co %	Cu %	Mo %	Ti %	Al %	S %	B %
minimum	44.5	20.0	-	0.05	-	-	10.0	-	8.0	-	0.8	-	-
maximum	-	24.0	3.0	0.15	1.0	1.0	15.0	0.5	10.0	0.6	1.5	0.015	0.006

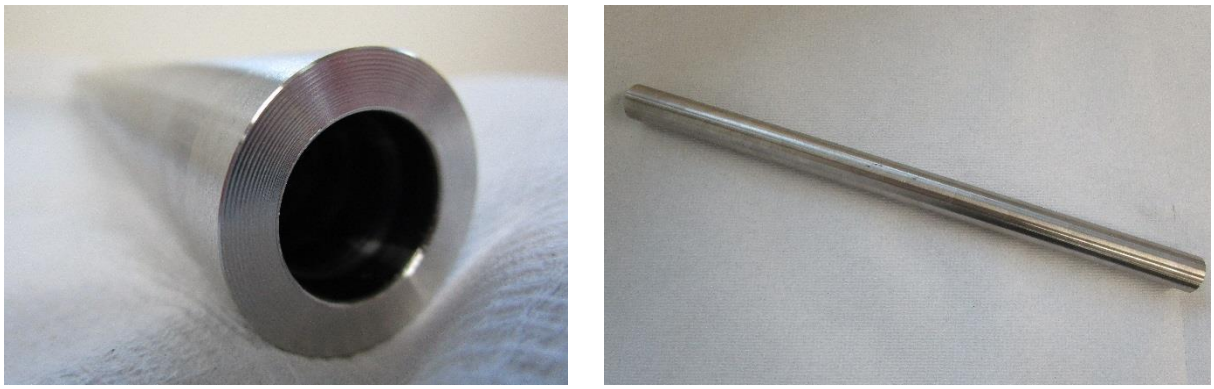

Figure 41: Photos of the Nicrofer 5520 Co, alloy 617 high pressure reactor tube.

The design calculations regarding the wall thickness for high pressure and high temperature operations were executed according to the German standard AD 2000 for pressure equipment with the datasheets B0 and B1.[207–209]

Calculations were performed according to equation 13, which is valid for tubes with $D_a \leq 200$ mm and a ratio of $D_a/D_i < 1.7$:

$$w = \frac{D_a \cdot p}{20 \cdot \frac{K}{S} \cdot v + p} + c_1 + c_2 \quad (13)$$

The variable **w** represents the required wall thickness, $\mathbf{D_a}$ the outer reactor diameter with 25.4 mm (≙ 1''), **p** the maximum operation pressure, which was specified as 100 bar. **K** the material characteristic strength value, **S** the safety factor, **v** the coefficient for welded seams, $\mathbf{c_1}$ the safety margin for short falling of the wall thickness and $\mathbf{c_2}$ a safety margin for abrasion. The value for the material characteristics strength was based on the rupture strength data for 10,000 hours from the VDM metal data specification.[210] The reactor outside wall temperature was limited to 900 °C, thus $K = R_{m/10^4h} = 30\ N \cdot mm^{-2}$ (figure 42). As the safety factor S a value of 1.5 was incorporated, which relates to standards for rolled and forged stainless steel. Safety

margins for welding joints and deviations in the wall thickness were not integrated in the calculations and v was defined as 1. Hence the calculated value for the required wall thickness is w = 5.08 mm, which is in good accordance with the final reactor design of OD = 25.4 mm, ID = 15.26 mm.

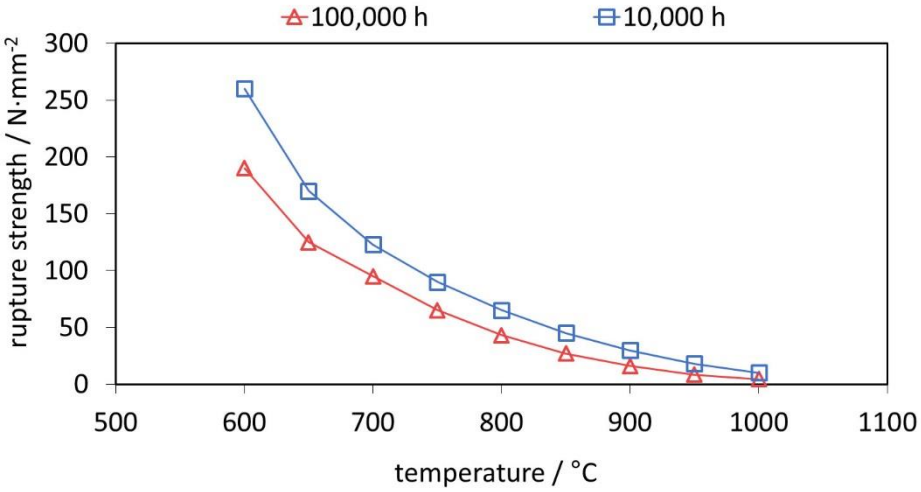

Figure 42: Rupture strength of Nicrofer 5520 Co, alloy 617 according to operation temperatures and lifetime.[210]

5.2.2 Oxygen carrier samples

An oxygen carrier sample with a composition of 90 wt% Fe_2O_3, 5 wt% Al_2O_3 and 5 wt% CeO_2 was prepared by a continuous co-precipitation synthesis based on the method of Kidambi et al.[102] Particles with a grain diameter of 90 – 125 µm were calcinated at 1173 K for 3 hours. 7.00 g were used in the cyclic experiments. CeO_2 was added to the oxygen carrier unlike to samples used in our previous work[158] because of its positive effects on the activity and stability in a synthesis gas atmosphere.[211]

Elemental analysis was performed after a microwave-assisted pressurized acid digestion by inductively coupled plasma atomic emission spectroscopy ICP-OES (Spectro Arcos SOP).

The surface of the oxygen carrier was analyzed by scanning electron microscopy SEM (Zeiss Ultra 55, acceleration voltage 15 kV). Images of the fresh oxygen carrier and after the experimental test series were taken.

X-ray powder diffraction data were obtained on a Bruker AXS D8 Advance powder diffractometer in Bragg-Brentano geometry with LynxEye Detector, operated at 40 kV and 40 mA, using Cu Kα radiation (λ = 1.54178 Å). Diffraction angles were measured from 15 – 105° 2θ, having a step size of 0.025° 2θ, 5 s per step.

5.2.3 Operation procedures

The reactor was filled with the oxygen carrier. A thermocouple was placed inside the oxygen carrier bed. Both reactor ends were packed with inert materials to preheat the reaction gases and to prevent movement inside the reactor. The steam-carrying parts of the system were heated with heating-cords to 573 K to prevent steam condensation at higher system pressure. At the system outlet, steam was removed with a peltier-cooler by condensation. The reaction gases left the system through 2 MFCs (mass flow controller) in serial connection. In the oxidation pressure experiments the first MFC was used as a throttle valve to close the system or to limit the outlet gas flow. The produced hydrogen left the first MFC at an atmospheric pressure and the gas flow was analyzed in the second MFC, which was fully opened. This guaranteed stable and reproducible pressure conditions independently of the actual system pressure, which was a critical requirement to analyze the hydrogen flow with a MFC. The hydrogen purity was subsequently investigated with a gas chromatograph (MicroGC 3000 Inficon) at the system outlet. During the reduction experiments both MFCs were fully opened. The changing gas composition during the reduction was analyzed by the MicroGC at the system outlet. The MicroGC is equipped with a molecular sieve 5A and a PoraPLOT U and 2 thermal conductivity detectors. During the reduction and air-oxidation an analysis method to identify components (H_2, CO, CO_2 and O_2) in the %-range was used. The hydrogen impurities CO and CO_2 during the oxidation experiments were analyzed with a high sensitive detection method in the ppm concentration range, while H_2 was analyzed separately using the MFC2.

Reduction reactions were performed at 1023 K using a gas mixture of H_2, CO, CO_2 (He was added as an external standard). The reductions were performed for 90 respectively 210 minutes. Each reduction was concluded by a nitrogen purge step with 150 $ml \cdot min^{-1}$ for 30 minutes respectively several hours including a cooling-down phase. Each reduction was followed by an oxidation at elevated pressure (or at ambient pressure as reference) by introducing 0.06 $g \cdot min^{-1}$ of water for approximately 60 minutes with a HPLC pump. The water was evaporated in the heated tubes before entering the reactor. Each cyclic experiment with a reduction length of 210 minutes was concluded by an air oxidation to completely remove solid carbon from the oxygen carrier.

5.3 Results and discussion

5.3.1 Composition analysis of the fresh oxygen carrier sample

The elemental analysis results of the used sample and the calculated share of the metal oxides (under the assumption of completely oxidized state) are presented in table 5.

Table 5: Elemental analysis results and the calculated metal oxide composition.

Al wt%	Ce wt%	Fe wt%	Al_2O_3 wt%	CeO_2 wt%	Fe_2O_3 wt%
2.59	3.79	61.29	5.04	4.79	90.17

5.3.2 Reduction reactions with synthesis gas

The reductions of the oxygen carrier were performed at 1023 K with a dry synthesis gas mixture of H_2 54.5 vol%, CO 34.0 vol% and CO_2 11.5 vol% and a total gas flow of 90 ml·min^{-1}. The reduction was performed for 90 minutes followed by a 30 minutes sweeping phase with nitrogen (150 ml·min^{-1}) and a steam-oxidation (0.06 g·min^{-1} of water) at elevated pressure.

The changes of gas flow characteristics with increasing cycle numbers are presented in figure 43, left. Two noticeable reductions stages are visible within each cycle. Between minutes 20 – 40 the reduction of magnetite to wustite and between minutes 70 – 90 the reduction of wustite to iron take place.[83,194,212] The two quasi stable stages are separated by a transition phase at around minute 60.

At the end, the reduction of wustite to iron is happening with a low conversion of the synthesis gases. The parallel occurring water gas shift reaction dominates and defines the outlet gas composition, which is in good accordance with equilibrium calculations from HSC Chemistry at this stage of the process.

The reductions were manually stopped after 90 minutes to guarantee reproducible conditions for each of the consecutive oxidations and to investigate the decrease of the oxygen carrier conversion. The shifting of the transition phases to an earlier reaction time (hydrogen flow from minute 60 to minute 50) indicates the degradation of the oxygen carrier and a loss of reactive surface.[67] The reaction temperature of 1023 K leads to sintering of the solid, which reduces the porosity and the active volume of the pellets. Consequently, less magnetite is able to react with the synthesis gas.[67] Another explanation for the degradation of the contact mass is the formation and accumulation of $FeAl_2O_4$. Studies have reported that $FeAl_2O_4$ is formed in the presence of Al_2O_3 if the iron based oxygen carrier is reduced beyond Fe_3O_4, which lowers the hydrogen yield, thus leading to a decreased oxygen carrier conversion.[102,106] The third possible explanation is the formation of carbon on the oxygen carrier, which is not fully removed by the steam oxidations. This leads to accumulation of carbon and plating of the iron surface.[153,156] The oxygen carrier conversion (figure 43, right), which expresses the exchanged

oxygen atoms within the solid, shows a strong drop within the first two reductions and slow linear decrease afterwards. After the first 11 cycles, a different test series, discussed in 5.3.4, which included longer reductions and full oxidations to hematite with oxygen were executed. The reductions performed after that (number 27 to 31) display a slightly higher conversion than expected following the linear decrease within the first reduction set. This indicates a regeneration effect of the oxygen carrier by the complete air oxidations. This effect has also been reported by literature studies.[55,213]

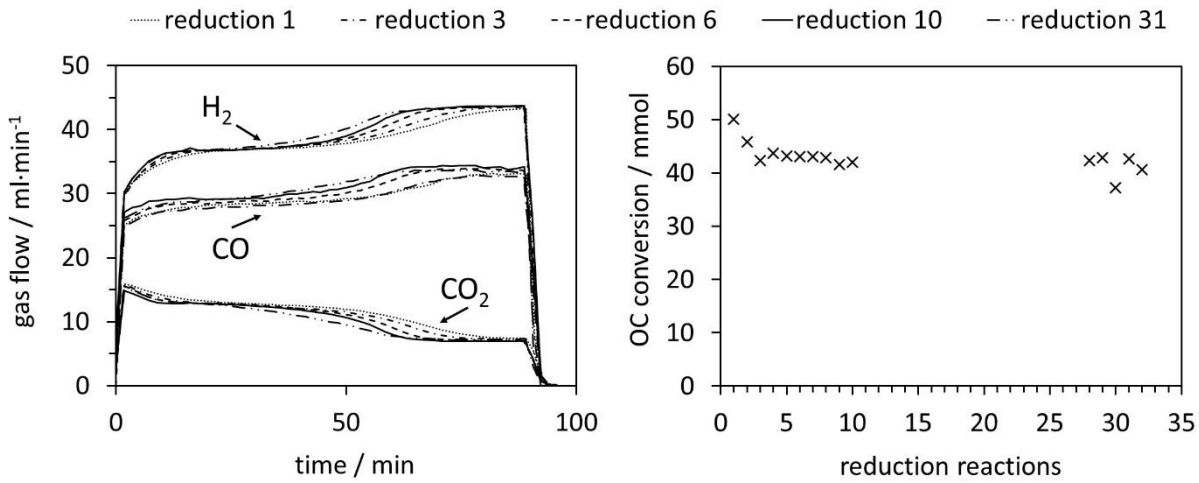

Figure 43: Left: gas flow characteristics of 5 representative reductions. Right: oxygen carrier conversion of reduction reactions performed with synthesis gas for 90 minutes at 1023 K. Reductions 1 – 11 were followed by a steam-oxidation, reductions 27 – 31 were followed by a steam-oxidation and an air-oxidation. Reductions 12 – 26 are discussed in section 5.3.4. Experiments 12 – 15 and 21 – 26 were used to vary process parameters and thus excluded from the assessment.

5.3.3 Pressurized oxidations – hydrogen purity

After each reduction an oxidation at elevated pressure (oxidation at ambient pressure as reference) was performed. The hydrogen flow was measured with a thermal mass flow controller (MFC 2 in figure 40). The hydrogen purity was analyzed with a gas chromatograph directly behind the system outlet. The two detected impurities were carbon monoxide and carbon dioxide. The hydrogen purity at different pressure levels (0 – 50 bar) and potential correlations were analyzed. Figure 44 shows the pressure profile and the gas flow adjustment of two representative pressurized oxidations.

The oxidation starts with the pressure build-up by pumping water into the system. At this stage the system outlet is completely closed by the MFC 1. This leads to a linear pressure rise in the system. The steam oxidizes the oxygen carrier in the reactor at a temperature of 1023 K by releasing hydrogen. At higher pressure levels the pressure rise slowly decreases, due to the oxygen carrier reaching the fully oxidized state. Unreacted steam is condensed at the system outlet in the peltier-cooler. After the system has reached the predefined pressure the MFC 1

is opened. The amount of produced hydrogen is analyzed by the gas flow measured with the MFC 2.

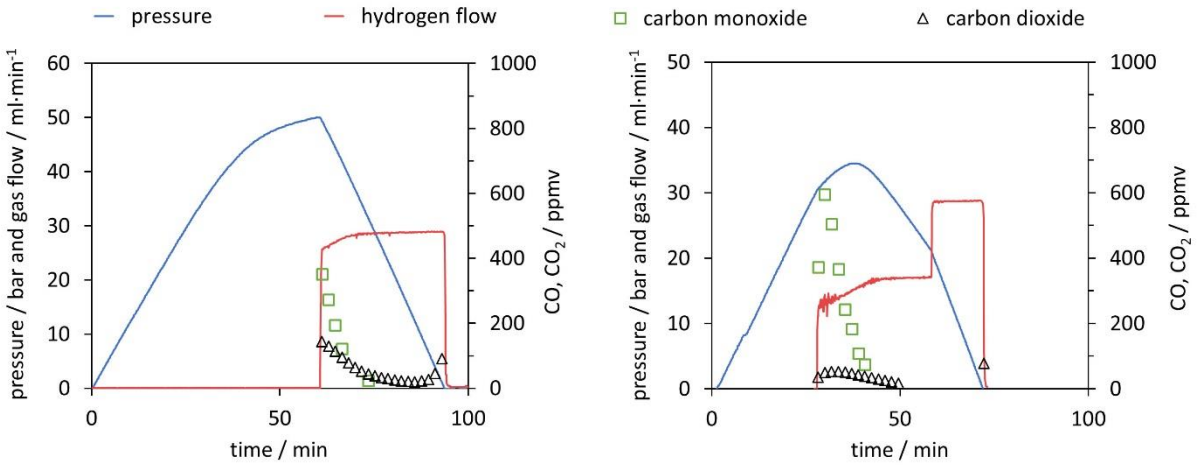

Figure 44: Representative pressure oxidations performed with 0.06 g·min^{-1} of steam at 1023 K. Left corresponds to oxidation 2, right corresponds to oxidation 5 in table 6.

The hydrogen purity measured at the different pressure levels and the amount of carbon monoxide and carbon dioxide are presented in table 6. The hydrogen purity was within the range of 99.958% to 99.999% with a total amount of carbon monoxide in the range of 10 – 245 ppmv.[213] The carbon monoxide characteristic of each oxidation shows a strong peak in the first part of the hydrogen flow measurement of several hundred ppmv and a decrease within 20 minutes below the detection limit of the gas chromatograph (approximately 20 ppmv). The highest initial CO concentration measured was 1633 ppmv (oxidation 4), the lowest 176 ppmv (oxidation 3). The experimental results clearly indicate that the carbon monoxide is immediately produced at the beginning of the oxidation with steam reaching the reactor and cracking solid carbon structures following equation 14.[214] This behavior was also reported by C.R. Müller et al. during the steam oxidation in a fixed bed reactor under ambient pressure and similar experimental setup. They used a CO/CO_2 gas mixture produced by coal gasification for the reduction of the oxygen carrier and the capturing of CO_2.[212]

Table 6: Experimental oxidation results of 16 performed pressure experiments with a reduction length of 90 minutes and 5 experiments with a reduction length of 210 minutes (**bold**). Experiments with purge phases over night, including a cooling down and heating up phase, are underlined. Experiments 12 – 15 and 21 – 26 were used to vary process parameters and thus excluded from the results table.

Reaction	Maximum pressure bar	H_2 amount mmol	H_2 purity %	CO_2 ppmv	CO ppmv
1. oxidation	50	45.9	99.992	7	68
2. oxidation	50	43.9	99.985	104	47
3. oxidation	41	41.6	99.997	20	10
4. oxidation	41	40.0	99.958	171	245
5. oxidation	35	42.2	99.991	19	70
6. oxidation	34	42.0	99.992	48	27
7. oxidation	26	41.8	99.994	8	48
8. oxidation	25	37.1	99.991	34	53
9. oxidation	17	40.2	99.976	107	132
10. oxidation	44	36.5	99.996	0	41
11. oxidation	40	44.9	99.995	5	43
16. oxidation	**50**	**48.9**	**99.946**	**107**	**438**
17. oxidation	**40**	**49.8**	**99.962**	**79**	**305**
18. oxidation	**50**	**49.4**	**99.953**	**82**	**385**
19. oxidation	**32**	**47.6**	**99.941**	**107**	**487**
20. oxidation	**2**	**45.2**	**99.957**	**103**	**328**
27. oxidation	30	39.2	99.999	48	181
28. oxidation	21	37.4	99.984	13	149
29. oxidation	3	36.2	99.980	42	162
30. oxidation	30	37.3	99.982	64	117
31. oxidation	2	36.0	99.987	18	112

The carbon dioxide concentration shows a similar behavior to CO. At the first couple of minutes of the hydrogen flow measurement a higher CO_2 concentration is detected, followed by a decrease, which is probably the result of the water gas shift reaction (WGS) (eq. 15). The initial CO_2 concentration is significantly lower than expected from thermodynamic calculations. A possible explanation is that the high amount of hydrogen, due to high conversion of steam in the presence of Fe, and the high reaction temperatures favor the left side of the WGS equilibrium, thus a high CO/CO_2 ratio.[55]

$$C(s) + H_2O \rightarrow CO + H_2 \quad (14)$$

$$CO + H_2O \rightarrow CO_2 + H_2 \quad (15)$$

The carbon dioxide concentrations contain an additional irregularity. Oxidations with higher concentrations and lower concentrations of CO_2 are alternating in the test series (oxidations 1 – 11). An explanation for this is the duration of the sweeping phase between the reduction and oxidation with nitrogen. The oxidations (1, 3, 5, 7, 10 and 11) with a CO_2 concentration below 20 ppmv were performed after a sweeping phase of several hours over night including a cooling down phase and a heating up phase of the test rig. The results suggest that a significant part of the carbon dioxide is entrapped inside the micro pores of the oxygen carrier particles. The extended purge phase with nitrogen and possibly structural changes in the oxidation carrier by the cooling down phase completely remove CO_2 residues, thus decrease the overall CO_2 concentration.

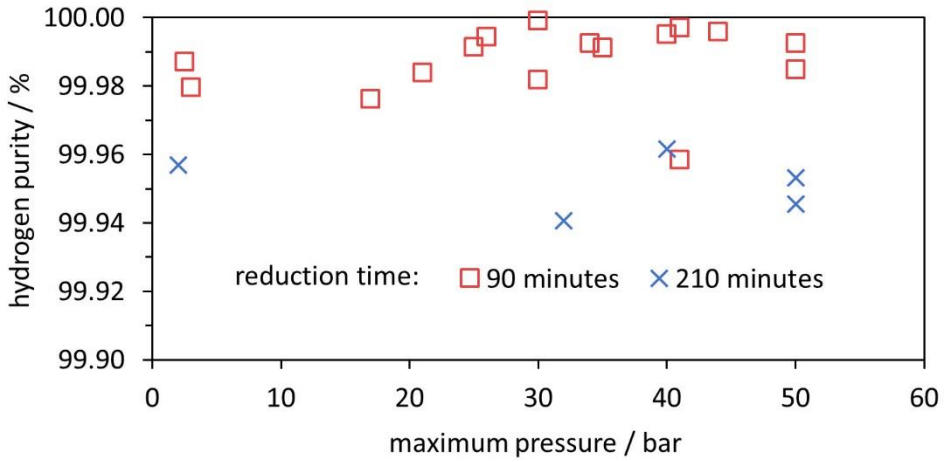

Figure 45: Hydrogen purity as a function of the maximum oxidation pressure. ☐ corresponds to results of the first test series with a reduction time of 90 minutes. x corresponds to results of the second test series with a reduction time of 210 minutes.

Analyzing the hydrogen purity in figure 45, symbol ☐, shows no correlation between the system pressure and the hydrogen purity. This is comprehensible because most of the carbon monoxide is produced in the initial stage of the oxidation where the pressure build up takes place and these conditions are similar in all cycles. This CO oxidation behavior was also found in the experiments at ambient pressure (oxidations 29, 31), which were executed with a minor pressure build-up phase during the oxidation. Thus, the tests clearly revealed that the steam-iron process is suitable to produce pressurized hydrogen out of reducing gas containing carbonaceous products. The increased system pressure shows no impact on the purity of the produced hydrogen.

5.3.4 Experiments with increased carbon deposition

In order to investigate the behavior of carbonaceous contaminations further at an increased system pressure, the reduction time was extended to precipitate a specific amount of solid carbon on the oxygen carrier. The reductions were performed for 210 minutes with the same

reducing gas mixture as before followed by a 30 minutes sweeping phase with nitrogen (150 ml·min^{-1}). The carbon mass balance of the reduction reaction revealed the deposition of 4 – 10 mmol of solid carbon in each reduction. The consecutive oxidations with steam were performed at different pressure levels (50, 40, 30 bars and ambient pressure) under identical conditions as in the prior test series. Each steam oxidation was followed by an air oxidation at ambient pressure (100 ml·min^{-1} for 45 – 60 minutes) to completely remove any solid carbon still left on the oxygen carrier and fully oxidize the oxygen carrier to hematite.

A representative reduction is shown in figure 46, left. The experiment starts with a full conversion of CO and H_2 (minute 7) by the reduction of hematite to magnetite. Two additional steps are recognizable after that, which represent the magnetite to wustite and wustite to iron conversions.

Two representative oxidations are shown in figure 47 and the results of the oxidations are presented in table 6 (oxidations 16 – 20). It is noteworthy that the first carbon monoxide peak is significantly higher but displays a similar shape to the prior test series. After an initial decrease the carbon monoxide concentration remains at a steady level of 40 – 50 ppmv. The initial CO concentration and the overall CO amount are about 5 to 10 times higher compared to the previous tests due to the longer reductions. The CO_2 amount on the other hand is comparable to experiments with a shorter reduction time. The overall carbon monoxide content was in the range of 300 to 500 ppmv and the overall CO_2 content between 80 – 110 ppmv, with a hydrogen purity between 99.94 – 99.96% (table 6 and figure 45). The experiments revealed that only small amounts of the deposited carbon, approximately 5%, are re-oxidized with steam. Teixeira et al. reported a similar carbon oxidation behavior. They suggest that at the beginning carbon structures are cracked until the iron can be oxidized by steam. The more stable graphitized carbon structures are then gradually oxidized. In their experiments the complete removal of carbon with steam was completed after 44 h.[215] The remaining carbon after the steam oxidation serves as a substrate for new carbon deposition[214] in the consecutive cycles. This eventually leads to accumulation of solid carbon and decreasing hydrogen purity with each cycling experiment unless an air-oxidation is performed after each steam oxidation. This effect was not observed in the first set of experiments (1 – 11). A possible explanation is that the effect of accumulating carbon[131,152] and its impact on the carbon monoxide amount were too subtle to be recognized in this test setup during the oxidation. The oxygen carrier conversion (figure 43, right) during the reduction reaction on the other hand might indicate some negative effect of solid carbon building up on the surface. It is possible that the slight decrease of oxygen carrier conversion from reduction 3 to 11 is related to carbon occupying the surface and blocking pores and thus inhibiting the reduction gases from reducing the oxygen carrier.[153] Therefore, the complete air oxidations and the total removal of any solid carbon residue could explain the regeneration effect of the oxygen carrier conversion of cycles 27 to 31, mentioned in section 5.3.2.

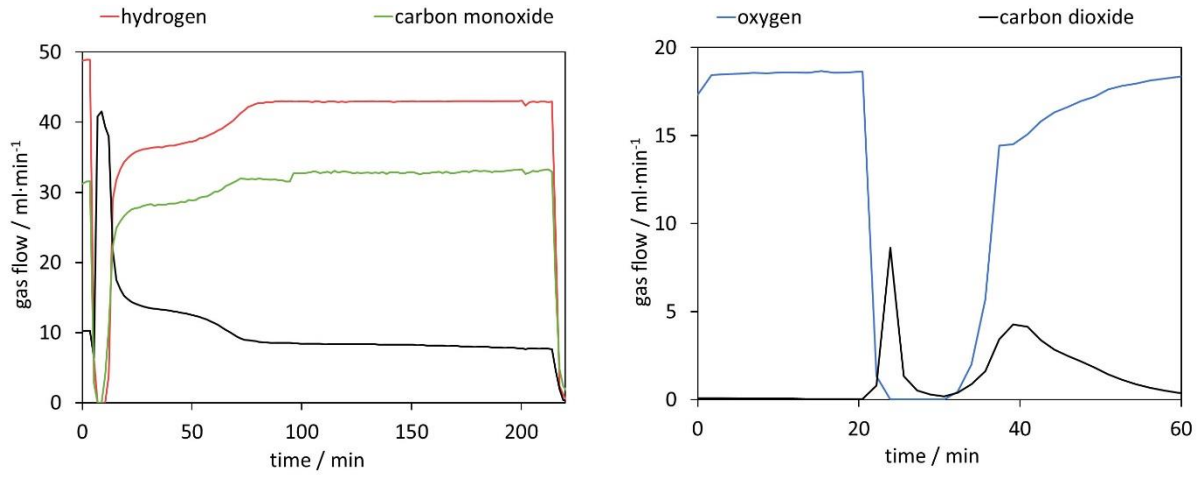

Figure 46: Left: Representative reduction corresponding to cycle 19. The experiments were performed with H_2 54.5 vol%, CO 34 vol% and CO_2 11.5 vol% and a total gas flow of 90 ml min^{-1} at 1023 K and ambient pressure for 210 minutes. Right: Representative air oxidation corresponding to cycle 18. The air oxidations were performed with 100 ml·min^{-1} of synthetic air at 1023 K until a full oxidation had been achieved (approximately 60 minutes).

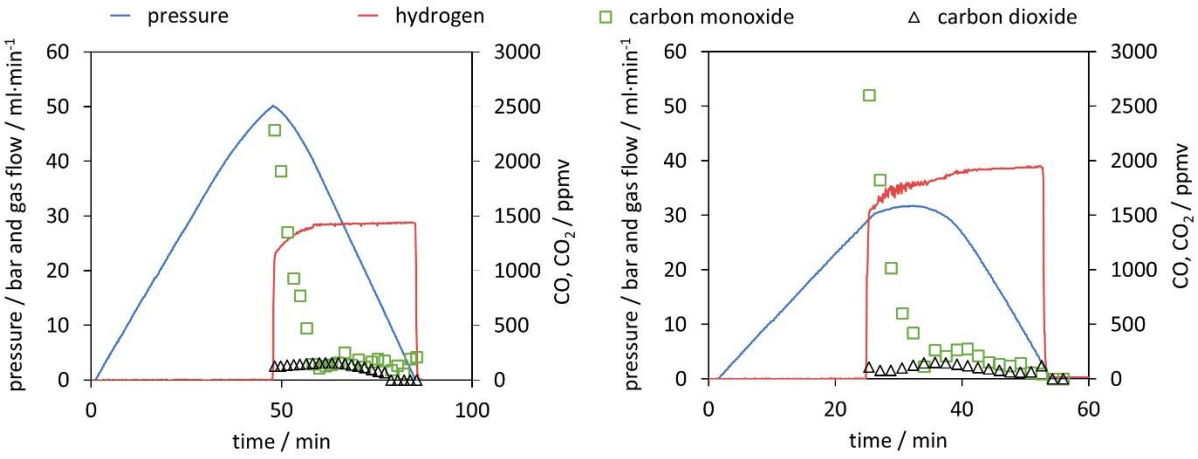

Figure 47: Two representative pressure oxidations performed with 0.06 g·min^{-1} of steam at 1023 K. Left corresponds to oxidation 16, right corresponds to oxidation 19 in table 6.

The result of a representative air oxidation is shown in figure 46, right. Three distinctive parts are noticeable. After the gas stream is switched from bypass to the reactor the oxygen flow immediately drops to 0 and a carbon dioxide peak becomes visible. This clearly indicates that solid carbon, which was not oxidized during the steam oxidation, is now removed from the oxygen carrier.[132,213] The carbon dioxide flow decreases again (minute 27 – 32). At this point of the experiment it is likely that the reaction from magnetite to hematite exclusively takes place eq. 7. After minute 35 another carbon dioxide peak becomes visible, which indicates the oxidation of a different type or source of solid carbon deposition. The most likely explanation is that the first CO_2 peak is the product of carbon oxidation located in the reactor inlet. At this part of the reactor the oxygen carrier was completely reduced to Fe, which is known for

catalyzing carbon deposition. This reaction takes place concurrently with the oxidation of magnetite to hematite. The second peak is measured after the breakthrough of the oxygen at the reactor. This indicates that the oxygen carrier conversion is completed and that another carbon deposit is located at the end of the fixed bed or in the inert section of the reactor outlet.

5.3.5 Post-experimental sample analysis with scanning electron microscopy and XRD diffraction analysis

Samples of the fully reduced oxygen carrier (procedure described as in 5.3.4) were taken and analyzed by scanning electron microscopy (figure 48) and X-ray powder diffraction analysis (figure 51) for further investigation. The image in figure 48, (a) shows the fully reduced oxygen carrier. The sample displayed in figure 48, (b) was re-oxidized with steam at ambient pressure in a thermogravimetric analysis system, and the sample in figure 48, (c) was fully re-oxidized in a muffle furnace at ambient pressure in air. The image in figure 48, (d) shows the fresh and fully oxidized oxygen carrier as a reference. The comparison of the figure 48, (a,b,c) with figure 48, (d) reveals that the oxygen carrier retained its porosity and structural integrity over the whole experiment of pressurized cycling. In all samples with different 3 oxidations stages small dense zones with less porosity are visible, which are related to thermal sintering and a source for the reduced oxygen carrier conversion.[216]

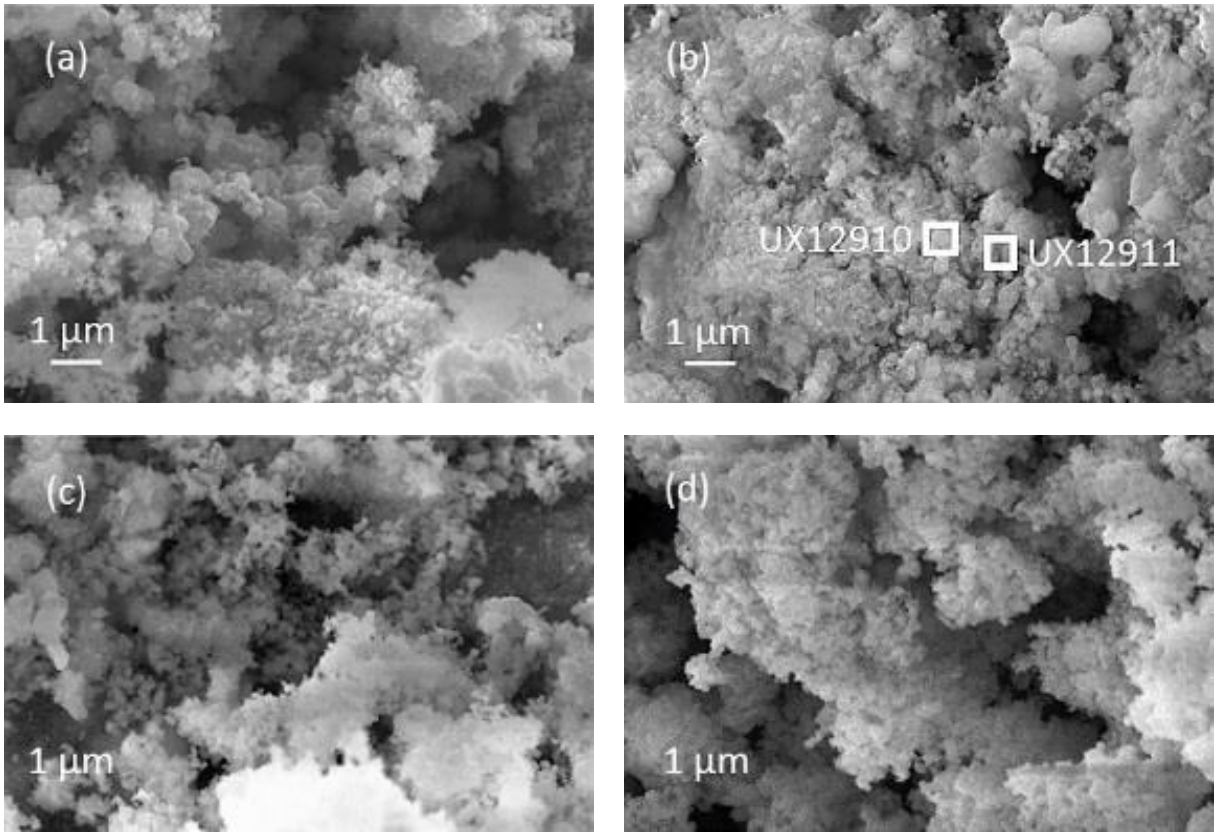

Figure 48: SEM images of the oxygen carrier samples (90 wt% Fe_2O_3, 5 wt% Al_2O_3, 5 wt% CeO_2, grain size 90-125 µm). Samples used in the pressure experiments after 40 cycles: fully reduced (a), re-oxidized to magnetite in a thermogravimetric analysis system with steam (b), fully oxidized to hematite in a muffle furnace in air (c). A fresh fully oxidized sample as reference (d).

Interestingly, samples (a) and (b) did not reveal any signs of solid carbon, although the analysis of the mass balance of the cyclic experiments strongly indicated that a significant amount of carbon was deposited during the reduction. EDX analyses of the sample from two different particles (figure 49) identified the original oxygen carrier composition without deposited carbon. Two possible explanations are conceivable. (i) The oxygen carrier is covered by the solid carbon in a thin layer, which cannot be detected by scanning electron microscopy. Other more noticeable forms of solid carbon, (filaments, plates, nanotubes) which are reported by other groups[214,217] were not formed during the reduction reaction, thus not identified on any of the analyzed samples. (ii) The carbon depositions occur not directly on the oxygen carrier but in its vicinity. Possible substrates for solid carbon are the reactor walls and the inert beds, which cover both reactor ends. The inevitable temperature gradient at both the reactor inlet and outlet can favor the formation of carbon deposits in these regions. This would lead to the measured carbon impurities in the hydrogen produced during the pressure oxidations. Small carbon particles with diameters of roughly 0.2 mm were identified in the ceramic layers at both ends of the reactor. Samples were gather and analyzed by SEM and EDX depicted in figure 50.

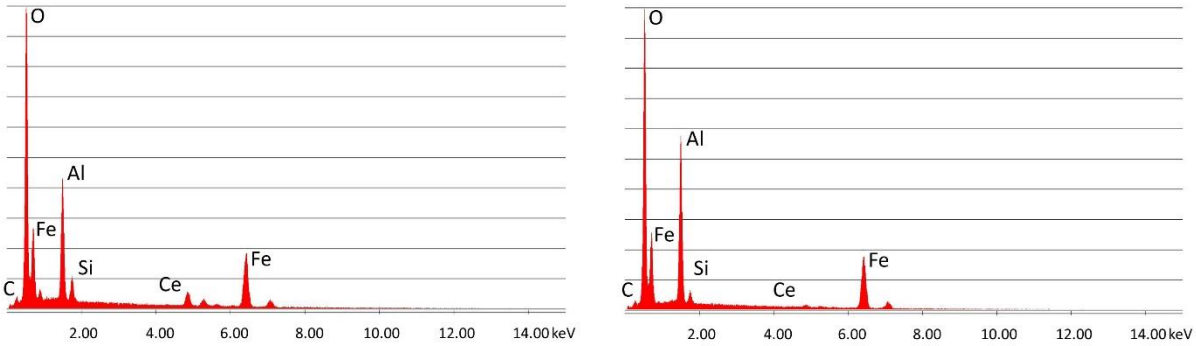

Figure 49: EDX analyses taken from the sample in figure 48, (b). Left: UX129110 and right: UX129110.

The results of the X-ray powder diffraction analysis verify the absence of carbon in the oxygen carrier samples. Thus, under the described experimental conditions, the carbon formation does not take place on the oxygen carrier itself. This is also suggested by the experiment results obtained by the air oxidations and shown in figure 46, right. Two detached CO_2 peaks separated by a region of complete oxygen conversion, which corresponds to the oxidation of magnetite to hematite, were measured. This strongly indicates that two solid carbon sources are oxidized separately, which suggests sources from the reactor bed inlet and outlet.

It is noteworthy that the samples (a) and (b) revealed clearly visible peaks, which are related to hercynite $FeAl_2O_4$, implying a significant amount to be present in the sample. It can thus be concluded that the decrease in oxygen carrier conversion over the measured 11 cycles (figure 43, right) is a combination of thermal sintering effects and the accumulation of $FeAl_2O_4$.[218] This unreactive structure is not removed by steam oxidations but the oxidation with air decomposes this component to Al_2O_3 and Fe_2O_3.[106] Sample (c) shows almost the complete disappearance of peaks related to $FeAl_2O_4$, hence a regeneration of the oxygen carrier conversion is measured in the reductions 27 to 31.[106]

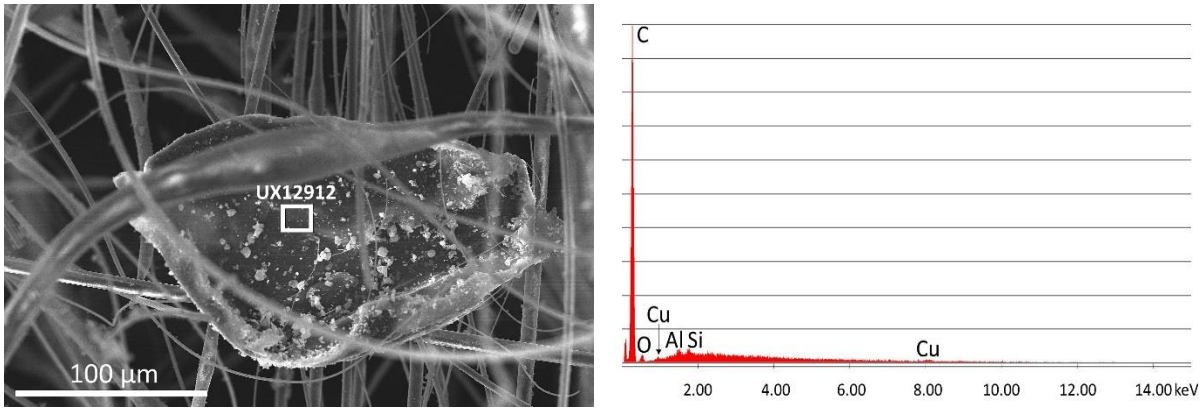

Figure 50: Left: SEM image of a carbon particle found in the inert material at the reactor inlet. The filaments are residues from the ceramic wool. Right: EDX analysis of the carbon particle.

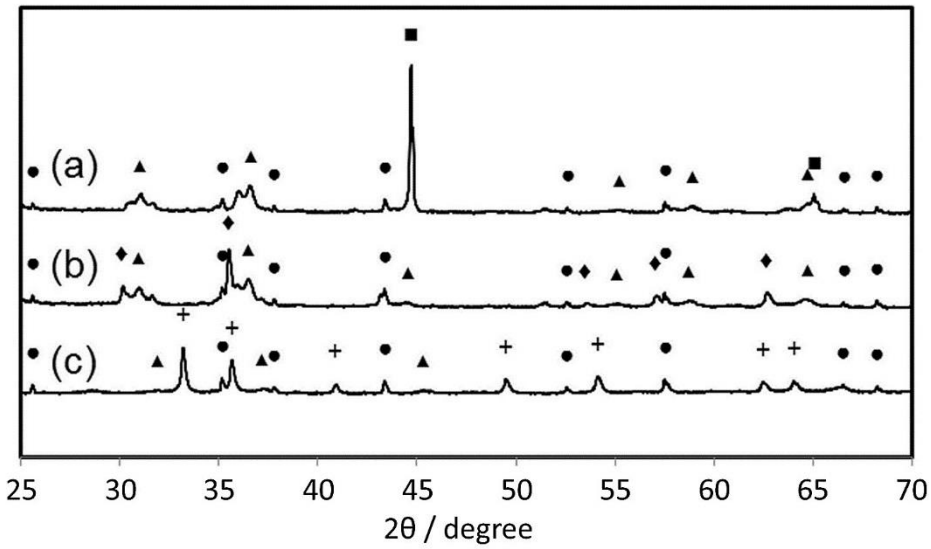

Figure 51: XRD patterns of the oxygen carrier samples used in the pressure experiments (90 wt% Fe_2O_3, 5 wt% Al_2O_3, 5 wt% CeO_2 90 – 125 µm). Fully reduced (a), re-oxidized to magnetite in a thermogravimetric analysis system with steam (b), fully oxidized to hematite in a muffle furnace in air (c). (■) Fe_α, (▲) $FeAl_2O_4$, (●) Al_2O_3, (♦) Fe_3O_4, (+) Fe_2O_3.

5.4 Conclusion

A new tubular high-pressure reactor was designed utilizing the nickel-chromium-cobalt-molybdenum alloy Nicrofer 5520 Co, alloy 617. In the optimized system pressure oxidations with hydrogen are feasible up to 100 bar at a maximum temperature of 1123 K.

Cyclic pressure experiments were performed using an iron-based oxygen carrier mixed with 5 wt% Al_2O_3 and 5 wt% CeO_2. The oxygen carrier was reduced with a synthesis gas (H_2 54.5 vol%, CO 34.0 vol% and CO_2 11.5 vol% and a total gas flow of 90 ml·min^{-1}) at 1023 K and ambient pressure for 90 minutes. The oxidations were performed at different pressure levels with a maximum pressure of 50 bar at 1023 K utilizing 0.06 g·min^{-1} of steam. The process yielded pressurized hydrogen with purities in the range of 99.958% to 99.999%. Carbon monoxide and carbon dioxide were the identified contaminations, which were produced by the oxidation of solid carbon. Carbon depositions, which occurred during the reduction, were identified as the source for solid carbon by calculating the mass balance of each experiment. The pressurized oxidations clearly showed that there is no correlation between the increased system pressure and the hydrogen purity. The source of carbon depositions was further analyzed by increasing the reduction time to 210 minutes to increase the amount of formed carbon significantly. The experiments suggest that the solid carbon is not fully re-oxidized during the steam-oxidation and accumulating in the cyclic experiments. As a consequence the hydrogen purity is decreased gradually with each cycle unless an air oxidation step to completely remove the carbon residues is included after the hydrogen production step.

The post-experimental oxygen carrier analyses with scanning electron microscopy and X-ray powder diffraction analysis revealed that carbon deposition did not take place on the oxygen carrier itself. Neither of the two analysis methods found traces of solid carbon suggesting that carbon formation occurs on the inert material covering both ends of the fixed bed reactor. This is supported by the results of the air oxidations, which showed two CO_2 peaks separated by a region of full oxygen conversion, which corresponds to the oxidation of magnetite to hematite. When dismantling the reactor setup, small carbon particles were found within the ceramic wool.

The oxygen carrier conversion showed a slow linear decrease in the first set of cyclic experiments. A regeneration effect was achieved after steam oxidations including air oxidations were performed. Thermal stress, which leads to sintering of the oxygen carrier, is one source for this decrease. The effect was verified by scanning electron microscopy, which revealed regions with significantly reduced porosity. Another source is the accumulated formation of $FeAl_2O_4$, which gradually reduces the hydrogen yield. Air oxidation can convert $FeAl_2O_4$ back to hematite and Al_2O_3 and explains the oxygen carrier regeneration. X-ray powder diffraction analysis identified the presence of $FeAl_2O_4$ in the fully reduced sample and the magnetite sample and verified the disappearance in the fully oxidized oxygen carrier.

The work has shown that chemical looping water splitting is suitable for the direct production of pressurized hydrogen using hydrocarbons as feed. The gas compression can be achieved in

every fixed bed reactor, which complies with the requirements for high pressure. The main issue with hydrocarbons as feed is the formation of solid carbon and the subsequent hydrogen contamination. The results exhibited similar re-oxidation behavior of solid carbon over the complete pressure range, hence whether the process is operated at atmospheric or elevated system pressure, the conditions to prevent the formation of hydrogen impurities are identical.

6 Conclusion

Hydrogen is a promising energy carrier to support the reduction of greenhouse gas emissions and to mitigate the anthropogenic impact on climate change. However, current state of the art hydrogen production relies on fossil fuels, which undoes the positive effects of hydrogen as energy carrier. Alternative clean production technologies, such as electrolysis and biomass gasification are currently too expensive in their operation and thus not competitive.

Chemical looping hydrogen generation is as very promising technology to produce clean hydrogen out of carbon-based resources in small-scale applications. The process enables a zero-net CO_2 emission operation by relying on renewable sources. In small-scale applications with local renewable feedstocks, it is expected to lower the hydrogen production costs by limiting investment and operation costs for transportation and storage of the hydrogen. In addition, the chemical looping operation in a fixed bed reactor enables the direct production of compressed hydrogen, which reduces the demand for down-stream compression and raises the process efficiency. These process optimizations enable competitive operation costs of small scale systems compared to conventional large-scale centralized production plants.

In a detailed literature review on chemical looping water-splitting technology the substantial progress achieved in this promising field was presented. Iron based oxygen carrier development advanced towards higher cycle stability and redox reactivity by newly proposed compositions and optimized preparation methods. Extensive kinetic studies on the reductions and oxidations provided data for mathematical modelling and for a better understanding of the reactions on a molecular level, which ensures further progress in the field of oxygen carrier development. In recent years the system and process development led to the introduction of several prototypes up to 50 kW with moving and fixed bed reactors. The successfully executed operation tests of these prototypes are a critical step towards commercialization of the chemical looping hydrogen technology. Experimental process development and process simulations broadened the applicability of CLH in terms of applicability and feedstock utilization, product gas yields and carbon capture capabilities. The process simulations suggest that the process efficiency and operations costs of chemical looping water splitting systems can compete with conventional technologies for hydrogen production due to its flexibility and scalability.

Extensive cyclic experiments in a fixed bed reactor under pressurized conditions were performed to investigate the applicability of the chemical looping technology for compressed hydrogen production. The investigations were executed using iron based oxygen carriers prepared by the mechanical mixing method. The preparation method was investigated and developed in a lab scale intensive mixer. The mechanical mixing was easy to upscale was suitable for quickly manufacturing different sample compositions. Samples were prepared by dry mixing of precursor powders and by slowly adding water as aggregation agent during the mixing phase. Pellets with diameters between 0.5 – 2 mm were obtained. High melting metal

oxides were added to the iron oxide to improve its cycle stability. The most promising results were obtained with the compositions $Fe_2O_3/Al_2O_3/CuO$ 80/10/10 wt% and 75/10/15 wt% with a declining hydrogen production yield of approximately 0.2% per cycle. Thermal sintering, due to high operation temperatures, was identified as the cause for this degradation. The stability of the samples prepared by mechanical mixing were inferior compared to wet synthesis methods. Nevertheless, the procedure proved its feasibility for the preparation of samples suitable for an experimental investigation in a lab environment.

The first series of pressurized experiments used pure hydrogen as reducing agent and focused on the stability and structural integrity of the oxygen carrier. The reductions at ambient pressure were followed by oxidations at elevated pressure up to 22 bar. A sequence of different pressure steps were executed and related to the oxygen carrier conversion. The initial oxygen carrier conversion of 84% dropped at a rate of 0.7% per cycle over 15 performed oxidations. The decrease was at a steady level and did not correlate with the varying pressure conditions. The linear pressure increase, which occurred at the highest steam conversion in the first segment of each oxidation preserved the slope throughout the entire investigation. Surface analysis revealed an intact structure and morphology despite the pressure load. A reduced porosity resulting from thermal sintering due to the high reaction temperature was identified, which explained the continuous degradation.

In the second series of pressure experiments a synthetic gas mixture of H_2 54.5 vol%, CO 34.0 vol% and CO_2 11.5 vol% was used as reducing gas mixture at 750 °C. The subsequent pressure oxidations were executed at a maximum pressure up to 50 bar. A special high pressure tubular reactor was designed, which utilized a nickel-chromium-cobalt-molybdenum alloy. This new reactor enabled operations up to 100 bar at 850 °C. The experimental investigation emphasized on the quantitative and qualitative analysis of contaminations in the produced hydrogen. The influence of a higher oxidation pressure on the hydrogen purity was evaluated. Hydrogen with a very high purity in the range of 99.958% to 99.999% was obtained. Carbon monoxide and carbon dioxide were identified as the contaminations, which were formed by the re-oxidation of solid carbon with steam. The solid carbon depositions occurred during the reduction with synthesis gas. The increased oxidation pressure did not influence the concentration of these impurities. The operation parameters, most notably the reaction temperature, the gas composition and the reduction length, were critical for the tendency towards coking. An increased reduction time led to the formation of significantly more solid carbon and thus to a lower hydrogen purity. The oxidations revealed that only small amounts of carbon were re-oxidized by steam, which resulted in an agglomeration of coke in the reactor and a decreasing hydrogen purity. An air oxidation removed the carbon completely. The results suggested that air oxidations need to be included frequently into the cycle sequence to prevent coke agglomeration and avoid a decreasing hydrogen purity.

The air oxidations revealed two completely separated CO_2 peaks, which were related to coke oxidation. This suggested that two detached carbon sources were formed during the

reductions, presumably in the reactor inlet and the reactor outlet. Post experimental analyses confirmed the presence of carbon in these regions of the reactor, while no coke was found on the oxygen carrier itself.

Post experimental analyses by SEM and XRD measurements indicated the formation of hercynite and reduced particle porosity as a result of thermal sintering. Hercynite is a compound formed out of iron oxide and aluminum oxide and is inert in a steam atmosphere. Thus, the formation reduced the amount of active iron in the oxygen carrier and led to a lower hydrogen yield. The oxygen carrier conversion slightly improved by incorporating air oxidations into the cycle sequence, which suggested a back formation of hercynite and a partially countering of the iron losses.

The work presented in this thesis showned that chemical looping water splitting with fixed bed reactors enable the production of compressed and very pure hydrogen. The process can utilize hydrocarbon feedstocks, which are converted to a synthesis gas for the reduction of the oxygen carrier. A critical issue using carbon-based feedstocks is carbon formation, which leads to hydrogen contamination. Since the reductions are executed at atmospheric pressure, the operation parameters to prevent coking are identical to the regular operations. The results exhibited similar re-oxidation behavior of solid carbon over the complete pressure range. The gas compression can be realized in every fixed bed reactor, which complies with the requirements for high pressure. This concludes that the chemical looping technology is suitable for decentralized direct production of compressed and pure hydrogen from renewable carbon feedstocks.

7 Notes and References

¥ Reprinted and adapted from https://yearbook.enerdata.net/energy-consumption-data.html, Copyright Enerdata (2009-2016), with permission from Enerdata, accessed September 2016.

¥¥ Reprinted and adapted from F. Krausmann, S. Gingrich, N. Eisenmenger, K-H. Erb, H. Haberl, M. Fischer-Kowalski, Growth in global materials use, GDP and population during the 20th century, *Ecol. Econ*., 2009, 68, 2696–2705, Copyright (2009), with permission from Elsevier.

¥¥¥ Reprinted and adapted from https://www.statista.com/chart/4322/the-spread-of-the-zika-virus, Copyright (2016), under the Creative Commons Attribution 3.0 International License, accessed September 2016.

¥¥¥¥ Reprinted and adapted from N. Armaroli and V. Balzani, The hydrogen issue, *ChemSusChem* **4,** 2011, 21–36, Copyright (2011), with permission from Wiley-VCH.

¥¥¥¥¥ Reproduced from, Voitic, G. S. Nestl, K. Malli, J. Wagner, B. Bitschnau, F. A. Mautner and V. Hacker*,* High purity pressurised hydrogen production from syngas by the steam-iron process, *RSC Adv.* **6,** 2016, 53533–53541, Copyright (2016), with permission from the Royal Society of Chemistry.

§ Reprinted and adapted from F. Kosaka, H. Hatano, Y. Oshima, and J. Otomo, Iron oxide redox reaction with oxide ion conducting supports for hydrogen production and storage systems, Chem. Eng. Sci., 2015, 123, 380-387, Copyright (2014), with permission from Elsevier.

§§ Reprinted and adapted from Y. Zheng, Y. Wei, K. Li, X. Zhu, H. Wang, and Y. Wang, Chemical-looping steam methane reforming over macroporous CeO_2-ZrO_2 solid solution: Effect of calcination temperature, Int. J. Hydrogen Energy, 2014, 39, 13361–13368, Copyright (2014), with permission from Elsevier.

§§§ Reproduced from W. Liu, M. Ismail, M. T. Dunstan, W. Hu, Z. Zhang, P. S. Fennell, S. A. Scott, and J. S. Dennis, Inhibiting the interaction between FeO and Al_2O_3 during chemical looping production of hydrogen, RSC Adv., 2015, 5, 1759–1771, Copyright (2015), with permission from the Royal Society of Chemistry.

§§§§ Reprinted and adapted with permission from K. Zhao, F. He, Z. Huang, A. Zheng, H. Li, Z. Zhao, Three-dimensionally ordered macroporous $LaFeO_3$ perovskites for chemical-looping steam reforming of methane, Int. J. Hydrogen Energy, 2014, 39, 3243–3252, Copyright (2013) with permission from Elsevier.

§§§§§ Reprinted and adapted with permission from W. Liu, L. Shen, H. Gu and L. Wu, Chemical Looping Hydrogen Generation Using Potassium-Modified Iron Ore as an Oxygen Carrier, Energy Fuels, 2016, 30, 1756-1763, Copyright (2016) American Chemical Society.

§§§§§ Reproduced from, F. He and F. Li, Perovskite promoted iron oxide for hybrid water-splitting and syngas generation with exceptional conversion, Energy Environ. Sci., 2015, 8, 535–539, Copyright (2015), with permission from the Royal Society of Chemistry.

§§§§§ Reprinted and adapted from S. Bhavsar, M. Najera, R. Solunke and G. Veser, Chemical looping: To combustion and beyond, Catal. Today, 2014, 228, 96–105, Copyright (2013), with permission from Elsevier.

£ Reprinted and adapted from A. Tong, S. Bayham, M. V Kathe, L. Zeng, S. Luo, L.-S. Fan and W. G. Lowrie, Iron-based syngas chemical looping process and coal-direct chemical looping process development at Ohio State University, Appl. Energy, 2014, 113, 1836–1845, Copyright (2013), with permission from Elsevier.

ff Reprinted and adapted from M. Rydén and M. Arjmand, Continuous hydrogen production via the steam-iron reaction by chemical looping in a circulating fluidized-bed reactor, Int. J. Hydrogen Energy, 2012, 37, 4843–4854, Copyright (2013), with permission from Elsevier.

fff Reprinted and adapted with permission from B. Moghtaderi, Hydrogen enrichment of fuels using a novel miniaturised chemical looping steam reformer, Chem. Eng. Res. Des., 2012, 90, 19-25, Copyright (2011) The Institution of Chemical Engineers, Published by Elsevier B.V..

ffff Reprinted and adapted with permission from Z. Xue, S. Chen, D. Wang, and W. Xiang, Design and Fluid Dynamic Analysis of a Three-Fluidized-Bed Reactor System for Chemical-Looping Hydrogen Generation, Ind. Eng. Chem. Res., 51, 4267–4278, Copyright (2012) American Chemical Society.

fffff Reprinted and adapted from W. C. Cho, D. Y. Lee, M. W. Seo, S. D. Kim, K. Kang, K. K. Bae, H. Kim, S. Jeong and C. S. Park, Continuous operation characteristics of chemical looping hydrogen production system, Appl. Energy, 2014, 113, 1667–1674, Copyright (2013), with permission from Elsevier.

ffffff Reprinted and adapted from J. Herguido, J. Peña, and E. Carazo, Experimental assessment of hydrogen separation from H_2/H_4 mixtures by the "steam-iron process" in an interconnected circulating fluidized bed reactor, Int. J. Hydrogen Energy, 2014, 39, 14050-14060, Copyright (2014), with permission from Elsevier.

∏ Reprinted and adapted with permission from Q. Yang, Y. Qian, Y. Wang, H. Zhou, and S. Yang, Development of an Oil Shale Retorting Process Integrated with Chemical Looping for Hydrogen Production, Ind. Eng. Chem. Res., 2015, 54, 6156−6164, Copyright (2015) American Chemical Society.

∏∏ Reprinted and adapted from S. Chen, Z. Xue, D. Wang and W. Xiang, Hydrogen and electricity co-production plant integrating steam-iron process and chemical looping combustion, Int. J. Hydrogen Energy, 2012, 37, 8204-8216, Copyright (2012), with permission from Elsevier.

ℓ Reprinted and adapted with permission from X. Hua, W. Wang, and Y. Hu, Analysis of reduction stage of chemical looping packed bed reactor based on the reaction front distribution, J. Mater. Cycles Waste Manag., 2014, 16, 583–590 Copyright (2014) Springer Japan.

ℓℓ Reprinted and adapted with permission from E. R. Monazam, R. W. Breault, and R. Siriwardane, Kinetics of Hematite to Wüstite by Hydrogen for Chemical Looping Combustion, Energy Fuels, 2014, 28, 5406-5414, Copyright (2014) American Chemical Society.

‡ Reprinted and adapted from F. Kosaka, H. Hatano, Y. Oshima, and J. Otomo, Optimization of Disc Parameters Producing More Suitable Size Range of Green Pellets, *Int. J. Metallurgical Eng.,* **1**, 48-59, Copyright (2012), under the Creative Commons Attribution 4.0 International License.

‡‡ Reprinted and adapted with the permission from Maschinenfabrik Gustav Eirich GmbH & Co KG.

1. Enerdata intelligence + consulting, https://yearbook.enerdata.net/energy-consumption-data.html, accessed September 2016.
2. U.S. energy Information administration, International Energy Outlook 2016, DOE/EIA-0484, 2016, 276 pp.
3. D. Warrilow, *Energy Policy*, 2015, **82**, 81–84.
4. S. J. Okullo, F. Reynès and M. W. Hofkes, *Resour. Energy Econ.,* 2015, **40**, 36–56.
5. I. Chapman, *Energy Policy*, 2014, **64**, 93–101.
6. A. M. Jaffe, K. B. Medlock III and R. Soligo, *James A. Bak. III Institute Public Policy, Rice Univ.*, 2011, pp 40.
7. R. Bentley and Y. Bentley, *Energy Policy*, 2015, **86**, 880–890.
8. R.E.H. Sims, R.N. Schock, A. Adegbululgbe, J. Fenhann, I. Konstantinaviciute, W. Moomaw, H.B. Nimir, B. Schlamadinger, J. Torres-Martínez, C. Turner, Y. Uchiyama, S.J.V. Vuori, N. Wamukonya, X. Zhang, 2007: Energy supply. In Climate Change 2007: Mitigation. Contribution of Working Group III to the Fourth Assessment Report of the Intergovernmental Panel on Climate Change [B. Metz, O.R. Davidson, P.R. Bosch, R. Dave, L.A. Meyer (eds.)], Cambridge University Press, Cambridge, United Kingdom and New York, NY, USA.
9. R. G. Miller and S. R: Sorrell SR, *Phil. Trans. R. Soc. A*, **372**, 2014, 20130179.
10. W. K. Tabb, Resource Wars, *Monthly Review,* **58**, 2007.
11. F. Krausmann, S. Gingrich, N. Eisenmenger, K. H. Erb, H. Haberl and M. Fischer-Kowalski, *Ecol. Econ.*, **68**, 2009, 2696–2705.
12. IPCC, 2013: Climate Change 2013: The Physical Science Basis. Contribution of Working Group I to the Fifth Assessment Report of the Intergovernmental Panel on Climate Change [Stocker, T.F., D. Qin, G.-K. Plattner, M. Tignor, S.K. Allen, J. Boschung, A. Nauels, Y. Xia, V. Bex and P.M. Midgley (eds.)]. Cambridge University Press, Cambridge, United Kingdom and New York, NY, USA, 1535 pp.

13. J. Cook, D. Nuccitelli, S. A. Green, M. Richardson, B. Winkler, R. Painting, R. Way, P. Jacobs and A. Skuce, *Environ. Res. Lett.*, **8**, 2013, 1–7.
14. R. S. J. Tol, *Energy Policy*, **73**, 2014, 701–705.
15. R. S. J. Tol, *Energy Policy*, **73**, 2014, 709.
16. R. S. J. Tol, **73**, 2014, 706–708.
17. IPCC, 2014: Climate Change 2014: Synthesis Report. Contribution of Working Groups I, II and III to the Fifth Assessment Report of the Intergovernmental Panel on Climate Change [Core Writing Team, R.K. Pachauri and L.A. Meyer (eds.)]. IPCC, Geneva, Switzerland, 151 pp.
18. M. U. G. Kraemer, M. E. Sinka, K. A. Duda, A. Mylne, F. M. Shearer, O. J. Brady, J. P. Messina, C. M. Barker, C. G. Moore, R. G. Carvalho, G. E. Coelho and W. Van Bortel, *Sci. Data*, 2015, 2-150035.
19. CDC, Zika Virus, http://www.cdc.gov/zika/index.html, accessed Septermber 2016.
20. J. Gillis, In Zika Epidemic, a Warning on Climate Change, The NewYork Times Science, http://www.nytimes.com/2016/02/21/world/americas/in-zika-epidemic-a-warning-on-climate-change.html, accessed September 2016.
21. N. McCarthy, https://www.statista.com/chart/4322/the-spread-of-the-zika-virus, accessed September 2016.
22. UNFCCC. Conference of the Parties (COP), ADOPTION OF THE PARIS AGREEMENT Proposal by the President, FCCC/CP/2015/L.9, United Nations Office at Geneva, 2015.
23. IEA International Energy Agency, Key World Energy Statistics 2015, OECD/IEA, 2015.
24. N. Armaroli and V. Balzani, *ChemSusChem*, **4**, 2011, 21–36.
25. J. D. Holladay, J. Hu, D. L. King and Y. Wang, *Catal. Today*, **139**, 2009, 244–260.
26. S. K. Ngoh and D. Njomo, *Renew. Sustain. Energy Rev.*, **16**, 2012, 6782–6792.
27. R. Chaubey, S. Sahu, O. O. James and S. Maity, *Renew. Sustain. Energy Rev.*, **23**, 2013, 443–462, 2013.
28. W. C. Cho, D. Y. Lee, M. W. Seo, S. D. Kim, K. Kang, K. K. Bae, H. Kim, S. Jeong and C. S. Park, *Appl. Energy*, **113**, 2014, 1667–1674.
29. B. Sørensen, Hydrogen and Fuel Cells (Second Edition) Emerging technologies and applications Second Edition," Emerging Technologies and Applications, A volume in Sustainable World, Academic press, 2011, chapter 2, 5–94.
30. M Singh, J. Moore and B. Shadis, Hydrogen Demand, Production and Costs by Region to 2050, 84th Annual Meeting of the Transpiration research Board, Washington D.C., January, 2004.
31. K. Zech, E. Grasemann, K. Oehmichen, I. Kiendl, R. Schmersahl, S. Rönsch, M. Seiffert, J. Michaelis and P. Trainer, DBFZ Report Nr . 19 Hy-NOW Evaluierung der Verfahren und Technologien für die Bereitstellung von Wasserstoff auf Basis von Biomasse, *DBFZ Rep. Hy-NOW*, **19**, 2014.
32. P. Spath, A. Aden, T. Eggeman, M. Ringer, B. Wallace and J. Jechura, Biomass to Hydrogen Production Detailed Design and Economics Utilizing the Battelle Columbus Laboratory Indirectly- Heated Gasifier, National Renewable Energy Laboratory, 2005, Technical Report NREL/TP-510-37408.

33. M. R. Shaner, H. A. Atwater, S. Lewis and E. W. Mcfarland, *Energy Environ. Sci.*, **9**, 2016, 2354-2371.
34. IEA International Energy Agency, Technology Roadmap Hydrogen and Fuel Cells, OECD/IEA, 2015.
35. National Renewable Energy Laboratory, Hydrogen Production Cost Estimate Using Biomass Gasification, NREL/BK-6A10-51726, 2011.
36. K. Reddi, A. Elgowainy and E. Sutherland, *Int. J. Hydrogen Energy*, **39**, 2014, 19169–19181.
37. A. Elgowainy, K. Reddi, E. Sutherland and F. Joseck, *Int. J. Hydrogen Energy*, **39**, 2014, 20197–20206.
38. J. Alazemi and J. Andrews, *Renew. Sustain. Energy Rev.*, **48**, 2015, 483–499.
39. N. Rustagi, A. Elgowainy, E. Gupta, Hydrogen Delivery Cost Projections – 2015, DOE Hydrogen and Fuel Cells Program Record, 2016.
40. A. A. Wade, Costs of Storing and Transporting Hydrogen, *National Renewable Energy Laboratory*, NREL/TP-570-25106, 1998.
41. National Renewable Energy Laboratory, State-of-the-Art Hydrogen Production Cost Estimate Using Water Electrolysis, NREL/BK-6A1-46676, 2009.
42. A. Elgowainy, Hydrogen Infrastructure Analysis in Early Markets of FCEVs, North America Workshop Bethesda, Maryland, January, 2014.
43. e-mobil BW GmbH – Landesagentur für Elektromobilität und Brennstoffzellentechnologie, Wasserstoffinfrastruktur für eine nachhaltige Mobilität, Baden-Württemberg, 2013.
44. P. E. Dodds, W. McDowall, A review of hydrogen delivery technologies for energy system models, UCL Energy Institute, UKSHEC Working Paper No. 7, 2012.
45. V. Hacker, G. Faleschini, H. Fuchs, R. Fankhauser, G. Simader, M. Ghaemi, B. Spreitz and K. Friedrich, *J. Power Sources*, **71**, 1998, 226–230.
46. V. Hacker, *J. Power Sources*, **118**, 2003, 311–314.
47. J. Adanez, A. Abad, F. Garcia-Labiano, P. Gayan and L. F. De Diego, *Prog. Energy Combust. Sci.*, **38**, 2012, 215–282.
48. A. Tong, D. Sridhar, Z. Sun, H. R. Kim, L. Zeng, F. Wang, D. Wang, M. V. Kathe, S. Luo, Y. Sun and L. S. Fan, *Fuel,* **103**, 2013, 495–505.
49. Kolbitsch, T. Pröll, J. Bolhar-Nordenkampf and H. Hofbauer, *Chem. Eng. Technol.*, **32**, 2009, 398–403.
50. S. D. Fraser, M. Monsberger and V. Hacker, *J. Power Sources*, **161**, 2006, 420–431.
51. M. Thaler and V. Hacker, *Int. J. Hydrogen Energy*, **37**, 2012, 2800–2806.
52. S. Nestl, V. Hacker, and G. Voitic, Pat. WO2016011473A1, 2016.
53. S. Nestl, Biogas reforming and the steam iron process for the production of pressurised hydrogen, University of Technology Graz, 2015.
54. G. Voitic, S. Nestl, K. Malli, J. Wagner, B. Bitschnau, F. Mautner and V. Hacker, *RSC Adv.*, **6**, 2016, 53533–53541.
55. S. Nestl, G. Voitic, M. Lammer, B. Marius, J. Wagner and V. Hacker, *J. Power Sources*, **280**, 2015, 57–65.
56. R. K. Ahluwalia, T. Q. Hua, and J. Peng, , *Int. J. Hydrogen Energy,* **32**, 2007, 3592–3602.

57. D. D. Papadias, S. H. D. Lee, M. Ferrandon and S. Ahmed, *Int. J. Hydrogen Energy*, 2010, **35**, 2004–2017.
58. M. Ortiz, L. F. de Diego, A. Abad, F. Garcia-Labiano, P. Gayan and J. Adanez, *Int. J. Hydrogen Energy*, 2010, **35**, 151–160.
59. F. Garcia-Labiano, J. Adanez, L. F. Diego, P. Gayan and A. Abad, *Energy & Fuels*, 2006, **20**, 26–33.
60. R. Xiao, Q. Song, M. Song, Z. Lu S. Zhanga and L. Shen, *Combust. Flame*, 2010, **157**, 1140–1153.
61. S. Zhang, C. Saha, Y. Yang, S. Bhattacharya and R. Xiao, *Energy Fuels*, 2011, **25**, 4357-4366.
62. S. Zhang, R. Xiao and W. Zheng, *Appl. Energy*, 2014, **130**, 181–189.
63. R. Siriwardane, J. Poston, K. Chaudhari, A. Zinn, T. Simonyi and C. Robinson, *Energy Fuels*, 2007, **21**, 1582-1591.
64. O. Nordness, L. Han, Z. Zhou and G. M. Bollas, *Energy Fuels*, 2016, **30**, 504−514.
65. H. P. Hamers, F. Gallucci, G. Williams, P. D. Cobden and M. V. S. Annaland, *Energy Fuels*, **29**, 2015, 2656−2663.
66. P. Hamers, *Packed Bed Chemical-Looping Combustion experimental demonstration and energy analysis*, Technical University Eindhoven, 2014.
67. L. Fan, *Chemical Looping Systems for Fossil Energy Conversions*, John Wiley & Sons, Inc., Hoboken, New Jersey, 2010.
68. A. Thursfield, A. Murugan, R. Franca and I. S. Metcalfe, *Energy Environ. Sci.*, 2012, **5**, 7421-7459.
69. A. Messerschmitt, US pat., 971206, 1910.
70. C.E. Parsons, US pat., 1658939, 1926.
71. W. H. Marshall, US pat., 2182747, 1939.
72. H. C. Reed, US pat., 2635947, 1953.
73. F. Bergius, US pat., 1059818, 1913.
74. D. D. Miller and R. Siriwardane, *Energy Fuels*, 2013, **27**, 4087–4096.
75. B. Dou, Y. Song, C. Wang, H. Chen and Y. Xu, *Renew. Sustain. Energy Rev.*, 2014, **30**, 950–960.
76. E. Lorente, J. A. Peña and J. Herguido, *Int. J. Hydrogen Energy*, 2008, **33**, 615–626.
77. F. Li, H. R. Kim, D. Sridhar, F. Wang, L. Zeng, J. Chen and L.-S. Fan, *Energy Fuels*, 2009, **23**, 4182–4189.
78. M. Ortiz, L. F. De Diego, A. Abad, F. García-Labiano, P. Gayan and J. Adanez, *Energy Fuels*, 2012, **26**, 791–800.
79. X.-L. Liu, X.-J. Yin and H. Zhang, *Energy Fuels*, 2014, **28**, 6066–6076.
80. R. D. Solunke, *Ind. Eng. Chem. Res.*, 2010, **49**, 11037–11044.
81. P. Gupta, L. G. Velazquez-vargas and L. Fan, *Energy Fuels*, 2007, **21**, 2900–2908.
82. M. Thaler, V. Hacker, M. Anilkumar, J. Albering, J. O. Besenhard, H. Schröttner and M. Schmied, *Int. J. Hydrogen Energy*, 2006, **31**, 2025–2031.
83. V. J. Aston, B. W. Evanko and A. W. Weimer, *Int. J. Hydrogen Energy*, 2013, **38**, 9085-9096.
84. X. Zhu, Y. Wei, H. Wang and K. Li, *Int. J. Hydrogen Energy*, 2013, **38**, 4492–4501.
85. H. Fang, L. Haibin and Z. Zengli, *Int. J. Chem. Eng.*, **2009**, 1–16.
86. N. L. Galinsky, Y. Huang and F. Li, *Sustain. Chem. Eng.*, 2013, **1**, 364−373.
87. W. Liu, J. S. Dennis and S. A. Scott, *Ind. Eng. Chem. Res.*, 2012, **51**, 16597–16609.

88. W. C. Cho, C. G. Kim, S. U. Jeong, C. S. Park, K. S. Kang, D. Y. Lee and S. D. Kim, *Ind. Eng. Chem. Res.*, 2015, **54**, 3091–3100.
89. W. C. Cho, M. W. Seo, S. D. Kim, K. S. Kang, K. K. Bae, H. Kim, S. U. Jeong and C. S. Park, *Int. J. Hydrogen Energy*, 2012, **37**, 16852–16863.
90. F. Kosaka, H. Hatano, Y. Oshima and J. Otomo, *Chem. Eng. Sci.*, 2015, **123**, 380–387.
91. Y. Zheng, X. Zhu, H. Wang, K. Li, Y. Wang and Y. Wei, *J. Rare Earths*, 2014, **32**, 842–848.
92. Y. Zheng, Y. Wei, K. Li, X. Zhu, H. Wang, and Y. Wang, *Int. J. Hydrogen Energy*, 2014, **39**, 13361–13368.
93. X. Zhu, K. Li, Y. Wei, H. Wang and L. Sun, *Energy Fuels*, 2014, **28**, 754–760.
94. Z. Gu, K. Li, S. Qing, X. Zhu, Y. Wei, Y. Li and H. Wang, *RSC Adv*, 2014, **4**, 47191–47199.
95. E. Romero, R. Soto, P. Durán, J. Herguido and J. A. Peña, *Int. J. Hydrogen Energy*, 2011, **37**, 6978–6984.
96. P. Datta, L. K. Rihko-Struckmann and K. Sundmacher, *Mater. Chem. Phys.*, 2011, **129**, 1089–1095.
97. P. Datta, L. K. Rihko-Struckmann and K. Sundmacher, *Fuel Process. Technol.*, 2014, **128**, 36–42.
98. H. Wang, J. Zhang, F. Wen and J. Bai, *RSC Adv*, 2013, **3**, 10341–10348.
99. P. Datta, *Mater. Res. Bull.*, 2013, **48**, 4008–4015.
100. M. Ismail, W. Liu, M. T. Dunstan and S. A. Scott, *Int. J. Hydrogen Energy*, 2015, **41**, 4073-4084.
101. M. S. C. Chan, W. Liu, M. Ismail, Y. Yang, S. A. Scott and J. S. Dennis, *Chem. Eng. J.*, 2016, **296**, 406–411.
102. P. R. Kidambi, J. P. E. Cleeton, S. A. Scott, J. S. Dennis and C. D. Bohn, *Energy Fuels*, 2012, **26**, 603–617.
103. A. M. Kierzkowska, C. D. Bohn, S. A. Scott, J. P. Cleeton, J. S. Dennis and C. R. Mu, *Ind. Eng. Chem. Res.*, 2010, **49**, 5383–5391.
104. C. D. Bohn, J. P. Cleeton, C. R. Müller, S. A. Scott and J. S. Dennis, *Energy Fuels*, 2010, **24**, 4025–4033.
105. M. Ishida, K. Takeshita, K. Suzuki and T. Ohba, *Energy Fuels*, 2005, **19**, 2514–2518.
106. W. Liu, M. Ismail, M. T. Dunstan, W. Hu, Z. Zhang, P. S. Fennell, S. A. Scott, and J. S. Dennis, *RSC Adv.*, 2015, **5**, 1759–1771.
107. M. Mufti, E. Jerndal, H. Leion, T. Mattisson and A. Lyngfelt, *Chem. Eng. Res. Des.*, 2010, **88**, 1505–1514.
108. F. Liu, Y. Zhang, L. Chen, D. Qian, J. K. Neathery, S. Kozo and K. Liu, *Energy Fuels*,2013, **27**, 5987–5995.
109. H. Leion, A. Lyngfelt, M. Johansson, E. Jerndal and T. Mattisson, *Chem. Eng. Res. Des.*, 2008, **86**, 1017–1026.
110. Y. Ku, Y.-C. Liu, P.-C. Chiu, Y.-L. Kuo and Y.-H. Tseng, *Ceram. Int.*, 2014, **40**, 4599–4605.
111. R. Xiao, S. Zhang, S. Peng, D. Shen, and K. Liu, *Int. J. Hydrogen Energy*, 2014, **39**, 19955-19969.
112. A. Tong, S. Bayham, M. V Kathe, L. Zeng, S. Luo, L.-S. Fan and W. G. Lowrie, *Appl. Energy*, 2014, **113**, 1836–1845.
113. W. Liu, L. Shen, H. Gu and L. Wu, *Energy Fuels*, 2016, **30**, 1756–1763.
114. F.-X. Chiron and G. S. Patience, *Int. J. Hydrogen Energy*, 2012, **37**, 10526–10538.
115. T dl R. Castillo, J. S. Gutiérrez, A. L. Ortiz and V. Collins-Martínez, *Int. J. Hydrogen Energy*, 2013, **38**, 12519–12526.
116. H. Liang, *Int. J. Hydrogen Energy*, 2015, **40**, 13338–13343.

117. N. L. Galinsky, A. Shafiefarhood, Y. Chen, L. Neal and F. Li, *Applied Catal. B, Environ.*, 2015, **164**, 371–379.
118. K. Zhao, F. He, Z. Huang, A. Zheng, H. Li and Z. Zhao, *Int. J. Hydrogen Energy*, 2014, **39**, 3243–3252.
119. K. Zhao, F. He, Z. Huang, G. Wei, A. Zheng, H. Li and Z. Zhao, *Appl. Energy*, 2016, **168**, 193–203.
120. I. Popescu, Y. Wu, P. Granger and I. Marcu, *Applied Catal. A, Gen.*, 2014, **485**, 20–27.
121. C. Feng, S. Ruan, J. Li, B. Zou, J. Luo, W. Chen, W. Dong and F. Wu, *Sensors Actuators B*, 2011, **155**, 232–238.
122. W. Haron, T. Thaweechai and W. Wattanathana, *Energy Procedia*, 2013, **34**, 791–800.
123. F. He and F. Li, *Energy Environ. Sci.*, 2015, **8**, 535–539.
124. T. A. S. Ferreira, J. C. Waerenborgh, M. H. R. M. Mendonça, M. R. Nunes and F. M. Costa, *Solid State Sci.*, 2003, **5**, 383–392.
125. D. S. Mathew and R. Juang, *Chem. Eng. J.*, 2007, **129**, 51–65.
126. E. Manova, B. Kunev, D. Paneva, I. Mitov and L. Petrov, *Chem. Mater.*, 2004, **16**, 5689-5696.
127. Y. Qu, H. Yang, N. Yang, Y. Fan, H. Zhu and G. Zou, *Mater. Lett.*, 2006, **60**, 3548–3552.
128. K. Svoboda, G. Slowinski, J. Rogut and D. Baxter, *Energy Convers. Manag.*, 2007, **48**, 3063–3073.
129. V. Crocellà, F. Cavani, G. Cerrato, S. Cocchi, M. Comito, G. Magnacca and C. Morterra, *J. Phys. Chem. C*, 2012, **116**, 4998–15009.
130. S. Cocchi, M. Mari, F. Cavani and J.-M. M. Millet, *Appl. Catal. B, Environ.*, 2014, **152-153**, 250–261.
131. C. Trevisanut, M. Mari, J.-M. M. Millet and F. Cavani, *Int. J. Hydrogen Energy*, 2015, **40**, 5264–5271.
132. O. Vozniuk, S. Agnoli, L. Artiglia, A. Vassoi, N. Tanchoux, F. Di Renzo, G. Granozzi and F. Cavani, *Green Chem.*, 2016, **18**, 1038–1050.
133. Y. Kuo, W. Huang, W. Hsu, Y. Tseng and Y. Ku, *Aerosol Air Qual. Res.*, 2015, **15**, 2700-2708.
134. S. Bhavsar, M. Najera, R. Solunke and G. Veser, *Catal. Today*, 2014, **228**, 96–105.
135. M. Rydén and M. Arjmand, *Int. J. Hydrogen Energy*, 2012, **37**, 4843–4854.
136. A. Edrisi, Z. Mansoori and B. Dabir, *Int. J. Hydrogen Energy*, 2014, **39**, 8271–8282.
137. D. Sanfilippo, *Catal. Today*, 2016, **272**, 58-68.
138. M. Sorgenfrei and G. Tsatsaronis, *Appl. Energy*, 2014, **113**, 1958–1964.
139. D. Zeng, R. Xiao, Z. Huang, J. Zeng and H. Zhang, *Int. J. Hydrogen Energy*, 2016, **41**, 6676-6684, 2016.
140. Z. Xue, S. Chen, D. Wang, and W. Xiang, *Ind. Eng. Chem. Res.*, 2012, **51**, 4267–4278.
141. S. Chen, Z. Xue, D. Wang, and W. Xiang, *Int. J. Hydrogen Energy*, 2012, **37**, 8204–8216.
142. J. Herguido, J. A. Peña, and E. Carazo, *Int. J. Hydrogen Energy*, 2014, **39**, 14050–14060.
143. D. Sridhar, A. Tong, H. Kim, L. Zeng, F. Li, L.-S. Fan and W. G. Lowrie, *Energy Fuels*, 2012, **26**, 2292−2302.
144. A. Tong, L. Zeng, M. V Kathe, D. Sridhar, L.-S. Fan and W. G. Lowrie, *Energy Fuels*, 2013, **27**, 4119–4128.
145. M. V Kathe, A. Empfield, J. Na, E. Blair and L. Fan, *Appl. Energy*, 2016, **165**, 183–201.
146. B. Moghtaderi, *Chem. Eng. Res. Des.*, 2012, **90**, 19–25.
147. B. Moghtaderi and E. Doroodchi, *Int. J. Hydrogen Energy*, 2012, **37**, 15164–15169.
148. D.-W. Zeng, R. Xiao, S. Zhang and H.-Y. Zhang, *Fuel Process. Technol.*, 2015, **139**, 1–7.

149. Y. S. Hong, K. S. Kang, C. S. Park, D. Kim, J. W. Bae, J. W. Nam, Y. Lee and D. H. Lee, *Int. J. Hydrogen Energy*, 2013, **38**, 6052–6058.
150. D. Lee, M. W. Seo, T. D. B. Nguyen, W. C. Cho and S. D. Kim, *Int. J. Hydrogen Energy*, 2014, **39**, 14546–14556.
151. E. Hormilleja, P. Durán, J. Plou, J. Herguido, and J. A. Peña, *Int. J. Hydrogen Energy*, 2014, **39**, 5267–5273.
152. R. Campo, P. Durán, J. Plou, J. Herguido and J. A. Peña, *J. Power Sources*, 2013, **242**, 520–526.
153. C. Trevisanut, F. Bosselet, F. Cavani and J. M. M. Millet, *Catal. Sci. Technol*, 2015, **5**, 1280-1289.
154. M. G. Rosmaninho, F. C. C. Moura, L. R. Souza, R. K. Nogueira, G. M. Gomes, J. S. Nascimento, M. C. Pereira, J. D. Fabris, J. D. Ardisson, M. S. Nazzarro, K. Sapag, M. H. Araújo and R. M. Lago, *Appl. Catal. B Environ.*, 2012, **115–116**, 45–52.
155. J. Plou, P. Durán, J. Herguido and J. A. Peña, *Fuel*, 2014, **140**, 470–476.
156. J. Plou, P. Durán, J. Herguido and J. A. Peña, *Fuel*, 2014, **118**, 100–106.
157. M. Herrer, J. Plou, P. Durán, J. Herguido and J. A. Peña, *Int. J. Hydrogen Energy*, 2015, **40**, 5244–5250.
158. G. Voitic, S. Nestl, M. Lammer, J. Wagner and V. Hacker, *Appl. Energy*, 2015, **157**, 399-407.
159. Y. Tsai, L. Liu and D. Chen, *RSC Adv.*, 2016, **6**, 8930–8934.
160. K. Michiels, J. Spooren and V. Meynen, *Fuel*, 2015, **160**, 205–216.
161. A.-M. Cormos and C.-C. Cormos, *Int. J. Hydrogen Energy*, 2014, **39**, 2067–2077.
162. C. Cormos, A. Cormos and L. Petrescu, *Chem. Eng. Trans.*, 2014, **39**, 347–252.
163. C.-C. Cormos, *Int. J. Greenh. Gas Control*, 2012, **37**, 13371–13386.
164. C.-C. Cormos, A.-M. Cormos, and L. Petrescu, *Chem. Eng. Res. Des.*, 2014, **92**, 741–751.
165. S. Mukherjee, P. Kumar, A. Hosseini, A. Yang and P. Fennell, *Energy Fuels*, 2014, **28**, 1028–1040.
166. Q. Yang, Y. Qian, Y. Wang, H. Zhou and S. Yang, *Ind. Eng. Chem. Res.*, 2015, **54**, 6156-6164.
167. S. Chen, Z. Xue, D. Wang and W. Xiang, *J. Power Sources*, 2012, **215**, 89–98.
168. L. Zeng, F. He, F. Li, L.-S. Fan and W. G. Lowrie, *Energy Fuels*, 2012, **26**, 3680–3690.
169. H. Ozcan and I. Dincer, *Energy Convers. Manag.*, 2014, **85**, 477–487.
170. K.-S. Kang, C.-H. Kim, K.-K. Bae, W.-C. Cho, S.-U. Jeong, S.-H. Kim and C.-S. Park, *Int. J. Hydrogen Energy*, 2012, **37**, 3251–3260.
171. M. N. Khan and T. Shamim, *Appl. Energy*, 2016, **162**, 1186–1194.
172. X. Zhang, S. Li, H. Hong and H. Jin, *Energy Convers. Manag.*, 2014, **85**, 701–708.
173. X. Zhang and H. Jin, *Appl. Energy*, 2013, **112**, 800–807.
174. X. Zhang, S. Li and H. Jin, *Energies*, 2014, **7**, 7166–7177.
175. C.-C. Cormos, *Fuel Process. Technol.*, 2015, **137**, 16–23.
176. L. Yan, G. Yue and B. He, *Bioresour. Technol.*, 2016, **205**, 133–141.
177. L. Yan, B. He, X. Pei, C. Wang, Z. Duan, J. Song and X. Li, *Int. J. Hydrogen Energy*, 2014, **39**, 17540–17553.
178. C.-C. Cormos, *Int. J. Hydrogen Energy*, 2014, **39**, 5597–5606.
179. S. G. Gopaul, A. Dutta and R. Clemmer, *Int. J. Hydrogen Energy*, 2014, **39**, 5804–5817.
180. A. Sanz, D. Nieva and J. Dufour, *Int. J. Hydrogen Energy*, 2015, **40**, 5074–5080.
181. A. Edrisi, Z. Mansoori, B. Dabir and A. Shahnazari, *Int. J. Hydrogen Energy*, 2014, **39**, 10380–10391.

182. J. Zhu, W. Wang, X. N. Hua, F. Wang, Z. Xia and Z. Deng, *Int. J. Hydrogen Energy*, 2015, **40**, 12097–12107.
183. X. Hua, W. Wang and Y. Hu, *J Mater Cycles Waste Manag*, 2014, **16**, 583–590.
184. X. Hua, W. Wang and F. Wang, *Front. Environ. Sci. Eng.*, 2015, **9**, 1130–1138.
185. C. Hertel, P. Heidebrecht, and K. Sundmacher, *Int. J. Hydrogen Energy*, 2012, **37**, 2195-2203.
186. K.-S. Kang, C.-H. Kim, K.-K. Bae, W.-C. Cho, S.-U. Jeong, Y.-J. Lee and C.-S. Park, *Chem. Eng. Res. Des.*, 2014, **92**, 2584–2597.
187. S. Nasr and K. P. Plucknett, *Energy Fuels*, 2014, **28**, 1387–1395.
188. E. R. Monazam, R. W. Breault and R. Siriwardane, *Energy Fuels*, 2014, **28**, 5406–5414.
189. E. R. Monazam, R. W. Breault, R. Siriwardane, G. Richards and S. Carpenter, *Chem. Eng. J.*, 2013, **232**, 478–487.
190. Y. Zhang, E. Doroodchi and B. Moghtaderi, *Energy Fuels*, 2015, **29**, 337–345.
191. Y. Zhang, E. Doroodchi and B. Moghtaderi, *Appl. Energy*, 2014, **113**, 1916–1923.
192. E. Ksepko, M. Sciazko and P. Babinski, *Appl. Energy*, 2014, **115**, 374–383.
193. M. H. Jeong, D. H. Lee and J. W. Bae, *Int. J. Hydrogen Energy*, 2015, **40**, 2613–2620.
194. W. Liu, J. Y. Lim, M. A. Saucedo, A. N. Hayhurst, S. A. Scott and J. S. Dennis, *Chem. Eng. Sci.*, 2014, **120**, 149–166.
195. J. Plou, P. Durán, J. Herguido and J. A. Peña, *Int. J. Hydrogen Energy*, 2012, **37**, 6695-7004.
196. R. C. Stehle, M. M. Bobek and D. W. Hahn, *Int. J. Hydrogen Energy*, 2015, **40**, 1675-1689.
197. M. M. Bobek, R. C. Stehle and D. W. Hahn, *Materials*, 2012, **5**, 2003–2014.
198. A. Singh, F. Al-Raqom, J. Klausner and J. Petrasch, *Int. J. Hydrogen Energy*, 2012, **37**, 7442–7450.
199. M. Thaler, *Kontaktmassenentwicklung für den Metall-Dampf-Prozess zur Erzeugung und Speicherung von Wasserstoff für Brennstoffzellen*, Graz University of Technology, 2009.
200. M. Zhu and I. E. Wachs, *ACS Catal.*, 2016, **6**, 722–732.
201. P. Pandey, N. F. Lobo and P. Kumar, *Int. J. Metall. Eng.*, 2012, **1**, 48–59.
202. M. Lammer, *Investigations on Generation of Ultra-Pure Hydrogen By the Steam-Iron Process Using a Tubular Reactor System*, Graz University of Technology, 2014.
203. K. Malli, *Enhancement of the iron-based Oxygen Carrier for the Steam-Iron Process : Effects of Preparation Methods and Additive Metals on Hydrogen Production,* Graz University of Technology, 2016.
204. B. Marius, *Investigation and characterization of contact mass stability in the reversible steam-iron process for hydrogen production, –storage and –purification,* Graz University of Technology, 2014.
205. C. Schaffer, *Untersuchung der Druckwasserstoffherstellung durch den Eisen-Dampf-Prozess*, Graz University of Technology, 2015.
206. B. Maunz, Optimierung des Reformer Eisen-Dampf-Prozesses zur Wasserstoffherstellung, University of Technology, 2014.
207. M. Ziegler, *Auslegung und Erprobung eines Reaktors für den Eisen-Dampf Prozess zur Herstellung von komprimiertem Wasserstoff*, Graz University of Technology, 2016.
208. AD 2000-Merkblatt B0, *Berechnung von Druckbehältern*, 2007.
209. AD 2000-Merkblatt B1, *Zylinder- und Kugelschalen unter innerem Überdruck*, 2000.
210. VDM, *Alloy 617, Nicrofer 5520 Co*, VDM Metals GmbH, Germany, 2005.
211. V. V. Galvita, H. Poelman, V. Bliznuk, C. Detavernier and G. B. Marin, *Ind. Eng. Chem. Res.*, 2013, **52**, 8416–8426.

212. C. R. Müller, C. D. Bohn, Q. Song, S. A. Scott and J. S. Dennis, *Chem. Eng. J.*, 2011, **166**, 1052–1060.
213. C. D. Bohn, C. R. Müller, J. P. Cleeton, A. N. Hayhurst, J. F. Davidson, S. A. Scott and J. S. Dennis, *Ind. Eng. Chem. Res.*, 2008, **47**, 7623–7630.
214. J. Zhang, A. Schneider and G. Inden, *Corros. Sci.*, 2003, **45**, 281–299.
215. I. F. Teixeira, T. P. V Medeiros, P. E. Freitas, M. G. Rosmaninho, J. D. Ardisson and R. M. Lago, *Fuel*, 2014, **124**, 7–13.
216. E. Lorente, J. A. Peña and J. Herguido, *Int. J. Hydrogen Energy*, 2011, **36**, 7043–7050.
217. K. Svoboda, G. Slowinski, J. Rogut and D. Baxter, *Energy Convers. Manag.*, 2007, **48**, 3063-3073.
218. A. Murugan, A. Thursfield and I. S. Metcalfe, *Energy Environ. Sci.*, 2011, **4**, 4639–4649.

8 Appendix

8.1 Abbreviations

3DOM – three-dimensionally ordered macro-porous

AR – air reactor

ASU – air separation unit

BGL – British Gas/Lurgi

BHA – barium hexaaluminate

CDCL –coal direct chemical looping

CLC – chemical looping combustion

CLH – chemical looping hydrogen

CLWS – chemical looping water splitting

CoPr – co-precipitation

EDX – energy-dispersive X-ray spectroscopy

FR – fuel reactor

GDC – gadolinium-doped ceria

GDP – gross domestic product

GHG – green house gas

HRSG – heat recovery steam generator

ID – inner diameter

IGCC – integrated gasification combined cycle

IPCC – The intergovernmental panel on climate change

IWI – incipient wetness impregnation

LSF – $La_{0.8}Sr_{0.2}FeO_{3-\delta}$

MFC – mass flow controller

Mtoe – million of tons of oil equivalent

NAFO – Na, Al, Fe, oxide

NMAFO – Na, Mg, Al, Fe, oxide

OC – oxygen carrier

OD – outer diameter

OECD – Organisation for Economic Co-operation and Development

O&M – operation and maintenance

OSR-CLH – oil shale retorting process

PMMA – poly(methyl methacrylate)

ppb – parts per billion

ppm – parts per million

ppmv – parts per million volume fraction

PSA – pressure swing adsorption

RCP – representative concentration pathway

RCP 2.6 – radiation peak at 3 $W \cdot m^{-2}$ before 2100

RCP 4.5 and 6.0 – radiation peak at 4.5 $W \cdot m^{-2}$ and 6.0 $W \cdot m^{-2}$ before 2100

RCP 8.5 – radiation peak > 8.5 $W \cdot m^{-2}$ by 2100

RESC – reformer sponge iron cycle

SEM – scanning electron microscope

SIP – steam iron process

SIR – steam iron reformer

SOFC – solid oxide fuel cell

SR – steam reactor

TGA – thermogravimetric analysis

TPR – temperature programmed reduction

TRCL – three reactor chemical looping

wt% – weight percent

XRD – x-ray diffraction

YSZ – yttria-stabilized zirconia

8.2 Data tables

Table 7: Overview of the prepared and utilized oxygen carrier.

Active component	Additives/Support	Preparation method	Experimental device	Composition	Reference
Fe	$NiFe_2O_4$, $CoFe_2O_4$ ZrO_2	Incipient wetness method	Fixed bed	Fe/Ni = 1.9/1 wt% Fe/Co = 2.1/1 wt%	83
Fe	CeO_2	Chemical precipitation		$Ce_{1-x}Fe_xO_{2-\delta}$ x = 0, 0.1, 0.2, 0.3, 0.4, 0.5, 0.6, 1	84
Fe	ZrO_2	Co-precipitation	TGA, packed bed, fluidized bed	Fe_2O_3 = 83.7 – 82.2 wt% Fe_2O_3 = 58 – 58.2 wt%	87
Fe	ZrO_2	Co-precipitation	TGA +fixed bed	Fe_2O_3/ZrO_2 = 20/80 wt%	88,89
Fe	ZrO_2, CeO_2, $Zr_{0.8}Y_{0.2}O_{2-\delta}$ (YSZ) $Ce_{0.8}Gd_{0.2}O_{2-\delta}$ (GDC)	Solid state reaction	TGA	Fe_2O_3/support = 30/70 wt%	90
Fe	TiO_2, $La_{0.8}Sr_{0.2}$, FeO_3, Al_2O_3, YSZ	Solid state reaction	TGA	Fe_2O_3 = 60 wt%	86
Ce	ZrO_2 $Ce_{0.8}Zr_{0.2}O_2$	Colloidal crystal template method	TPR	Ce/Zr = 80/20 wt%	91
Ce	ZrO_2 $Ce_{0.8}Zr_{0.2}O_2$	Colloidal crystal template method	TPR	Ce/Zr = 80/20 wt%	92
Fe	CeO_2	Co-precipitation	Fixed bed	Fe/Ce = 1	93
Fe	CeO_2	Co-precipitation	TPR	Fe/Ce = 95/5, 90/10, 80/20, 60/40, 50/50 wt%	94
Fe	Support: Al_2O_3 Additives: MoO, CeO_2	Citrate sol-gel method	Fixed bed	Fe_2O_3 wt% / Al_2O_3 wt% / MoO_3 wt% / CeO_2 wt%: 100 / 0 / 0 / 0; 98 / 1.90 / 0.10 / 0; 98 / 1.75 / 0.25 / 0; 98 / 1.50 / 0.50 / 0; 98 / 1.75 / 0 / 0.25; 97.79 / 1.75 / 0.20 / 0.25	95

Table 7: Overview of the prepared and utilized oxygen carrier (continued).

Active component	Additives/Support	Preparation method	Experimental device	Composition	Reference
Fe	Ce, Zr, Mo	Urea hydrolysis, impregnation	TPR,TGA		96 97
Fe	Mo	Hydrothermal synthesis	TPR	Fe_2O_3, Fe_2O_3/Mo = 95/5, 92/8, 90/10 mol%	98
Fe	Al_2O_3, SiO_2, CaO	Co-precipitation, urea hydrolysis	TPR		99
Fe	CaO	Mechanical mixing	TGA, TPR, fluidized bed	Fe_2O_3/CaO = 50/50, 42.7/57.3, 33.3/66.7 mol%	100
Fe $Ca_2Fe_2O_5$	ZrO_2	Pechini method	TGA, fixed bed	Fe_2O_3/ZrO_2 = 60/40 wt%	101
Fe	Al_2O_3, Na_2O, MgO	Co-precipitation	TGA, fixed bed		106

Sample name	Fe wt%	Ce wt%	Zr wt%	Mo wt%
FCZ	56.1	10.1	4.49	
FCZ-1Mo	58.0	11.0	4.50	0.96
FCZ-2Mo	58.0	10.0	4.50	1.50
FCZ-3Mo	57.0	10.0	4.50	3.00
FCZ-4Mo	57.0	10.0	4.50	4.10
FCZ-5Mo	56.0	11.0	4.40	5.50
0 Mo	56.1	10.1	4.49	
1 Mo	52.6	9.72	4.43	0.98
2 Mo	50.8	9.61	4.28	1.91
3 Mo	49.4	9.16	4.22	2.85
4 Mo	48.8	9.20	4.18	3.78
5 Mo	48.4	8.94	4.12	4.71

Sample name	Fe_2O_3 wt%	Al_2O_3 wt%	SiO_2 wt%	CaO wt%
F1	100.0			
F2	95.0	5.0		
F3	92.5	5.0		2.5
F4	90.0	5.0	7.5	5.0
F5	88.5	5.0	7.5	
F6	90.0	5.0	7.5	2.5
F7	85.0	5.0	7.5	7.5
F8	85.0		5.0	2.5
F9	85.0			5

Sample name	Fe_2O_3 wt%	Al_2O_3 wt%	Na_2O wt%	MgO wt%	other wt%
NAFO	64.3	20.7	12.2	0	2.8
NMAFO	51.7	25.2	10.7	10.2	2.1

Table 7: Overview of the prepared and utilized oxygen carrier (continued).

Active component	Additives/Support	Preparation method	Experimental device	Composition	Reference
Fe	TiO_2 illmenite	Ball milled, tablet pressed	TGA, fixed bed	Fe_2TiO_5	110
Fe	TiO_2, SiO_2, Al_2O_3, CaO, MgO, Na_2O, MnO, Cr_2O_3, K_2O,	Fractioning, calcination	TGA, fixed bed	Fe_2O_3 wt% / TiO_2 wt% / SiO_2 wt% / Al_2O_3 wt% / CaO wt% / MgO wt% / Na_2O wt% / MnO wt% / Cr_2O_3 wt% / K_2O wt% / rest wt%t Illmenite: 44.8 / 29.1 / 11.3 / 8.3 / 1.34 / 2.83 / 1.33 / 0.10 / 0.11 / 0.13 / 0.66 CVRD - Iron ore: 94.79 / 0.00 / 4.31 / 0.90 / 0.00 / 0.00 / 0.00 / 0.00 / 0.00 / 0.00 / 0.00 MAC - Iron ore: 93.96 / 0.00 / 3.96 / 2.08 / 0.00 / 0.00 / 0.00 / 0.00 / 0.00 / 0.00 / 0.00 YD - Iron ore: 93.19 / 0.00 / 5.20 / 1.61 / 0.00 / 0.00 / 0.00 / 0.00 / 0.00 / 0.00 / 0.00	111,139
Fe	SiO_2,Al_2O_3, KNO_3 as promotor	Impregnation	Fluidized bed	Fe_2O_3/SiO_2/Al_2O_3/other = 83.25/7.06/5.32/4.37 wt% KNO_3 loading = 0, 3, 6, 10 wt%	113
Mixed Fe-Cu	Al_2O_3	Co-precipitation, incipient wetness impregnation	TPR Fluidized bed	20 OC samples prepared, samples tested Sample name / Fe_2O_3 wt% / CuO_3 wt% / Al_2O_3 wt% Fe18-IWI: 8 / 82 Fe62-CoPr: 62 / 38 Cu17-IWI: 17 / 83 Cu60-CoPr: 60 / 40 Fe16Cu15-IWI: 16 / 15 / 69 Fe17Cu15-CoPr: 17 / 15 / 68	114
Fe	perovskite $LaNiO_3$ $CeO_2/LaNiO_3$	Citric acid complexation, impregnation	TPR, fixed bed	$Fe_2O_3/LaNiO_3$ = 15/85 wt% $Fe_2O_3/CeO_2/LaNiO_3$ = 15/5/80 wt%	116

Table 7: Overview of the prepared and utilized oxygen carrier (continued).

Active component	Additives/Support	Preparation method	Experimental device	Composition	Reference
Fe	CeO_2, $Ca_{0.8}Sr_{0.2}Ni_{0.2}O_3$, $MgAl_2O_4$	Citric acid, Co-precipitation, solid state reaction	TGA	Fe_2O_3/CeO_2 = 30/70 mol% solid state reaction $Fe_2O_3/MgAl_2O_4$ = 30/70 wt% solid state reaction Fe_2O_3/CeO_2 = 30/70 mol% co-precipitation Fe_2O_3/CeO_2 = 40/60 mol% co-precipitation $Fe_2O_3/Ca_{0.8}Sr_{0.2}Ti_{0.8}Ni_{0.2}O_3$ = 30/70 mol% citric acid	117
Fe	$LaFeO_3$	3DOM-$LaFeO_3$: Polystyrene colloidal crystal templating method, nano-$LaFeO_3$: combustion method	TPR, fixed bed	3DOM-$LaFeO_3$, nano-$LaFeO_3$	118
Fe	$LaFeO_3$ Co doping	Combustion method	TPR, fixed bed	$LaFe_{1-x}Co_xO_3$ x = 0.1,0.3,0.5,0.7,1.0	119
Fe	$La_{0.8}Sr_{0.2}FeO3_{-\delta}$ (LSF)		Fixed bed	Fe_2O_3/LSF = 25/40 wt%	123
Fe	$CoFe_2O_4$ spinel	Co-precipitation	Fixed bed	$CoFe_2O_4$	129
Fe	$CoFe_2O_4$ spinel	Co-precipitation	Fixed bed	$CoFe_2O_4$	130
Fe	Spinell type $NiFe_2O_4$, Fe_3O_4	Co-precipitaion	TPR, fixed bed	$NiFe_2O_4$, Fe_3O_4	131
Fe	Co,and Mn	Co-precipitaion	Fixed bed, TPR	$M^1_{0.6-x}M^2_xFe_{2.4}O_y$ Co:Mn = 1:0, 0.9: 0.1, 0.5:0.5 and 0:1	132
Fe	Spinel $NiFeAlO_4$	Mechanical mixing	TGA, fixed bed	$NiFeAlO_4$	133
Fe	BHA barium hexa-aluminate,	One-pot synthesis	Fixed bed	40 wt% Fe-nanoparticles: 16, 22, 54 nm	134
Co-W	Ni, La_2O_3	Co-precipitation Impregnation	TGA	$CoWO_4$/Ni = 10 wt% Ni $CoWO_4/La_2O_3$ = 10 wt% La	115
Fe	$MgAl_2O_4$	Freeze-granulation	Fluidized bed	$Fe_2O_3/MgAl_2O_4$ = 60/40 wt%	135

Table 7: Overview of the prepared and utilized oxygen carrier (continued).

Active component	Additives/Support	Preparation method	Experimental device	Composition	Reference
Fe	Al_2O_3	Co-precipitation,		Fe_2O_3/Al_2O_3 = 66.7/33.3 wt%	146
Fe	Al_2O_3	Mechanical mixing	Fixed bed	Fe_2O_3/Al_2O_3 = 60/40 wt%	148
Fe	ZrO_2	Co-precipitation	Fluidized bed	Fe_2O_3/ZrO_2 = 20/80 wt%	28
Fe	CeO_2/Al_2O_3	Co-Precipitation	Fixed bed	$Fe_2O_3/CeO_2/Al_2O_3$ = 98/0.25/1.75 wt%	151,152
Fe		Co-precipitation	TPR	Fe_3O_4	153
			Fixed bed		
Fe		Hematite: thermal treatment Magnetite: thermal decomposition Goethite: co-precipitation	TPR	Goethite (γ-FeOOH), hematite (α-Fe_2O_3), magnetite (Fe_3O_4)	154
Fe	CeO_2/Al_2O_3, $NiO/NiAl_2O_4$	Co-Precipitation mechanical mixing	Fixed bed	$Fe_2O_3/CeO_2/Al_2O_3$ = 98/0.25/1.75 wt% $NiO/NiAl_2O_4$ 10 wt% excess mixture: 67.5 wt% OC, 7.5 wt% cat, 25 wt% silica	156,155,157
Fe	CeO_2/Al_2O_3	Co-precipitation	Fixed bed	$Fe_2O_3/CeO_2/Al_2O_3$ = 90.17/4.79/5.04 wt%	54
Fe	Fe_2O_3/Al_2O_3	Mechanical mixing	Fixed bed	Fe_2O_3/Al_2O_3 = 90/10 wt%	55,158
Fe	Al_2O_3	Mechanical mixing	Fixed bed	Fe_2O_3/Al_2O_3 = 59.4/40.3 wt%	182
Fe	Al_2O_3	Mechanical mixing	TGA	Fe_2O_3/Al_2O_3 = 50/50 wt%	184
Fe	ZrO_2	Co-precipitation	TGA	Fe_2O_3/ZrO_2=20/80 wt%	186
Fe	Al_2O_3	Impregnation method	TGA	Fe_2O_3/Al_2O_3 = 45/55 wt% Fe_2O_3/Al_2O_3 = 25/75 wt%	190,191
Fe Fe-Cu	Al_2O_3, TiO_2	Mechanical mixing	TGA	$Fe_2O_3/CuO/Al_2O_3$ = 60/20/20 wt% Fe_2O_3/TiO_2 = 80/20 wt%	192

Table 7: Overview of the prepared and utilized oxygen carrier (continued).

Active component	Additives/Support	Preparation method	Experimental device	Composition	Reference
Fe	CeO_2/Al_2O_3	Citrate method	Fixed bed	$Fe_2O_3/CeO_2/Al_2O_3$ = 98/0.5/1.5 wt%	[195]

Table 8: Overview of chemical looping plants in operation.

System	Organization	Power range	Gas feed	Solid flow/solid inventory	Reaction temperatures	Dimension	Reference
Three-reactor moving bed system	Ohio State University	25 kW_{th}	Syngas CO/H_2 = 2:1, 15 $L \cdot min^{-1}$	150 $g \cdot min^{-1}$	900 °C		[48,112,143,144]
2-compartment fluidized bed	Chalmers University of Technology, Sweden		Syngas or CO: 0.5-1.25 $L \cdot min^{-1}$ steam: 4-5 $L \cdot min^{-1}$	180 – 240 $g \cdot min^{-1}$	800 – 900 °C	System height: 300 mm reactor: 25x25 mm	[135]
µ-System	University of Newcastle, Australia	µ-System	CH_4		900 °C	Reactor length: 0.05 m, cross section area: 200x100 µm	[146,147]
Three-reactor fluidized bed system	Key Laboratory of Energy Thermal Conversion and Control, China	50 kW	Feed: 24-31 $Nm^3 \cdot h^{-1}$	Solid material = 5 kg	Cold flow mode		[140]
Three-reactor counter-current moving bed system	Hydrogen and Fuel Cell Department, Korea	300 W_{th}	CH_4: 0.55 $L \cdot min^{-1}$ steam: 0.25 $L \cdot min^{-1}$	65 – 75 $g \cdot min^{-1}$	FR: 900 °C SR: 800 °C		[28]
Multistage circulating moving bed reactor	Department of Chemical Engineering, Korea		Compressed air	22 kg 20 – 100 $kg \cdot m^{-2} \cdot s^{-1}$	Ambient – 850 °C	Fuel reactor: 0.07 (bottom), 0.16 (top)x0.06x1 m^3 steam reactor: 0.16x0.06x1.4 m^3 riser: 0.03x0.06x3.8 m^3	[149]
Interconnected circulating fluidized bed reactor	Aragon Institute of Engineering Research, Spain		H_2/CH_4	0.235 kg 85 wt% Fe_2O_3 15 wt% SiO_2	500 – 575 °C	Reactor: steel tube ID = 5.4 cm, OD = 6.0 cm, height = 41.5 cm	[142]

Table 9: Summary of kinetic data.

Sample	Sample properties	Reaction parameters	Reaction model	Rate constants Reduction	Rate constants oxidation	Ea reduction	Ea oxidation	Reference
Fe_2O_3/ZrO_2	Particle size = 150-300 µm porosity = 50% BET = 2.2 $m^2 \cdot g^{-1}$	550 – 800 °C H_2 = 2 vol% H_2O = 5 vol%		Step 1 = $7.8 \cdot 10^{-3}$ s^{-1} step 2 = $1.4 \cdot 10^{-3}$ s^{-1} step 3 = $2.7 \cdot 10^{-4}$ s^{-1}	$4.4 \cdot 10^{-4}$ s^{-1}			90
Fe_2O_3/CeO_2	Particle size= 150-300 µm porosity 32% BET 1.0 $m^2 \cdot g^{-1}$	550 – 800 °C H_2 = 2 vol% H_2O = 5 vol%		Step 1 = $4.1 \cdot 10^{-3}$ s^{-1} step 2 = $1.4 \cdot 10^{-3}$ s^{-1} step 3 = $7.0 \cdot 10^{-4}$ s^{-1}	$9.6 \cdot 10^{-4}$ s^{-1}			90
Fe_2O_3/YSZ	Particle size = 150-300 µm porosity = 50% BET = 1.5 $m^2 \cdot g^{-1}$	550 – 800 °C H_2 = 2 vol% H_2O = 5 vol%		Step 1 = $2.7 \cdot 10^{-2}$ s^{-1} step 2 = $2.8 \cdot 10^{-3}$ s^{-1} step 3 = $4.1 \cdot 10^{-4}$ s^{-1}	$1.2 \cdot 10^{-3}$ s^{-1}			90
Fe_2O_3/GDC	Particle size = 150-300 µm porosity = 38% BET = 1.0 $m^2 \cdot g^{-1}$	550 – 800 °C H_2 = 2 vol% H_2O = 5 vol%		Step 1 = $1.9 \cdot 10^{-2}$ s^{-1} step 2 = $2.3 \cdot 10^{-3}$ s^{-1} step 3 = $9.1 \cdot 10^{-4}$ s^{-1}	$1.5 \cdot 10^{-3}$ s^{-1}			90
$Fe_2O_3/Ce_{0.5}Zr_{0.5}O_2$ 80/20 wt% Mo 1 – 5 wt%	Surface area $m^2 \cdot g^{-1}$ 0 Mo = 68.67 1 Mo = 55.54 2 Mo = 56.67 3 Mo = 56.66 4 Mo = 50.56 5 Mo = 48.44	650, 750, 800 °C 5 – 15 °C·min^{-1} H_2				Peak 1/Peak 2 kJ·mol^{-1} 0 Mo = 110.6/69.2 1 Mo =107.4/67.1 2 Mo = 108.5/63.6 3 Mo = 100.3/70.4 4 Mo = 99.6/60.4 5 Mo = 87.3/55.4		96
$Fe_2O_3/Ce_{0.5}Zr_{0.5}O_2$ 80/20 wt% Mo 1 – 5 wt%	Surface area $m^2 \cdot g^{-1}$ FCZ = 68.7 FCZ-1Mo = 60.2 FCZ-2Mo = 53.5 FCZ-3Mo = 65.4 FCZ-4Mo = 66.2 FCZ-5Mo = 60.3	750, 800 °C H_2				Peak 1/Peak 2 kJ·mol^{-1} FCZ = 110.6/69.2 FCZ-1Mo = 54.9/46.5 FCZ-2Mo = 63.2/54.8 FCZ-3Mo = 51.4/48.4 FCZ-4Mo = 87.6/55.7 FCZ-5Mo = 94.6/41.6		97

Table 9: Summary of kinetic data (continued).

Sample	Sample properties	Reaction parameters	Reaction model	Rate constants Reduction	Rate constants oxidation	Ea reduction	Ea oxidation	Reference
$Fe_2O_3/Al_2O_3/SiO_2$/ CaO	Surface area $m^2 \cdot g^{-1}$ F1 (Fe_2O_3) = 32.2 F2 (Fe-5Al) = 48.8 F3 (Fe-5Al-5Ca) = 48.3 F4 (Fe-5Al-5Ca) = 74.1 F5 (Fe-5Al-7.5Si) = 93.1 F6 (Fe-7.5Si-2.5Ca) = 74.8 F7 (Fe-7.5Si-7.5Ca) = 79.3 F8 (Fe-5Al-7.5Si-2.5Ca = 95.6 F9 (Fe-5Al-5Si-5Ca) = 77.6	650, 750, 800 °C H_2				Peak 1/Peak 2 $kJ \cdot mol^{-1}$ F1 = 104.4/37.0 F2 = 116.3/111.9 F3 = 125.3/72. F4 = 89.3/96.9 F5 = 96.4/207.3 F6 = 114.8/137.5 F7 = 78.9/270.5 F8 = 101.6/332.5 F9 = 93.7/332.6		99
Cu-Fe	Particle size: Fe16Cu15-IWI = 115 µm Fe17Cu15-CoPr = 143 µm	530 – 825 °C H_2O = 5.5 vol%	IWI: Avramie Erofeyev (A2) CoPr: Nuclei growth model				IWI = 46±4 $kJ \cdot mol^{-1}$ CoPr = 51±5 $kJ \cdot mol^{-1}$	114
$CoWO_4$ $CoWO_4$ 10 wt%Ni $CoWO_4$ 10 wt%La		850-950 °C CH_4 = 2 – 8 vol%		1st cycle CoW = 0.2-1.6 $\cdot 10^{-3} \cdot min^{-1}$ CoW-Ni: 1.2-3.2 $\cdot 10^{-3} \cdot min^{-1}$ CoW-La = 0.5-1.7 $\cdot 10^{-3} \cdot min^{-1}$ 2nd cycle CoW = 0.7-1.5 $\cdot 10^{-3} \cdot min^{-1}$ CoW-Ni = 1.3-3.0 $\cdot 10^{-3} \cdot min^{-1}$ CoW-La = 1.1-2.9 $\cdot 10^{-3} \cdot min^{-1}$		1st cycle CoW = 221 $kJ \cdot mol^{-1}$ CoW-Ni = 134 $kJ \cdot mol^{-1}$ CoW-La = 140 $kJ \cdot mol^{-1}$ 2nd cycle CoW = 151 $kJ \cdot mol^{-1}$ CoW-Ni = 95 $kJ \cdot mol^{-1}$ CoW-La = 111 $kJ \cdot mol^{-1}$		115
Fe		973 – 1473 K H_2O_g = 4.9, 9.4, 17.2 vol% CO_2 = 4,7,7, 14.3 vol%					H_2O = 47.3 $kJ \cdot mol^{-1}$ CO_2 = 32.8 $kJ \cdot mol^{-1}$	196
Fe45/Al	Particle size = 75−150 µm	973 – 1073 K CH_4 = 0.5 vol%	Fe_2O_3/Fe_3O_4: Nuclei growth D2, D3 $Fe_3O_4/FeAl_2O_4$: Jander equ. D3			Fe_2O_3/Fe_3O_4 = 24.96 $kJ \cdot mol^{-1}$ $Fe_3O_4/FeAl_2O_4$ = 171.24 $kJ \cdot mol^{-1}$		190

Table 9: Summary of kinetic data (continued).

Sample	Sample properties	Reaction parameters	Reaction model	Rate constants Reduction	Rate constants oxidation	Ea reduction	Ea oxidation	Reference
Fe25/Al	Particle size = 75 − 150 µm	973 – 1073 K CH_4 = 0.5 vol%	Fe_2O_3/Fe_3O_4: Nuclei growth D2, D3 $Fe_3O_4/FeAl_2O_4$: Jander equ. D3			Fe_2O_3/Fe_3O_4 = 24.77 kJ·mol^{-1} $Fe_3O_4/FeAl_2O_4$ = 209.16 kJ·mol^{-}		190
$Fe_{0.933}O$ 0.05<X<0.2	Particle size = 300 – 425 µm, 150 – 212 µm	1073 K CO = 50 vol%	Linear correlation			H_2 = 62±9 kJ·mol^{-1} CO = 83±14 kJ·mol^{-1}		194
$Fe_{0.933}O$ 0.2<X<1	Particle size = 300–425 µm, 150 – 212 µm	1073 K CO = 50 vol%	Random pore model			H_2 = 62±19 kJ·mol^{-1} CO = 64±8 kJ·mol^{-1}		194
Fe_2O_3-FeO FeO-Fe	Density = 3.80 g/cm^3 Bulk density = 2.46 g/cm^3 BET surface area = 2.6 m^2/g Particle size = 125 – 300 µm	CH_4 = 10-55 vol% 825 - 900 °C H_2 = 10 – 25 vol% 750 - 900 °C CO = 10-25 vol% 750 – 900 °C	Phase boundary controlled, contracting sphere R3 contracting infinite slab R1			CH_4 = Fe_2O_3-FeO = 251 kJ·mol^{-1} FeO-Fe = 230 kJ·mol^{-1} H_2 = Fe_2O_3-Fe: 59 kJ·mol^{-1} CO = Fe_2O_3-Fe = 37 kJ·mol^{-1}		186
Fe-Fe_3O_4 Fe-Fe_2O_3	Density = 3.80 g/cm^3 Bulk density = 2.46 g/cm^3 BET surface area = 2.6 m^2/g particle size = 125 – 300 µm	H_2O = 5,10,15, 20 vol% Air = 3,6,9,12 vol% 600 - 900 °C	Phase boundary controlled, contracting sphere R3				H_2O: Fe-Fe_3O_4 = 27 kJ·mol^{-1} Air: Fe-Fe_2O_3 = 7 kJ·mol^{-1}	186
Fe_2O_3-Fe_3O_4 Natural ore	Mean particle ~ 92.5 µm Surface area ~ 5.74 m^2/g	800 – 950 °C CH_4 = 33 vol%	Phase boundary			215 kJ·mol^{-1}		187
Fe_2O_3 on 20% TiO_2	Particle size < 250 µm	600-950 °C H_2	First order reaction F1 Phase boundary controlled R3			33.8 kJ·mol^{-1}		192
Fe_2O_3/CuO on Al_2O_3 60/20/20	Particle size = < 250 µm	600-950 °C H_2	First order reaction F1 3D diffusion Jander equation			42.6 kJ·mol^{-1}		192
Fe_2O_3/Al_2O_3/CeO		450-600 °C H_2/CH_4 mixture	Johnson-Mehl-Avrami-Kolmogorov, Levenberg-Marquardt algorithm			Differential kinetics = 75 kJ·mol^{-1} Integral kinetics = 48±4 kJ·mol^{-1}l	Differential kinetics 0 kJ·mol^{-1} Integral kinetics: 0 kJ·mol^{-1}l	195
Fe_2O_3/Fe_3O_4/FeO	Particle size = 60 – 100 µm	750-825 °C CH_4 15, 20, 25 vol%	Multi-step kinetics: first order, nucleation growth			R1 = 34.4±0.5 kJ·mol^{-1} R2 = 39.3±1.6 kJ·mol^{-1}		189

Table 9: Summary of kinetic data (continued).

Sample	Sample properties	Reaction parameters	Reaction model	Rate constants Reduction	Rate constants oxidation	Ea reduction	Ea oxidation	Reference
$Fe_2O_3/Fe_3O_4/FeO$	Particle size = 100 − 300 µm	700 – 950 °C H_2 5,10, 20 vol%				Double-step: R1 = 6.15±0.2 kJ·mol^{-1} R2 = 56.9±1.1 kJ·mol^{-1} Single-step = 64.15 ± 0.5 kJ·mol^{-1}		188
Fe_2O_3	Particle size = 450–900 µm	1073 K CO		Reaction front reaction rate Fe_2O_3/Fe_3O_4 = 5.280 mol·m^{-3}·s^{-1} Fe_3O_4/FeO = 3.329 mol·m^{-3}·s^{-1} FeO/Fe = 4.379 mol·m^{-3}·s^{-1}				183
Fe_2O_3 50 wt% Al_2O_3	Particle size = 100-200 µm	973 – 1173 K CO	Pure Fe_2O_3: 2D phase boundary Fe_2O_3/Al_2O_3 diffusion controlled			Pure Fe_2O_3 = 33.3±0.8 kJ·mol^{-1} Fe_2O_3/Al_2O_3 = 41.1±2.0 kJ·mol^{-1}		184

8.3 List of figure

8.4 List of tables